PROXIMITY EFFECTS AND VORTEX DYNAMICS IN MESOSCOPIC SUPERCONDUCTOR-NORMAL METAL-SUPERCONDUCTOR ARRAYS

BY

SERENA MERTEEN ELEY

DISSERTATION

Submitted in partial fulfillment of the requirements
for the degree of Doctor of Philosophy in Physics
in the Graduate College of the
University of Illinois at Urbana-Champaign, 2012

Urbana, Illinois

Doctoral Committee:

Professor James Eckstein, Chair
Professor Nadya Mason, Director of Research
Professor Eduardo Fradkin
Professor John Stack

Abstract

Anderson's scaling theory of localization has proven invaluable in characterizing the behavior of real systems, that is, those possessing any amount of disorder. The theory predicts that, at zero temperature in 1D and 2D systems, the diffusive motion of electrons scattering off impurities ceases, and there is no long range electron transport. In other words, there are no metallic states at $T = 0$ in 1D and 2D systems. Although this theory has accurately described the low-temperature behavior of many materials, systems ranging from 2D semiconductors [1] to disordered superconductors [2,3] have in fact shown evidence of a "forbidden" zero-temperature metallic state. To reconcile these experimental results with Anderson localization, it has been proposed that these observations do not pertain to conventional metals, but rather to spatially inhomogeneous correlated states [4–6]. Determining the origin and characteristics of such states has attracted intense theoretical and experimental interest over the past two decades. Contributing to these efforts, we engineer a tunable, intrinsically phase-separated system. Our research focuses on novel model systems of 2D superconductors, systems which have been predicted to exhibit unusual metallic states as the temperature approaches zero. In particular, we created triangular arrays of physically separated mesoscopic superconducting islands placed on normal metal films, and measured the temperature-dependent transition to the superconducting state as a function of the island separation. We found two surprising results: first, the long-range communication between the islands occurs in a way that cannot be explained by current theories. Second, the progressive weakening of superconductivity with increasing island spacing suggests that arrays with even further spacing would be metallic at $T = 0$. This is the first systematic study of an inhomogeneous superconducting system that systematically approaches a zero-temperature metallic state. Finally, the sparsest arrays studied show evidence of a 2D metallic state.

The results suggest that such superconductor-normal-metal systems may be an ideal medium for tunably controlling the properties of this strange metal. To further understand these systems, we characterize the

vortex dynamics intrinsic to the 2D superconducting ground state, as well as that in response to an externally applied current and magnetic field. We provide evidence that the superconducting state is characterized by bound vortex-antivortex pairs. Additionally, we study the current-voltage characteristics; applying a current induces a Lorentz force on vortices that competes with pinning in the arrays. Lastly, in response to sweeping the field, we observe resistance oscillations, manifestations of competing magnetic ground states and correlated vortex motion.

This thesis is dedicated to my Mom, for teaching me the importance of education and providing unending encouragement. I also dedicate this thesis to Eric, who regularly drove 8 hours round-trip to spend his weekends with me in lab.

Acknowledgments

Numerous studies, both theoretical and experimental, have been concerned with competition between potentially disparate chapters in a thesis. Schulman *et al.*[7] emphasized the importance of the acknowledgments section, stating that "The Ph.D. thesis usually begins with a pithy quote, after which there will sometimes be a dedication to one's parents, life partner, and/or pet tapir. Following this is probably the most important part of the dissertation: the acknowledgments section. This is the only section that everyone who picks up your thesis will read. They will happen upon your dissertation in the library and flip through the first few pages, looking for a juicy acknowledgments section. This is your chance to make obscure references to secret loves .... or be very mysterious by having no acknowledgments section at all so that everyone wonders what you're hiding." Well, my alligator skull sitting on a desk in my office right now; I certainly have nothing to hide, so, here goes...

In high school, we were dreamers. My friends and I wanted to solve the most baffling, and often esoteric, scientific mysteries. Desire and fortitude, however, are completely different issues. I would like to start by thanking the teachers at Thomas Jefferson High School for Science and Technology for their zealous support and patient encouragement during my high school years. Afterwards, I was fortunate enough to attend the California Institute of Technology, a similarly unique environment, full of integrity, optimism, and support. These two environments really fortified my interest in the sciences and provided me with a foundation integral towards pursuing a scientific career.

It was an honor it attend the University of Illinois, getting to walk in the footsteps of Bardeen, Cooper and Schrieffer[8]. There were many advantages to joining a Physics department with a powerhouse of condensed matter research groups. Thanks to those who lent me liquid helium at odd hours or for weekend work – most notably, the members of Professor Eckstein's group. Additionally, Professor Van Harlingen's group was an excellent source of advice when we were first setting up the lab. Special thanks to Martin Stehno

and Dan Bahr for their detailed advice over the years.

This thesis would not have been possible without the Frederick Seitz Materials Research Lab. More specifically, I would like to acknowledge the staff at the Center for Microanalysis of Materials (CMM) and Micro/Nanofabrication Facility (Microfab), and the Department of Energy grant number DE-FG02-07ER46453. Many thanks to Tony Banks, not only for his technical assistance and insightful advice, but also the remarkably upbeat attitude and general optimism that made him a great role model. I am grateful to Doug Jeffers for his expeditious assistance with issues ranging from broken sample stage transfer arms in ultra-high vacuum systems to building sump pump failures.

I would also like to thank my adviser, Professor Nadya Mason. I was lucky enough to get the opportunity to join a new lab and help with the initial set-up, and I'd like to specifically thank her for the project itself, securing appropriate funding, allowance to attend interesting conferences, and project management. It was an immensely enjoyable project. Getting to fabricate intricate samples and collect aesthetically pleasing data (see Figure 6.2 on page 80) full of interesting physics was the highlight of my time in Champaign-Urbana. Perhaps I will always be stunned by microscopic phenomena than reveal themselves in such a macroscopically pronounced manner. I also simply enjoy probing limits – fabricating and studying *nanoscale* devices at *milli*-Kelvin temperatures in search of *negligible* resistances. I greatly appreciate my collaborators, Sarang Gopalakrishnan and Professor Paul Goldbart, for their contributions to this research.

I would like to acknowledge my fellow lab group members, most notably Travis Dirks, Yung-Fu Chen, Cesar Chialvo, and Sungjae Cho. Travis, your intriguing ideas and stock market advice have made me slightly richer today. Yung-Fu, thanks for setting such a great example of meticulous conduct in lab. Cesar, you were always reliable and I thank you for your assistance with machining-related issues. Sungjae, thanks for the career advice and exposure to your enthusiasm towards research. Further, thanks to Clare Li, Nick Bronn, Scott Scharfenberg, and David Barnes, for helping create such a friendly working environment.

I would also like to express my gratitude to my local parents, Chris and Pam Hohn. Thanks for lending me a car when mine was totalled, providing housing when my choice apartments were sub-optimal, access to your laundry machines, and for the memorable trips to the Indy 500. Having local family really enhanced my experiences here. I would also like to thank Eric Anderson for his limitless patience and support in both my academic endeavors and obsession with long distance running. My mother and three sisters also deserve praise for their encouragement. In addition, thanks to Toni Pitts for being such a good friend. Last but not least, I would like to thank Professors John Stack, James Eckstein, Eduardo Fradkin and Nadya Mason. I truly appreciate your time in reading this document, evaluating my defense.

What about secret loves? Just the Raith, the wedge wire-bonder, and a love-hate relationship with the

dilution refrigerator...

Table of Contents

List of Tables . . . . . **x**

List of Figures . . . . . **xi**

List of Symbols . . . . . **xiii**

Chapter 1 Introduction **1**
1.1 Motivation 1
1.2 Introduction to Thesis Problem 4
1.3 Introduction to Superconductivity 7
1.4 Superconductivity in 2D 8
1.5 Superconductor-Normal Metal Bilayers: The Proximity Effect 12
1.6 Josephson Junction Arrays 13
1.7 The Usadel Equations 21

Chapter 2 Experimental Techniques **24**
2.1 Sample Fabrication 24
2.2 Summary of Samples Presented in this Thesis 28
2.3 Measurement Set-up 33

Chapter 3 Two-Step Transition to Superconductivity **36**
3.1 Two-Step Transitions in Arrays with Island Spacings $d = 90$ – 340 nm 36
3.2 Dependence of Transitions on Island Height in Arrays with Island Spacings $d = 90$ – 340 nm 38
3.3 Two-step Transitions in Arrays with Island Spacings $d = 490$ – 640 nm 41

Chapter 4 First Transition: Superconductivity in the Islands **46**
4.1 T_1 in Arrays with Island Spacings $d = 90$ – 340 nm 46
4.2 T_1 in Arrays with Island Spacings $d = 490$ – 690 nm 48
4.3 T_1 in Arrays with Island Spacings $d = 740$ – 1140 nm 48
4.4 Understanding Intra-island Coupling through IV Characteristics 50

Chapter 5 Second Transition: Superconductivity Across the Array **55**
5.1 Extracting T_2 from IV Isotherms 56
5.2 T_2 in Arrays with Island Spacings $d = 90$ – 690 nm 60
5.3 Comparison to Lobb-Abraham-Tinkham (LAT) Theory 60
5.4 Understanding Inter-granular Coupling through IV Characteristics 62
5.5 T_2 vs d: Comparison to Model of Single, Diffusive SNS Junction 68
5.6 Possible Emergence of a Metallic Phase in Arrays with Island Spacings $d = 740$ – 1240 nm . 71

Chapter 6 Effects of a Perpendicular Magnetic Field 77
6.1 Magnetic Frustration 77
6.2 Two-step Transition to the Normal State 84
6.3 Smoothly Varying Resistance versus Temperature in a Magnetic Field 89
6.4 Cusps in Resistance versus Temperature in a Magnetic Field 92
6.5 Effects of an Applied Current on Field-Induced Vortices 96

Chapter 7 Conclusions 103
7.1 Summary of Results 103
7.2 Future Work 104

Appendix A Establishing a Clean S-N Interface 106

Appendix B Fabrication Procedure for Nb-Au Arrays 108
B.1 Resistivity and Number of Islands in Each Array 110

Appendix C Additional Magnetic Frustration Data 111

Appendix D Arrays of Al Islands on Au Layer 112
D.1 Superconducting Transitions in Al-Au arrays 113
D.2 Critical Current and Andreev Reflection in Al-Au Arrays 115

References 117

List of Tables

2.1 Island Spacings, Heights, Diffusion Constant, and Thouless Length 30

5.1 Effective Energy Gap and Thouless Energy 67

B.1 Resistivity and Number of Islands 110

List of Figures

1.1 Phase Separation in Superconducting Films on a Rigid Substrate . . . 3
1.2 Phase Diagrams for 2D Superconducting Films: Field, Disorder, and Dissipation . . . 9
1.3 Superconductor-Insulator Transitions in Disordered 2D Films . . . 10
1.4 Phase Glass . . . 11
1.5 The Effects of Dissipation on Phase Transitions in Amorphous MoGe . . . 11
1.6 Superconductivity in Nb-Au Bilayers . . . 13
1.7 Superconductor-Insulator Transitions in Josephson Junction Arrays . . . 16
1.8 Vortex-Antivortex Binding Transition to Superconductivity in SNS Arrays . . . 17
1.9 Illustration of Superconducting Transition in SNS Arrays with Large Islands . . . 18
1.10 Phase Diagram of Superconducting Grains Embedded in a Normal Metal . . . 20

2.1 Schematic of the Nanofabrication Process for Nb-Au SNS Arrays . . . 27
2.2 Schematic of Array Geometry . . . 28
2.3 AFM Topography of Arrays of Nb Islands on Au . . . 29
2.4 SEM Image of Device . . . 31
2.5 X-Ray Diffraction of Nb-Au Bilayer Films . . . 31
2.6 Side-view SEM Image of Array of Nb Islands on Au . . . 32
2.7 Transport Measurement Set-up . . . 34

3.1 Superconductivity in Nb Arrays with Island Spacings $d = 90$ – 340 nm . . . 37
3.2 Comparison of Transitions in Arrays with Different Island Heights . . . 40
3.3 Superconductivity in Nb Arrays with Island Spacings $d = 490$ – 690 nm . . . 42
3.4 Phenomenological Model: Superconducting Transition in SNS Arrays of Mesoscopic Granular Islands . . . 44

4.1 Dependence of T_1 on island height and spacing in arrays with $d = 140$ – 340 nm . . . 47
4.2 Dependence of T_1 on Island Spacing in Arrays with $d = 490$ – 690 nm . . . 48
4.3 T_1 in Dilute Arrays . . . 49
4.4 Multiple Peaks in Current-Biased Differential Resistance Curves in Nb Arrays . . . 51
4.5 The Energy Gap in Niobium . . . 52
4.6 Temperature Dependence of the Island Critical Currents . . . 53

5.1 Illustration of BKT Transition . . . 55
5.2 Identification of BKT Transition . . . 59
5.3 Dependence of T_2 on Island Height and Spacing for $d = 140$ – 690 nm . . . 60
5.4 Dependence of $\xi_N(T_2)$ on Island Height and Spacing for $d = 140$ – 340 nm . . . 61
5.5 Dependence of T_2 on Island Spacing for $d = 490$ – 690 nm . . . 62
5.6 Differential Resistance Isotherms in Array with Island Spacing $d = 490$ nm . . . 63
5.7 Theoretical Zero-Field Current-biased Differential Resistance . . . 64
5.8 Rounding in Differential Resistance Induced by Thermal Noise . . . 65

5.9 Theoretical Temperature dependence of the Critical Current in Diffusive SNS Arrays 66
5.10 Temperature Dependence of the Critical Current in Nb Island Arrays 68
5.11 Dependence of T_2 on Island Spacing 69
5.12 T_2 vs. d: Fit to Single, Diffusive SNS Junction 71
5.13 Transitions in Arrays with Island Spacings d = 740 – 1240 nm: Possible Metallic State 73
5.14 Temperature vs Island Concentration Phase Diagram: Arrays of Nb Islands on Au 76

6.1 Schematic of Magnetic Frustration and Corresponding Vortex Configurations 79
6.2 Magnetic Frustration in Nb Arrays, d = 490 nm and 690 nm 80
6.3 Predictions of the Ground State Energy of Arrays in Magnetic Different Fields 81
6.4 Dependence of Magnetoresistance on Island Spacing 82
6.5 Evidence of Bardeen-Stephen Flux Flow 83
6.6 Temperature Dependence of the Vortex Mobility in Arrays in a Magnetic Field 84
6.7 Two-Step Transition and Magnetoresistance Hysteresis in a Swept Magnetic Field 86
6.8 Magnetoresistance Hysteresis in MoGe Films 87
6.9 Comparison of High-Field Transitions in Arrays with d = 490 – 690 nm 88
6.10 Crossing Point in the Magnetoresistance Isotherms 89
6.11 Thermally Activated Motion of Field-Induced Vortices in Array with d = 490 nm 90
6.12 Cusps in Resistance versus Temperature in a Magnetic Field in Arrays with d = 440 nm . . . 93
6.13 Cusps in Resistance versus Temperature in a Magnetic Field in Arrays with d = 540 nm . . . 95
6.14 Current-biased Differential Resistance in a Magnetic Field 97
6.15 Current-biased Differential Resistance in a Magnetic Field for an array with d = 90 nm . . . 99
6.16 Current-biased Differential Resistance: Sensitivity of Critical Current to a Magnetic Field . . 100
6.17 Evidence of Magnetic Frustration in Current-biased Differential Resistance 101
6.18 Current-biased Differential Resistance in a Magnetic Field for an Array with d = 490 nm . . 102

C.1 Magnetic Frustration Isotherms in Nb Arrays with d = 290 nm, 540 nm, 590 nm, 640 nm . . 111

D.1 Superconductivity in Arrays of Al Islands on Au 114
D.2 Possible BKT Transition in Arrays of Al Islands on Au 114
D.3 Critical Current and Andreev Reflection in Arrays of Al Islands on Au 115

List of Symbols

d	Edge-to-edge spacing between islands
a	Center-to-center spacing between islands (array lattice constant)
z	Height of islands
A	Area of a plaquette
E_B	Maximum energy barrier to vortex motion
D	Diffusion constant
T	Temperature
T_1	Critical temperature of islands
T_2	Critical temperature of array
B	Magnetic field
f	Magnetic frustration, $\frac{BA}{\Phi_0}$
Δ	Superconducting energy gap
ξ_{S}	Superconductor coherence length
ξ_{N}	Normal metal coherence length (Thouless length, L_T)
E_{TH}	Thouless energy
ϕ	Phase of superconducting order parameter
I_c	Critical current
ℓ	Mean free path
I, V, R	Current, Voltage, Resistance
R_d	Differential resistance, $\frac{dV}{dI}$
$\hbar$	Planck's constant, 1.055×10^{-34} J $\cdot$ s
k_B	Boltzmann constant, 1.381×10^{-23} J/K
Φ_0	Magnetic flux quantum, 2.07×10^{-15} Wb
e	Electrical charge, 1.602×10^{-19} C
R_Q	Resistance quantum, $\frac{h}{4e^2} \approx 6.45$ kΩ

Chapter 1

Introduction

1.1 Motivation

Planar arrays of proximity-coupled superconducting islands on metallic underlayers serve as model two-dimensional systems with easily tunable parameters. The research described in this thesis focuses on studying ordered arrays of mesoscopic superconducting Nb islands on top of Au, determining the dependence of the transition to superconductivity on the island volume and spacing, and characterizing the vortex dynamics in these arrays. Research on such systems is of both fundamental and technological interest. Through straightforward, relatively simple transport measurements, we can probe a rich array of mesoscale phenomena. Moreover, using lithographic techniques, we can fabricate a wide range of geometries. This tunability makes it easy to study competition between dissipation, localization, disorder, Coulomb repulsion, and Cooper attraction. In fact, a strong motivation for this study is that similar competition exists in many 2D systems, namely graphene, topological insulators, 2D electron gases, and layered high-temperature superconductors. We will discuss the consequences of this competition on global and local states, i.e., phase transitions and phase separation, in 2D systems in the discussion below. We will also introduce dissipation, localization, and the role of vortex dynamics.

I. **Dissipation**

Any process that causes a system to irreversibly lose energy is considered dissipative. Electrons in a normal metal dissipate, or lose energy as heat, through electron-electron interactions. In a superconductor, dissipation may depend on the quasiparticle density of states and relaxation time of a vortex core[9]. Intrinsic sources that affect 2D superconductors include moving vortices, separation of Cooper pairs into quasiparticles

near vortex boundaries, and Joule heating inside vortex cores. Dissipation can be extrinsically introduced through shunt resistances between superconducting grains or islands. In the samples discussed in this thesis, the underlying metal Au layer introduces known dissipation by coupling in free fermions, which may affect the amplitude and/or phase of Cooper pairs [2].

Dissipation can introduce energy in the form of electrical resistance, thus locally destroying superconductivity, and catalyzing the transition to the normal state. However, it is not always detrimental to superconductivity. In fact, up to a critical value, it enhances superconductivity in Josephson junction arrays by suppressing fluctuations in the phase of the order parameter. This was observed in two-dimensional arrays of Josephson junctions capacitively coupled to 2DEG heterostructures that served as a source of dissipation [10]. Moreover, quantum phase slips are thought to destroy superconductivity in nanowires in the absence of some dissipation [11].

II. **Phase Transitions, Phase Separation, and Localization**

In this section, we will briefly discuss our motivation behind studying phase transitions, phase separation, and localization in superconductor-normal-superconductor arrays as well as provide a brief literature review on studies of Josephson junction arrays. The physics of these systems will be discussed in detail in Section 1.6.

Characterizing 2D superconductor-normal-superconductor (SNS) arrays could shed light on phase transitions in 2D superconducting films. In fact, granular films may be better understood by studying a lattice of superconducting islands rather than comparing them to predictions for continuous films [12]. Two-dimensional superconducting systems are known to undergo a vortex-antivortex binding transition to the superconducting state at a critical temperature. By tuning the island spacing in our arrays, we tune this transition temperature and compare the resulting spacing dependence of the critical temperature to proximity effect models. Our results differ from such models; these models are limited in scope due to a limited number of systematic experimental studies of the geometry dependence of the superconducting behavior in SNS arrays. However, our results could also prove supplemental to the far more extensively studied disorder- and field-tuned superconductor-insulator transitions (SIT) in thin superconducting films. Some of these studies provide evidence of Cooper pairs in the insulating state, indicating that these systems should be considered phase separated — composed of mixed conducting and insulating phases. In fact, a mosaic of states has been directly observed in high-temperature superconducting films by means of scanning tunnelling microscopy [13].

Phase separation models may more accurately characterize the ground state in 2D superconducting systems. Our system, which is phase separated by design, is an excellent test-bed for such models. These

models could further illuminate the microscopic underpinnings of macroscopic phenomena. In some phase separation models, disorder is treated as the main catalyst for phase separation[5,14–16]. One of these models, proposed by Spivak *et al.* in 2008, can be most easily compared to our system. This model predicts that dilute arrays of superconducting islands coupled to a thin normal metal will exhibit a zero-temperature metallic state. The existence of such 2D, zero-temperature metallic states is controversial; they are precluded by Anderson's venerated scaling theory of localization. However, 2D electron gases in semiconductor heterostructures[1] and disordered ultrathin metal films[2,3] have shown evidence of metallic ground states. These experimental observations may not pertain to conventional metals, but rather to spatially inhomogeneous superconducting states[4,5,16]. In this research, we directly test Spivak's prediction.

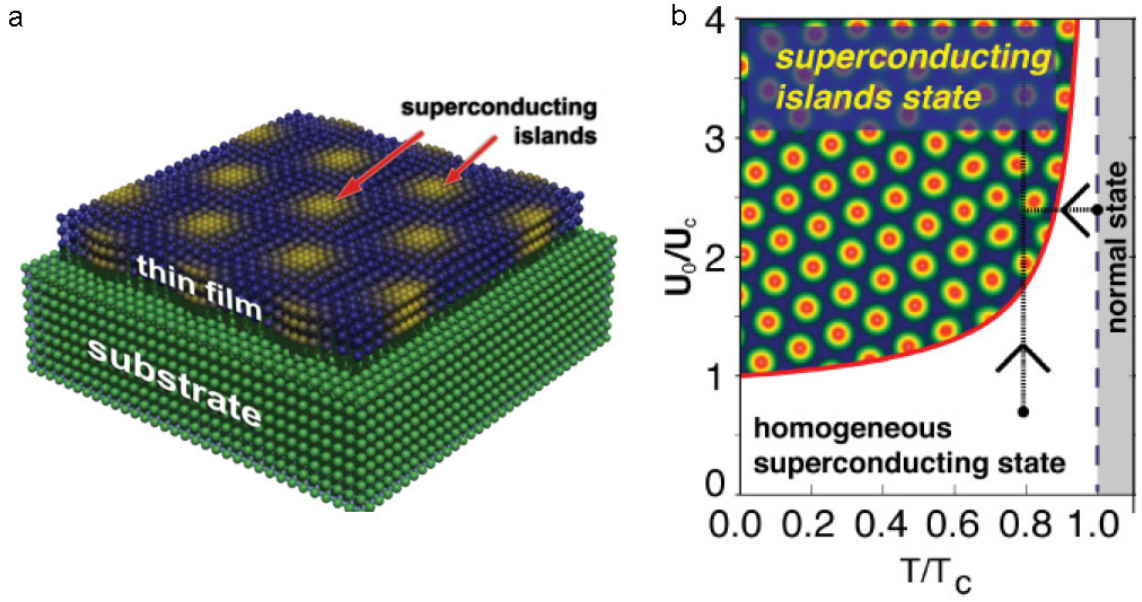

Figure 1.1: **Phase Separation in Superconducting Films on a Rigid Substrate**. (**a**) A regular array of superconducting islands is thought to naturally form in superconducting films due to deformation caused by a lattice mismatch between the film and the substrate. (**b**) The resulting phase diagram, where U_0/U_c is a normalized coupling constant characterizing the mechanical stresses experienced by the films, and T/T_c is the normalized temperature. Images extracted from Glatz *et al.*[17].

Another notable phase separation model, formulated quite recently, proposes that a regular array of superconducting islands can naturally form under certain circumstances when superconducting films are cooled[17]. This self-organization is caused by the interplay between the superconducting order parameter and elasticity; the elastic coupling results from mechanical stresses the thin film undergoes upon cooling due to its attachment to a rigid substrate. Consequently, our research on arrays of superconducting islands could have broad implications for studies on all thin film-based superconducting films and devices.

III. **Vortex Dynamics**

Vortices arise from local variations in the phases of the superconducting order parameters. This could be differences in the phases between neighboring superconducting islands or grains; these whirlpools of current can also form around defects in superconducting films. As natural thermal excitations in 2D superconducting systems, vortices can also be introduced by applying a magnetic field. Given the dependence of vortex dynamics on device geometry, our tunable arrays are a great means for studying correlated vortex motion and competing magnetic ground states. Moving vortices induce dissipation, strongly affecting the properties of superconducting devices. So, in addition to the broad implications our results could have on our understanding of fundamental phenomena, it could have a fairly direct impact on superconducting electronics.

IV. **Technological Applications of Research on Josephson Junction Arrays**

The relentless pace of advancements in computing technologies was most famously epitomized by Moore's Law in 1965. Forty years later, Dr. Gordon Moore commented that "Moore's Law is a violation of Murphy's Law. Everything gets better and better" [18]. Perhaps he overstated. Though Moore's Law bodes faster circuits, device miniaturization pushes electronics from the realms of semiclassical theory to quantum mechanics, where decoherence caused by dissipative coupling to the environment can often plague device reliability. This is an unrelenting issue in research on superconducting qubits, which may ultimately form the building blocks of a quantum computer due to advantageous properties such as flux quantization and Josephson tunnelling. In general, the interplay between decoherence and dissipation has not yet been resolved.

Qubits are not the only electrical elements that could benefit from extensive studies of SNS arrays. Our research could also impact the design of detectors comprised of superconducting circuitry. For example, NbN is one of the most popular materials used for single photon detectors due to its short electron-phonon recombination time. As a strongly type-II superconductor, vortex states play an important role in determining the properties of NbN. As will be clear from our results, SNS arrays behave as type-II films [19] and are an ideal medium for observing vortex phases. In fact, like dissipation, vortices can have either stabilizing or deleterious effects on superconducting devices; the role is not fully understood.

1.2 Introduction to Thesis Problem

In this thesis, we report our studies on triangular arrays of superconducting Nb islands on a normal metal Au underlayer. Our primary goal is to characterize the proximity effect in these arrays though a systematic

study of changes in the superconducting transition as we change the array lattice constant. Due to the conspicuous role of vortex dynamics in the properties of these arrays, we further systematically investigate vortex configurations in response to thermal excitations, current biases, and field sweeps.

In Chapter 2, we will discuss sample fabrication and the measurement set-up. We first evaluated numerous candidates for superconductor-normal metal combinations and developed a process for fabricating these devices. These issues are interdependent and are discussed in Sections 2.1 and 2.2. Though Nb islands on Au proved ideal, we did also successfully fabricate and measure Al islands on Au and have presented some of these results in the Appendix.

All results presented here were extracted from low-temperature transport measurements. Three different measurement systems were essential to capture phase transitions in these arrays, as each system has a limited accessible temperature range. Given the choice of Nb, arrays with a wide range geometries underwent transitions at temperatures ranging from 9 K down to $\sim$ 200 mK. Further, to exclude effects from thermal fluctuations, it was necessary to perform measurements at temperatures down to 15 mK. In Section 2.3, we describe our experimental set-up to access these temperatures and perform low-noise transport measurements.

Upon cooling, the arrays experienced a two-step transition to a superconducting state. The first transition occurs when the individual islands become superconducting; the second transition marks superconductivity across the array. We present and qualitatively discuss these transitions in Chapter 3 and develop a phenomenological model, presented in Section 3.3.1. The changes in the first transition with an increase in island spacing were profoundly different than results from previous experimental studies of SNS arrays and predictions of proximity effect theories. This transition is extensively discussed in Chapter 4.

In Chapter 5, we discuss the second drop in resistance. Superconductivity in 2D systems is typically characterized by bound-vortex antivortex pairs. We present evidence of this type of transition in our arrays and evaluate the trend in the critical temperatures with changes in the island spacing. In Section 5.5, we compare the overall results to proximity effect and phase separation theories. As we continue to increase the island spacing, the arrays no longer superconduct, possibly becoming metallic at zero temperature. The most dilute array may even become insulating. Results for dilute arrays are presented in Section 5.6, as well as a discussion of possible origins of the low temperature resistance.

To further characterize the phases in these arrays, we present an analysis of the current-voltage characteristics. We achieve this by both analyzing the shape of the curves and the critical currents. The temperature-dependence of the critical currents can tell us about the type of proximity coupling between islands and between grains within the islands. The zero-field IV characteristics are presented in Sections

4.4 and 5.4.

External magnetic fields induce vortices in the arrays. In Chapter 6, we will present the effects of applying a perpendicular magnetic field to these arrays. Our results in finite fields are quite striking; both the magnetoresistance and IV curves show a rich structure. In response to a swept magnetic field, the resistance shows strong, periodic oscillations. This manifestation of magnetic frustration is presented in Section 6.1. It has been observed previously in arrays of Josephson junctions and can be definitively explained as due to competing magnetic ground states. Though the origin of these oscillations is known, the intricate details behind the vortex rearrangement is not completely understood. As the magnetic field is swept to high values, the magnetoresistance oscillations disappear, then there is a distinct two-step transition to the normal state. This two-step transition and hysteresis in the magnetoresistance are presented in Section 6.2. The origin of this hysteresis is not understood.

For certain values of magnetic field, field-induced vortices are weakly pinned to the SNS array lattice. Sweeping the temperature can depin these vortices. We present results showing two types of thermally induced vortex depinning: smoothly-depinning transitions are discussed in Section 6.3 and a series of sudden, depinning transitions are reported in Section 6.4.

In addition to temperature and field sweeps, current biases can drive vortex motion. To supplement our investigation of vortex dynamics in these systems, we present results from and a qualitative analysis of IV characteristics in a finite field in Section 6.5. In dense arrays, the critical current is sensitive to a field; in arrays with farther island spacings, it appears insensitive.

To our knowledge, this is the first thorough, systematic study of the dependence of the proximity effect and vortex dynamics on island spacing and height in SNS arrays. We will begin by presenting relevant background information in the following section. We will start with a basic introduction to superconductivity. To this end, we will discuss how this state is characterized by electron pairing and phase coherence. Afterwards, we will describe the special properties of two-dimensional superconductors, applicable to superconducting thin films and arrays. This includes an introduction to the Berenzenskii-Kosterlitz-Thouless (BKT) vortex-antivortex binding transition, which we will address in more detail in Section 1.6. We will proceed to explain the effects of (a) placing a superconducting thin film in contact with a normal metal, and (b) sandwiching a normal metal layer between two superconducting banks. Understanding the resulting phenomena, respectively referred to as the proximity effect and the Josephson effect, will help us understand the suppression in critical temperature and diffusion of Cooper pairs in our SNS arrays. Section 1.6 will focus on the origin of vortices in SNS arrays, and subsequent predictions due to vortex dynamics in similar systems. However, the physics of our devices cannot be fully explained by current theories. In Chapter 3, we will present a

phenomenological model we developed to characterize our unique system. Please note that throughout the thesis, we will expand upon the background information provided in Chapter 1.

1.3 Introduction to Superconductivity

Through Drude, we saw electrons characterized classically as non-interacting pinballs rebounding off immobile ions. But this was inadequate. To satisfy quantum mechanics, Bloch later described electrons as plane waves modulated by the periodicity of the lattice. This was a huge milestone in understanding conduction, yet failed to predict the loss of resistance that characterizes superconductivity. Bloch once joked that " in the absence of external fields, every theory of superconductivity can be disproved." Yes, superconductivity stumped even the greatest contributors to early theories of conduction in metals.

In 1950, Leon Cooper asserted that electrons form pairs when lattice-mediated, attractive electron-electron interactions outweigh Coulomb repulsion at a temperature T_p. These so-called Cooper pairs can be considered bosons of charge 2e. The Cooper pair size is known as the coherence length ξ. Pair formation and phase coherence are prerequisite for superconducting long-range order. To characterize this order, Ginzburg and Landau proposed the complex order parameter $\Psi(r) = |\Psi_0|e^{i\phi(r)}$. Seven years later, John Bardeen, Leon Cooper, and Robert Schrieffer formulated a microscopic theory describing the mechanism behind Bose condensation of Cooper pairs, known as the BCS theory. BCS recognizes the order parameter as a single-particle, singlet wavefunction mapping the position of the center of mass of a Cooper pair. Breaking a Cooper pair into two quasiparticle excitations requires a minimum energy of $E_g = 2\Delta(T)$, where $\Delta(T)$ is the energy gap. For temperatures T near T_c, the energy gap is $\Delta(T) \propto k_B T_c \sqrt{1 - \frac{T}{T_c}}$.

Unlike fermions, bosons are not bound by the Pauli Exclusion Principle. When these Cooper pairs phase lock into a macroscopically occupied single quantum state at T_{co}, a dissipation-free supercurrent persists. Given that phase and particle number N are conjugate variables, the equivalent uncertainty principle for superconductors is $\Delta N \Delta\phi \geq 1$. When bosons are in an eigenstate of phase (phases lock), the system superconducts; an eigenstate of particle number (phase fluctuation) indicates a localized insulator or Bose metal. One can expect pair formation to occur at $T_p \approx \frac{1}{2k_B}\Delta_0$ and phase coherence at $T_{co} \approx \frac{1}{2}\frac{\hbar^2 n_s}{m*}\xi^{\mathcal{D}-2}$, for $n_s \propto |\Psi|^2$ is the superconducting electron density, $m^* = 2e$ is the effective mass, and $\mathcal{D}$ is the dimension[20]. Hence, superconductivity manifests at $T_c \leq min[T_p, T_{co}]$.

1.4 Superconductivity in 2D

Films of thickness less than the superconducting coherence length ξ_S are considered considered quasi-2D. In 2D superconductors, thermally-activated phase fluctuations of 2π produce a vortex, a whirlpool of circulating supercurrents shielding a normal core. Due to these fluctuations in the phase of the superconducting order parameter throughout the film, true long-range order cannot exist in two dimensional systems. However, quasi-long range order (decaying as a power law) can exist when these vortices are pinned, allowing "topological" superconductivity[21]. As a system is cooled below a critical temperature T_{BKT}, the lower energy of bound vortex pairs becomes thermodynamically favorable over the higher entropy of free vortices. This binding of vortices and antivortices, which have opposite vorticity, is called the Berezenskii-Kosterlitz-Thouless (BKT) transition. It has been observed in superconducting granular thin films[3,22–24] and Josephson junction arrays[19,25,26]. In Section 1.6, we will further describe the origin of the BKT transition, and the derivation of the theoretical transition temperature T_{BKT}, all in the context of SNS arrays.

Thin films of a superconducting material do not always superconduct. Disorder and magnetic fields can cause these films to be insulating. Disorder is inherent to thin films and is typically controlled by the film thickness. It localizes electrons to small regions in a sample, enhancing effective electron-electron repulsion, competing with Cooper pairing. A prominent theory addressing phases in disordered 2D superconducting films, known as the "dirty boson model", was first proposed by M.P.A. Fisher[27]. In this model, phase fluctuations caused by disorder can disrupt quasi-long-range order, and Cooper pairs become localized due to Coulomb repulsion. Localized Cooper pairs and de-localized vortices then exist in the newly formed insulating state, referred to as the Bose glass state. A superconducting state can be recovered if Cooper pairs are de-localized and vortices localized; this is the so-called vortex-glass phase. The phase diagram associated with the dirty boson model is shown in Figure 1.2a. This model predicts that the critical determinant of the transition between the superconducting and insulating state is the sheet resistance $R_\square$, and that a superconductor-to-insulator transition (SIT) occurs when $R_\square \approx R_Q$, where $R_Q = \frac{h}{4e^2} \approx 6.45$ kΩ is the superconducting resistance quantum. R_Q is the minimum contact resistance which arises from the mismatch in electronic modes of the contacts and sample. A SIT at R_Q has been confirmed in many thin films[28,29] and arrays of Josephson junctions[30,31], however, this is criteria is not universally true.

Figure 1.3 shows examples of SITs in superconducting thin films. The first plot (Figure 1.3a) shows an example of a disorder-tuned SIT in Bi thin films at a critical resistance R_Q. In this case, the disorder is tuned by changing the thickness of the films.

As previously mentioned, the SIT can also be tuned by an external magnetic field[27]. In the dirty boson picture, above a critical field H_c, vortices delocalize and Cooper pairs localize (a Bose-glass phase). Increasing

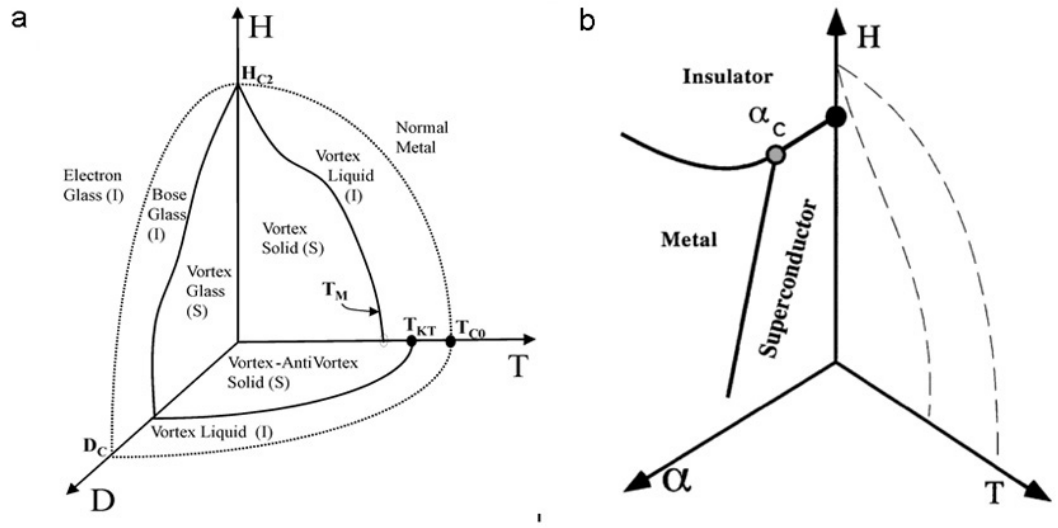

Figure 1.2: **Phase Diagrams for Superconducting Films**. (**a**) The Dirty Boson Model: The expected phase diagram for the 2D SIT. The axes show magnetic field H, temperature T, and disorder D. (**b**) Dissipation incorporated into the H-T phase diagram for 2D superconducting films of finite disorder[15]. The dashed lines represent mean field transitions.

the magnetic field will eventually dissociate Cooper pairs, which can fully suppress superconductivity. An example of a field-tuned SIT in MoGe films is presented in Figure 1.3b.

Although there has been evidence supporting various aspects of the dirty boson model, it remains controversial. For example, the transition to the insulating state in MoGe films is sample dependent[32]; it does not occur at $R_\square \approx R_Q$. Furthermore, though Hall and magnetoresistance measurements in amorphous InO_x[33] and TiN_x[34] films found evidence of a Bose insulator, tunnelling measurements in quench-condensed Bi films support the appearance of a Fermi insulator[35]. In these Bi films, the amplitude of the order parameter (energy gap) approaches zero near the SIT, signifying the breaking of electron pairs, while in a Bose insulator the energy gap is expected to remain finite through the transition[36].

Further evidence that the dirty boson model is incomplete has been the observation of a low temperature metallic state that seems to intervene between the superconducting and insulating states[37]. Figure 1.3 includes plots of this indirect SIT in (b) MoGe films and (c) Ga films. Perhaps the oldest and most notable observation of a possible 2D $T = 0$ metallic state was in Al, In, Ga, and Pb granular films by Jaegar *et al.*[24]. Studying ultrathin (tens of angstroms in thickness) films, they observed a disorder-tuned superconductor-to-insulator transition. The resistive transitions in the Ga film are shown in Figure 1.3c. In all films, the evolution from the superconducting to the insulating states spanned an interval of only a few angstroms. Additionally, the SIT occurred at a critical resistance $R_c \sim R_Q$, consistent with predictions from the dirty boson model. However, there was an intervening anomalous metallic state.

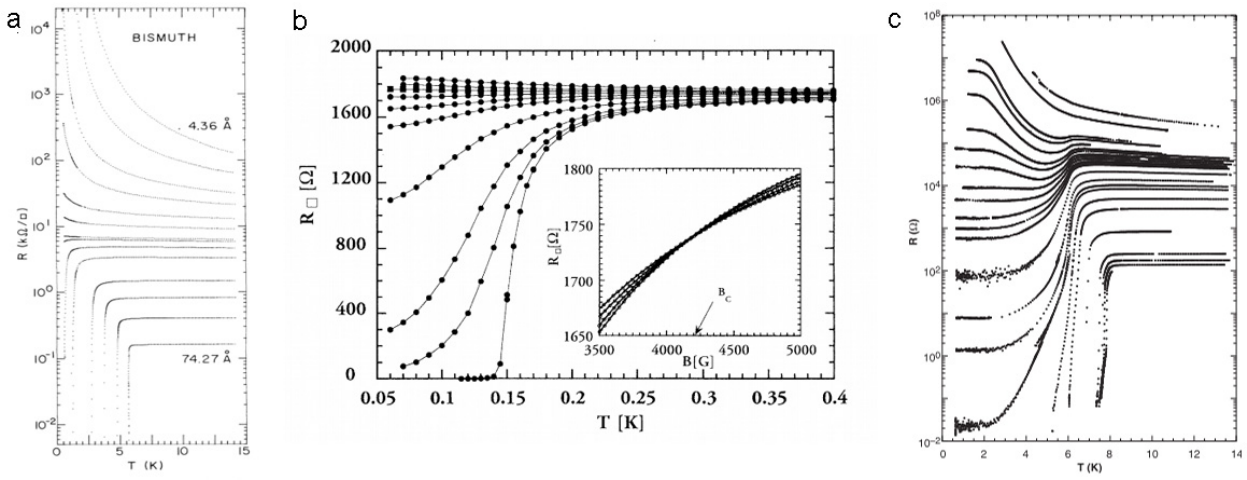

Figure 1.3: **Superconductor-Insulator Transition**. (**a**) Thickness-tuned SIT in Bi thin films[28]. Note that the critical resistance at the transition is R_Q. (**b**) Magnetic field-tuned SIT in disordered MoGe thin films[32]. Note that the critical resistance is not R_Q, evidence that the dirty boson picture is incomplete. (**c**) The disorder-tuned SIT in Ga films. Films thicknesses range from 12.75 Å (insulating) to 16.67 Å (superconducting) from top to bottom. The flattening of resistance at finite values as $T \to 0$ demonstrates an intervening metallic state[24].

Philips *et al.* proposed the phase glass model as a candidate to explain intervening metallic states in the superconductor-insulator transition[37]. In this model, disorder in the Josephson tunnelling amplitudes between superconducting islands and quantum fluctuations prevent phase coherence. The phase glass state, schematized in Figure 1.4, is characterized by "frozen" local phases on each island; the phases are not fluctuating and are fixed in different directions.

Kapitulnik *et al.* attempted to explain the intervening metallic states as due to dissipation[15]. The parameter $\alpha \propto \frac{h}{e^2 R}$ was introduced to represent strength of coupling to a dissipative background of delocalized fermions[38]. Dissipation was then incorporated into the recognized *H-T-D* phase diagram for homogeneous films, shown in Figure 1.2b, and studies were performed on amorphous MoGe capacitively coupled to a ground plane[39]. The ground plane, which acted a source of dissipation, seemed to enhance superconductivity; Figure 1.5 shows these results.

In the aforementioned studies, the actual mechanism behind dissipation was not explored. In light of this, the original goal of this research project was to characterize and parametrize dissipation in thin superconducting films, and more clearly understand what may cause such metallic states. Our underlying normal metal acts as a well-coupled source of dissipation, while tuning the island spacing would tune the amount of dissipative coupling per island. Though we have observed many novel effects in our Nb-Au system, no specifically dissipation-driven effects have yet been pinpointed. However, dissipation could be responsible for some of our anomalous results; our data warrants further analysis beyond the scope of this thesis.

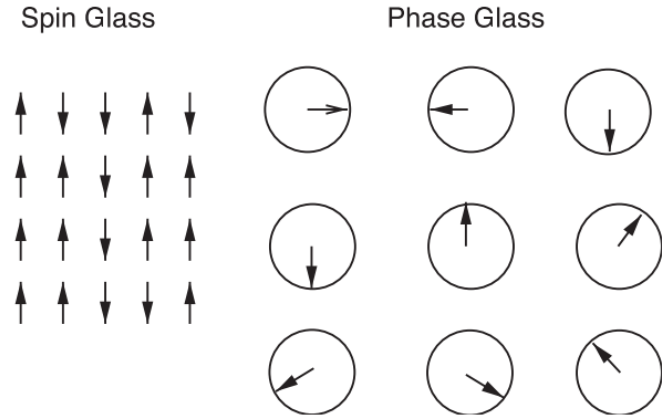

Figure 1.4: **Phase Glass**. A comparison of spin and phase ordering in a spin glass and a phase glass. In the former, the net magnetization is zero despite the randomization of the spins. In a phase glass, the phases have an extra degree of freedom, pointing randomly in the x-y plane. Figure extracted from Phillips *et al.*[37].

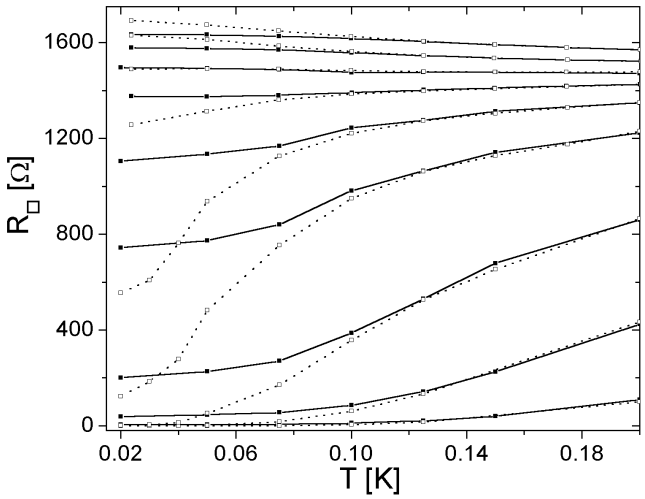

Figure 1.5: **The Effects of Dissipation on Phase Transitions in Amorphous MoGe**. Temperature-dependent resistance curves for MoGe films under different applied, perpendicular magnetic fields. The highest resistance curve represents results taken at the highest field, and each curve underneath shows results for progressively lower fields. The dotted lines represent films coupled to a dissipative source (ground plane). The effects of the dissipative source become measurable precisely as the system crosses into a metallic phase. Figure extracted from Mason *et al.*[39].

1.5 Superconductor-Normal Metal Bilayers: The Proximity Effect

The superconducting proximity effect describes the phenomena that occur when a superconductor is in contact with a normal metal. Cooper pairs from the superconductor tunnel or diffuse into the bordering normal metal, and single electrons from the normal metal diffuse into the superconductor, up to distances equivalent to their respective coherence lengths $\xi_{\mathrm{N,S}} = \sqrt{\frac{\hbar D_{N,S}}{2\pi k_B T}}$, where $D_{N,S}$ are the respective diffusion constants. The mechanism behind this is a process called Andreev reflection. In the Andreev Reflection picture, an electron from one superconducting island enters the normal metal. If the electron has energy ε above the Fermi energy, $\varepsilon < \Delta$, it is retroreflected as a hole at the normal-superconductor interface. A Cooper pair is then formed in the second superconducting island, and the retroflected hole gains energy eV from the voltage bias as it crosses the normal metal. The Andreev pair (incident electron/retroreflected hole) carries information about the macroscopic phases of the superconducting islands and energy scales.

The proximity effect has been well-studied in bilayers of Pb-Cu[40,41], Pb-Pt[41], Pb-Ag[42–45], Nb-Cu[46], Nb-Ni[46], Nb-Zr[47], and Nb-Au[48]. The critical temperature in SN bilayers is expected to be suppressed in accordance with the DeGennes-Werthamer theory[49], which derives a formula for this suppression. This model proved accurate to explain the suppression in T_c in experiments on S-N bilayers, and was subsequently used to derive the Cooper-limit relation: $T_c \propto e^{(\beta z_n + z_s)/(-\lambda z_s)}$, where $z_{n,s}$ is the thickness of the normal metal (N) or superconducting (S) layers, λ is the electron-phonon coupling constant, and β depends on the Fermi velocities of the N and S layers and interlayer coupling[43]. This approximation is less unwieldy and is applicable when the thickness of the layers are less than or on the order of the their respective coherence lengths. Our Nb layers are typically thicker than $\xi_{\mathrm{Nb}}(0)$ and on the order of $\xi_{\mathrm{Nb}}(T \approx T_c)$; we find the Cooper-limit relation accurate enough for our purposes:

Considerations of proximity length scales helped determine the relative thicknesses of our superconducting and normal metal layers, as well as the spacing of our superconducting islands. Figure 1.6 shows our results for superconducting transitions in three different four-point pattern shaped Nb-Au bilayers. Given that the films thickness $z_s \gtrsim \xi_{\mathrm{Nb}}$, the films were not in the 2D limit, thus a BKT-fit would not be appropriate. So, we extracted the T_c from fitting the curves to the Aslamazov-Larkin prediction[50]. In this theory, fluctuations in the amplitude of the superconducting order parameter accelerate superconducting pairs above T_c. This creates excess conductivity. By incorporating how this excess conductivity rounds the transition, Aslamazov and Larkin found that the temperature-dependent conductivity for films is expected to be $\sigma(T) \propto \frac{e^2}{16\hbar z_s}\frac{T}{T-T_c}$. This form fits the data well. The inset shows the extracted critical temperatures T_c plotted versus Nb

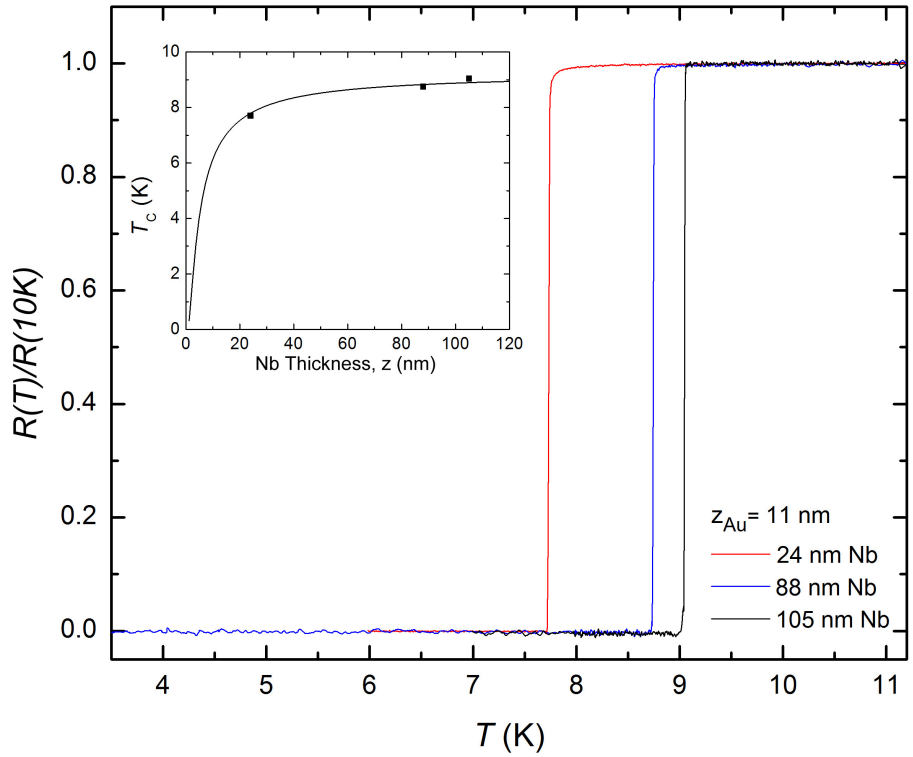

Figure 1.6: **Superconductivity in Nb-Au Bilayers**. Each bilayer was on a separate SiO_2 substrate; each substrate held six identical bilayers to test the reproducibility of the results. All samples were fabricated using photolithography to define the four-point patterns, and electron-beam evaporation in an ultra-high vacuum system (10^{-10} torr); the Nb and Au evaporations were performed sequentially without breaking vacuum. The thickness of the Au was 11 nm for all devices and the thickness of the Nb varied – 24 nm, 88 nm, and 105 nm. Four-point measurements of the resistance were taken using a lock-in amplifier with the sample mounted in a pumped ^{4}He cryostat. The **inset** shows the T_c versus Nb thickness, where the solid line is the fit to the Cooper limit approximation for the DeGennes-Werthamer prediction for suppression of the T_c in SN bilayers.

thickness. The solid line is a fit to the Cooper-limit relation. Note that for $z \gtrsim 50$ nm, the T_c of the bilayer is barely suppressed from that of bulk ($z \to \infty$) Nb.

1.6 Josephson Junction Arrays

When two superconductors are separated by a normal metal or insulator of length less than ξ_S, Cooper pairs tunnel or diffuse through the non-superconducting barrier without an applied voltage. In these so-called Josephson junctions (JJ), the supercurrent $I_s = I_c \sin \Delta\phi$ is related to the difference in phases of the order parameters of the superconducting banks $\Delta\phi = \frac{2eV}{\hbar}$, where V is the voltage, and I_c is the maximum current that a superconductor can carry with zero resistance. A similar effect occurs when the superconductors

are separated by an insulator, SIS, or by a superconducting material too thin to sustain superconductivity, considered a weak link (effective SNS junction). When our superconducting islands are closely-spaced, they act as arrays of SNS Josephson junctions.

Phase transitions in and transport properties of SNS arrays are largely determined by the dynamics of vortices in these systems. These topological excitations arise from fluctuations in phases $\phi(r)$ of the superconducting order parameter $\Psi(r) = |\Psi_0|e^{i\phi(r)}$, and the subsequent Josephson supercurrent that flows between the superconducting islands in the array. This section will set the backdrop for the energy landscape in SNS arrays. This will later help us understand the temperature-dependent transition to the superconducting state, and the effects of an applied current and magnetic field in our arrays.

The supercurrent through a junction is given by the current-phase relation:

$$i_s = i_c \sin(\phi_j - \phi_i - \frac{2e}{\hbar}\int_i^j A \cdot dr) \equiv \sin\gamma_{ij}, \tag{1.1}$$

where A is the vector potential and ϕ_i represents the phase of the i^{th} island. The voltage across a junction is $V_{ij} = \frac{\hbar}{2e}\frac{d\gamma_{ij}}{dt}$, known as the second Josephson equation. Between island i and j, the phase difference is therefore

$$\Delta\phi_{ij} \equiv \phi_j - \phi_i = \sin^{-1}\left(\frac{i_{ij}}{i_c}\right) + \frac{2e}{\hbar}\int_i^j A \cdot dr. \tag{1.2}$$

Summing around a closed path of junctions in a single unit cell, the phase difference changes by $2\pi n$. We call one unit cell of junctions a plaquette and the total flux enclosed $\Phi_{plaquette} \equiv \oint A \cdot dr$. We find that

$$\sum_{junctions} \sin^{-1}\left(\frac{i_{ij}}{i_c}\right) = 2\pi\left(n - \frac{\Phi_{plaquette}}{\Phi_0}\right), \tag{1.3}$$

where $\Phi_0 = \frac{h}{2e}$ is a flux quantum. For small currents $i_{ij} \ll i_c$

$$\sum_{junctions} \gamma_{ij} = 2\pi\left(n - \frac{\Phi_{plaquette}}{\Phi_0}\right). \tag{1.4}$$

Assuming a static system, this leads to a total junction energy

$$H = -\sum_{<ij>} E_J \cos\left(\Delta\phi_{ji} - \frac{2\pi}{\Phi_0}\int_i^j A \cdot dr\right), \tag{1.5}$$

where E_J is the Josephson coupling energy.

In zero magnetic field ($\Phi_{plaquette} = 0$) and at $T = 0$, the energy of the array is minimized when the

phases of all superconducting islands are equal, the $n = 0$ case in Eq. 1.4. However, for finite temperatures, thermal excitations cause fluctuations in the phases of the superconducting islands. These gradients in the phase configurations can be thought of as phase waves, similar to spin waves in an XY magnet[51]. This precludes long-range order in SNS arrays at non-zero temperatures.

For the next lowest energy state, the $n = 1$ case in Eq. 1.4, the phases of the islands vary by 2π in a plaquette. This phase difference induces a vortex. The energy required to add a vortex to an array is $E_v = \pi E_J \ln \frac{L}{a}$, where L is the system size, while the energy of a bound pair separated by a distance r is

$$E_{bv} = \pi E_J \ln \frac{r}{a}. \tag{1.6}$$

As mentioned in Section 1.4, when the temperature of the array is reduced to T_{BKT}, it becomes thermodynamically favorable for a vortex to pair with an antivortex (vortex of opposite vorticity). This transition occurs at T_{BKT} and is defined as the temperature at which the probability of finding a single vortex is negligible. The change in free energy caused by a generated single vortex is $\Delta F = E_v - T\Delta S_v$ such that the probability of finding a free vortex is $P \propto e^{-\Delta F} = \left(\frac{L}{a}\right)^2 e^{2-\pi E_J/(k_B T)}$. This probability drops abruptly when the exponent is zero and the BKT transition occurs at

$$T_{BKT} = \frac{\pi E_J}{2k_B}. \tag{1.7}$$

1.6.1 SIT in Josephson Junction Arrays: Understanding Competition between Josephson Coupling and Charging Energies

As mentioned previously, BKT transitions and SITs have been observed in arrays of Josephson junctions (JJAs). In both JJAs and granular films, the interplay between Josephson coupling energy $E_J = \frac{\hbar I_c}{2e}$ and charging energy $E_C = \frac{(2e)^2}{2C}$ can drive a phase transition. The Josephson coupling energy, which depends on the critical current I_c in the junctions, is the kinetic energy of two superconducting grains through which a Josephson supercurrent flows, whereas the charging energy is due to the capacitance C between the grains. Strong Josephson coupling decreases phase fluctuations while strong Coulomb interactions decrease charge fluctuations.

Section 1.4 discussed disorder and field-tuned superconductor-insulator transitions in thin superconducting fields. SITs have also been extensively studied in arrays of SIS Josephson junctions to shed light on the results for thin films. The SIT in JJAs, especially when metallic shunts are added between the junctions, is relevant to our SNS system. It was previously thought that a SIT in JJAs would occur precisely when

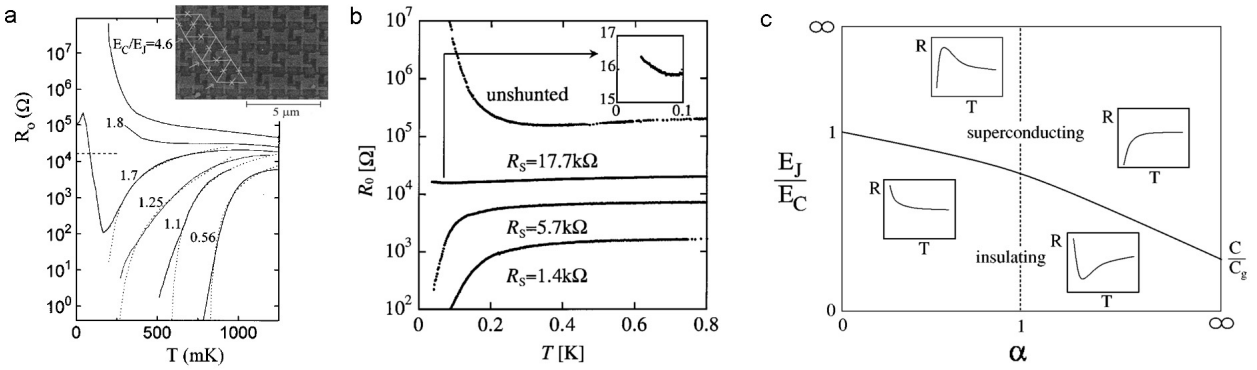

Figure 1.7: **Superconductor-Insulator Transitions in Josephson Junction Arrays**. (**a**) Temperature-dependent resistance for six different JJAs. Each curve represents a different device. The relative E_J/E_C varies between devices and is labelled adjacent to its result. The dotted line indicates a fit to expected results for a BKT transition. The **inset** is a scanning electron microscopy image of the arrays[56]. (**b**) Resistance vs. temperature for shunted JJAs[30]. The ratio $\frac{E_J}{E_C} = 0.13$ is the same in all arrays. The shunt resistance is labelled adjacent each curve. (**c**) Phase diagram for JJAs capacitively coupled to a 2D electron gas[55]. The y-axis shows $\frac{E_J}{E_C}$, while the x-axis shows the dissipative coupling constant α.

$\frac{E_J}{E_C} \approx 1$; the arrays would be superconducting when $E_J \gg E_C$ and insulating when $E_C \gg E_J$. Figure 1.7a shows a superconductor-to-insulator transition in SIS arrays with different $\frac{E_J}{E_c}$ ratios; the transitions occurs fairly close to the expected critical point at $E_C \approx E_J$. However, dissipation can induce an insulator-to-superconductor transition[52] even when $\frac{E_J}{E_C} \ll 1$. Incorporating resistive shunts between junctions in JJAs adds a known source of dissipation to the system. This adds to the intrinsic dissipation from quasiparticles tunneling through the junctions[30,53]. Yagi *et al.*[54] observed a dissipation-driven phase transition for a single JJ for $\frac{E_J}{E_C} \approx 0.1 - 0.2$ when coupled to strong dissipation $\alpha > 1$. Further, Takahide *et al.*[30] compared shunted SIS arrays for which the $\frac{E_J}{E_C}$ ratio was kept fixed at 0.13, but the resistance of the shunts varied. Their results are shown in Figure 1.7b. Dissipation can be in situ tunably added to a system of Josephson junction arrays through capacitive coupling to a two-dimension electron gas. Wagenblast *et al.*[55] produced a phase diagram, shown in Figure 1.7c, of results from such studies.

1.6.2 Previous Experimental Research on SNS Arrays

Few previous studies have been performed on the spacing dependence of superconducting islands in proximity-coupled SNS arrays[19,57]. The goal of the previous studies was to understand the slight broadening in the resistance versus temperature curves for granular superconducting films near the critical temperature. It was thought that this broadening was either caused by a spread in the critical temperatures of the individual grains, or a BKT transition. If studies of regular arrays of artificially homogeneous grains could sufficiently imitate the effects observed in granular films and adhere to predictions for BKT, it would be likely that

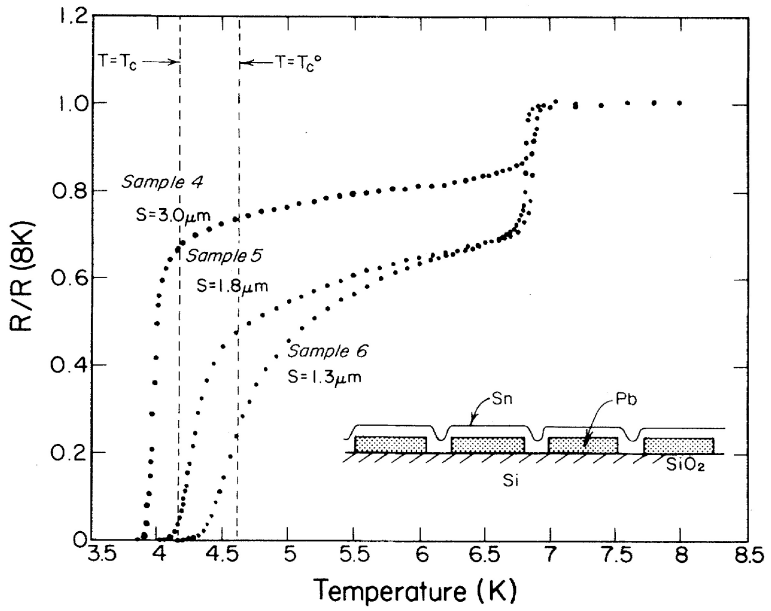

Figure 1.8: **Vortex-Antivortex Binding Transition to Superconductivity in SNS Arrays**. Two-step transitions to superconductivity in arrays of superconducting Pb islands coupled to a normal metal Sn overlayer[19]. The island spacings in each array are labelled as s. All three arrays experience a Berezenskii-Kosterlitz-Thouless transition. The dashed line, labelled $T = T_c$, marks the critical temperature of the array with 1.6 μm spaced islands. To our knowledge, this is the only other study that compared transitions for arrays of different island spacings.

vortex dynamics played an important role in the properties of granular films. These studies utilized large $d \gg \xi_S$ islands and focused on the type of transitions seen in the arrays. Most notably, Resnick *et al.*[19] showed evidence of BKT transitions in square arrays of 10^6 Pb islands coupled by a normal Sn overlayer. Their results are shown in Figure 1.8. The Pb islands were 13 μm-wide and 150 nm in height; the Sn layer was 100-nm thick. Results from three arrays with edge-to-edge spacings of 3.0 μm, 1.8 μm, and 1.3 μm demonstrated a two-step transition to a zero-resistance superconducting state. The high temperature drop in resistance occurred at the same temperature for all arrays; this marked the transition of the individual Pb islands. However, the temperature at which the entire array became superconducting was suppressed in the arrays with farther island spacings. To our knowledge, this is the only previous study in which a comparison was made between transitions in arrays with different island spacings.

Figure 1.9 shows an illustration of the two-step transition to the superconducting state in SNS arrays composed of large superconducting islands. The explanation of each regime, based on Resnick *et al.*, is summarized below:

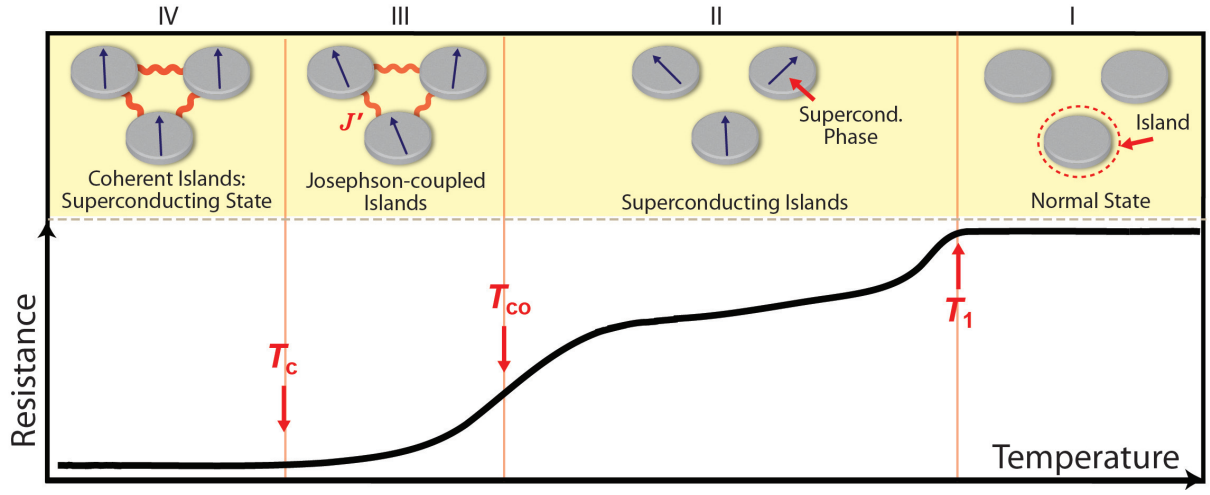

Figure 1.9: **Illustration of Transition to Superconductivity in Arrays of Large Superconducting Islands on a Normal Metal**. The gray circles represent superconducting islands. Black arrows representing the fluctuating phase of the superconducting order parameter in the islands. In region I, the islands are normal metals. In region II, the individual islands are superconducting, but are not Josephson coupled; the system exhibits Ohmic IV characteristics. The resistance drops at T_1 as Cooper pairs diffuse into the normal metal overlayer due to the proximity effect. In region III, the IV characteristics are non-linear due to thermally induced vortex-antivortex pairs. Lastly, the array undergoes a BKT transition and is superconducting in region IV.

- **Region I**

  For $T > T_1$, the individual islands are normal metals. At T_1, the individual islands become superconducting. This transition temperature T_1 is slightly suppressed from that of a continuous Pb film, due to the proximity effect, from the normal metal overlayer.

- **Region II**

  Due to the proximity effect, the effective radii of the islands increases as the temperature decreases. This causes the resistance in the sample to decrease. However, the IV characteristics continue to exhibit Ohmic behavior; thermal fluctuations inhibit inter-island coupling down to $T = T_{co}$

- **Region III**

  At T_{co}, the islands start to become Josephson coupled. At temperatures below T_{co}, though the sample is still resistive, it exhibits non-linear IV characteristics due to thermally induced vortices and antivortices.

- **Region IV**

  At T_c, the system exhibits a transition to a fully superconducting state. Bound vortex-antivortex pairs form, consistent with a BKT transition.

In response to Resnick's study, Lobb, Abraham, and Tinkham (LAT) [12] composed a proximity effect theory, from which predictions can be made regarding the spacing dependence of the BKT transition temperatures in such arrays. Their work bolstered early claims that the Berezenskii-Kosterlitz-Thouless transition not only applied to neutral superfluids, but also to 2D superconducting films. We will discuss LAT in detail in the next section.

1.6.3 Models of Superconductor-Normal Metal-Superconductor Arrays

Global superconductivity in SNS junctions is typically described using the phenomenological theory of Lobb, Abraham, and Tinkham (LAT) [12]. Using a superfluid density that considers the Josephson coupling energy of the islands, they formulated a model that could be exploited in experiments; its predictions are based on easily measurable parameters. The temperature dependence of the superfluid density will differ from the Ginzburg-Landau prediction for a continuous film. Instead of varying linearly with $T_{co} - T_c$, where T_{co} is the Ginzburg-Landau transition temperature, it will depend specifically on the temperature dependence of the critical current $i_c(T)$. According to LAT, for SNS junctions, the critical current at temperatures near the transition $T \approx T_2$ is expected to exponentially decrease with the ratio of the spacing to the normal metal coherence length $i_c(T_2) \propto e^{-d/\xi_N(T_2)}$. Accordingly, the prediction for T_2 is

$$k_B T_2 \sim J_0' e^{-d/\xi_N(T_2)}, \tag{1.8}$$

where J_0' is the coupling amplitude from the inter-island interaction $J'(T) \approx J_0' e^{-d/\xi_N(T)}$.

Models Predicting a Superconductor-Metal Transition

Phase-separated systems of superconducting grains embedded in normal metals are thought to undergo zero-temperature superconductor-to-metal transitions at a critical superconductor composition [5,16]. This applies to both ordered and disordered arrays of superconducting islands on a normal metal. By stipulating that the localization length is too large to be observable in finite samples with this composition, Spivak *et al.* [16] are able to sidestep the conflict between Anderson localization and the existence of a zero-temperature 2D metallic state. Their model considers the Josephson coupling between puddles i and j as

$$J_{ij} \equiv J(r_i, r_j) \propto C_{ij} \frac{\nu V_i V_j}{|r_i - r_j|^2} e^{\frac{-|r_i - r_j|}{L_T}}, \tag{1.9}$$

where ν is the density of states of the metal, V_i is the area (2D) and r_i the position of the i^{th} puddle, $L_T = \xi_N$ the normal metal coherence length, and C_{ij} is a "complicated dimensionless function of the coordinates" [16].

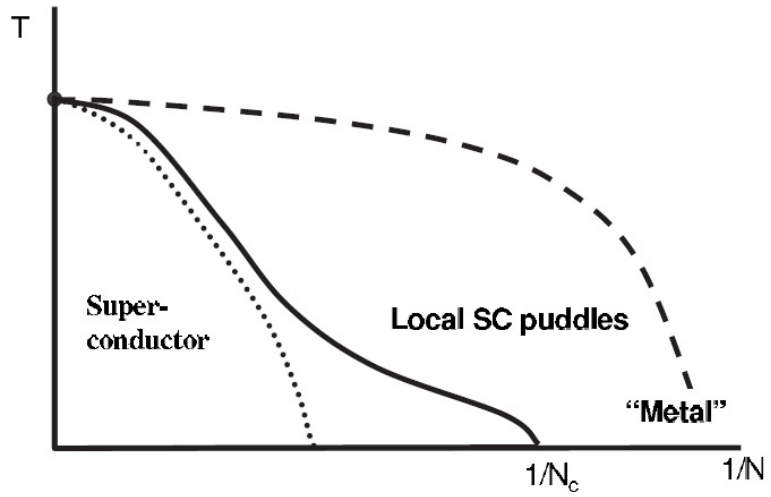

Figure 1.10: **Phase Diagram of Superconducting Grains Embedded in a Normal Metal**. This is a schematic of the Spivak phase separation model, where N is the concentration of superconducting grains and T is the temperature. The solid line represents a phase transition between a superconducting state and an unusual metallic state with local superconducting regions. This figure was extracted from Spivak *et al.*[16].

A phase transition is driven by fluctuations in the modulus of the superconducting order parameter. It specifically depends on both the Josephson coupling energy and island susceptibility $\chi \sim \Delta_0 e^{\sqrt{G}}$. Considering the dimensionless coupling parameter $X_{ij} \equiv \chi_i J_{ij} \chi_j J_{ji}$, two puddles fluctuate independently if $|X_{ij}| \ll 1$ and are phase locked if $|X_{ij}| \gg 1$. Thermal and quantum fluctuations destroy long-range phase coherence. Near criticality, the conductivity diverges and the Weideman-Franz law is violated.

Figure 1.10 is a schematic of the phase diagram predicted by Spivak's theory. The solid line represents a phase transition between long-range superconducting order and the "quantum" metallic state composed of local superconducting regions. In our systems, a signature of this metallic state in transport measurements would manifest itself as either:

(a) a single drop in resistance due to superconductivity in the individual islands, then a flattening of resistance at a finite value as $T \to 0$, or

(b) a two-step transition in which the second drop flattens out a finite resistance as $T \to 0$.

Spivak's model is not the only one directly applicable to our systems. Feigel'man *et al.*[5] considered a triangular array of superconducting islands, in which each island is large enough to support superconductivity $V_i \gg \frac{G_T}{\nu \Delta_{sc}}$. The island volume is V_i, d is the radius, and ν is the density of states. Embedded in a dirty normal metal of dimensionless conductance $g = \frac{\hbar}{e^2 R} \gg 1$, the islands are separated by $b \gg d$. The resistance of the interface between the normal metal and islands is low, $R_T \ll \frac{\hbar}{e^2 G_T}$. Feigel'man deduced that at

$T = 0$ K, the macroscopically superconductive state breaks down in the case of critical geometries and conductances: $g < g_c = (\frac{1}{\pi} \ln \frac{b}{d})^2$ and critical sheet resistance is $R_c = \frac{\hbar}{e^2 g_c} \ll R_Q$ for $\ln \frac{b}{d} \geq 3$. As in the SIT, researchers originally thought that observing *any* phase transition in junction arrays required critical resistance near R_Q. However, in Feigel'man's model, the normal resistance of a system of islands of critical lattice spacing $b = b_c$ was found to be smaller than R_Q. Given this, his model may be applicable to our high conductance system. However, for high normal metal conductance, the critical concentration of islands is expected to be exponentially small.

1.7 The Usadel Equations

Understanding proximity-coupling in Josephson junctions requires understanding how the supercurrent flows. In this section, we will introduce the Usadel Equations. These equations are often applied to describe the behavior of the supercurrent in diffusive heterostructures, as they take into account scattering.

The Gor'kov equations are formulations, in terms of Green's functions, that are based on BCS theory. They are a set of kinetic, non-linear equations and are probably the most complete model of superconductivity. Considering boundary conditions determined by length scales and electromagnetic stimuli, they can describe the macroscopic behavior of the superconducting state. However, the Gor'kov equations are unduly complicated, accounting for parameters that tend to be negligible in experimental systems [58].

Eilenberger and Usadel derived approximations of the Gor'kov equations, applicable in the quasi-classical limit. In the quasi-classical limit, length scales associated with the system, such as the mean free path ℓ in heterostructures, are much greater than the Fermi wavelength. The Eilenberger equations are applicable in the clean limit ($\ell \gtrsim \xi$) and are far less cumbersome than those of Gor'kov [59]. Two years after the Eilenberger equations were formulated, Usadel used them to derive approximations to the Gor'kov equations that are applicable in the dirty limit ($\ell \lesssim \xi_s$), that is, for diffusive systems.

Of all these formulations, the Usadel equations are considered most practical for experimentalists because they consider the diffusive limit, can include interfaces and easily experimentally measurable parameters, and do not include excess parameters that tend to be negligible. Strong impurity scattering randomizes the momentum of quasiparticles; Usadel averaged the system properties over all directions of momentum, leading to isotropic Green's functions. The Usadel equations are as follows:

$$2\omega F(\omega, \vec{r}) - D\hat{\partial}\left[G(\omega, \vec{r})\hat{\partial}F(\omega, \vec{r}) + \frac{1}{2}\frac{F(\omega, \vec{r})}{G(\omega, \vec{r})}\vec{\partial}|F(\omega, \vec{r})|^2\right] = 2\Delta(\vec{r})G(\omega, \vec{r}) \tag{1.10}$$

$$\Delta(\vec{r}) \ln \frac{T}{T_c} + 2\pi T \sum_{\omega>0} \left[\frac{\Delta(\vec{r})}{\omega} - F(\omega, \vec{r}) \right] = 0, \tag{1.11}$$

where $\Delta(\vec{r})$ is the order parameter, $\vec{r}$ the position vector, the Matsubara frequency is $\omega = (2n+1)\pi T$ assuming $\omega > 0$, T is the temperature, and T_c is the critical temperature. The functions G and F are the standard and anomalous Green's functions, respectively. The diffusion constant is $D = \frac{1}{3}\nu_F \ell$, where ν_F is the density of states at the Fermi level and ℓ is the elastic scattering length. The derivative $\hat{\partial} = \vec{\partial} + 2ie\vec{A}(\vec{r})$, such that the effects of a magnetic field can be included. Eq. 1.10 is the main Usadel result and Eq. 1.11 is the self-consistency equation for the order parameter. Usadel also found a form for the supercurrent density:

$$\vec{j_s}(\vec{r}) = 2ieN(0)\pi T D \sum_{\omega>0} \left[F^*(\omega, \vec{r}) \hat{\partial} F(\omega, \vec{r}) - F(\omega, \vec{r}) (\hat{\partial} F(\omega, \vec{r}))^* \right]. \tag{1.12}$$

Other physical parameters[59], such as the free energy and density of states, can be expressed in terms of $F(\omega, \vec{r})$.

In this thesis, we will compare our results to predictions for diffusive 1D wires that are based on the Usadel equations. For convenience, the equations are typically parameterized, *i.e.*, $G \equiv \cos\theta(x)$ and $F \equiv \sin\theta(x)$. In the 1D case, the parameterized Usadel equations become[60]

$$\frac{\hbar D}{2} \frac{\partial^2 \theta}{\partial x^2} + iE \sin\theta - \left[\frac{\hbar}{\tau_{sf}} + \frac{\hbar D}{2} \left(\frac{\partial \phi}{\partial x} + \frac{2e}{\hbar} A_x \right)^2 \right] \sin\theta \cos\theta + \Delta(x) \cos\theta = 0 \tag{1.13}$$

$$\Delta(x) = n_s V_{eff} \int_0^{\hbar\omega_D} dE \tanh \frac{E}{2k_B T} Im[\sin\theta] \tag{1.14}$$

where x is the position coordinate, E is an energy variable that accounts for electron states since k-vectors (*i.e.*, momentum vectors) are no longer eigenstates, τ_{sf} is the spin-flip scattering time, A_x the vector potential, V_{eff} is the BCS-like interaction potential, and $\hbar\omega_D$ is the Debye energy. The first term in Eq. 1.13 accounts for diffusive motion and the second accounts for the energy of the excitation ($\theta = 0$ in the normal state). Pair breaking mechanisms, such as a magnetic field, spin-flip scattering, and current, are all included in the third term. The last term considers pairing interactions.

From these equations, the Usadel formalism then predicts the following equation for the current density for 1D diffusive SNS junctions:

$$j_s = \frac{\sigma_s}{e} \left[\frac{\partial \phi}{\partial x} + \frac{2e}{\hbar} A_x \right] \int_{-\infty}^{\infty} dE \tanh \frac{E}{2k_B T} Im[\sin^2\theta] \tag{1.15}$$

where σ_s is the conductivity.

The Usadel equations themselves are not easy to directly apply to experiment without extensive numerical analysis. However, we can easily use analytical approximations formulated based on limiting regimes (*e.g.* low temperature limit). Dubos *et al.*[61] derived an analytical approximation for the temperature dependent IV characteristics of Josephson junctions using the Usadel equations. This approximation has two free fitting parameters. The fitting parameters depend on the relative gap in the superconductor and diffusion constant in the metal, thus vary based on junction geometry. In Section 5.4, we will fit our $I_c(T)$ to the Dubos form. Similarly, Wilhelm *et al.*[62] also used the Usadel equations to derive an analytical approximation for $I_c(T)$. We will use Wilhelm's low temperature limit ($T \to 0$) form, which has no free fitting parameters, to fit our results on the spacing dependence of the superconducting transition temperature in our arrays.

Chapter 2

Experimental Techniques

2.1 Sample Fabrication

2.1.1 Choosing materials

Selecting Nb as the superconductor and Au as the normal metal involved a very meticulous process. We not only considered a plethora of material combinations, but also tested combinations that failed. The normal metal should be thin enough that, through the proximity effect, Cooper pairs from the superconductor diffuse completely through the underlying metal. This required selecting a metal that, when grown via electron-beam evaporation or sputtering, would coalesce into a continuous layer at a thickness less than that of the normal metal coherence length. Additionally, it should be non-magnetic to prevent obscuring results from effects such as an intrinsic field or the creation of vortex pinning centers around magnetic impurities. The metal should not easily oxidize in air, as a poor interface between the superconducting islands and the normal metal could impede the proximity effect. Lastly, it should not melt or sublimate at $T \lesssim 180$ °C, the required baking temperature of our electron-beam sensitive resist. Gold (99.999% purity) on a titanium sticking layer satisfied these properties.

Ideally, the superconductor should be easy to lift-off, given the desire for closely-spaced features. This required choosing a material that could be electron-beam evaporated, rather than sputtered, and that has a medium-to-low sticking coefficient. Similar to the normal metal, it should not easily oxidize in air and should coalesce at a low thickness during the growth process. Thicker evaporations require thicker electron-beam sensitive resist to enable lift-off. However, closely-spaced features cannot be patterned in thick resist because scattering of the electron beam in the resist and substrate during electron-beam lithography broadens features in a pattern written in thick resist. Furthermore, the superconducting thin film should have a

critical temperature higher than 1 K, which will be suppressed as we pattern it into an array of islands and progressively increase the island spacing. The arrays should have critical temperatures above 15 mK, the lowest accessible temperature in our measurement systems. Niobium, which has a bulk T_c of 9.2 K, satisfied these criteria. Furthermore, the combined superconductor-normal metal should not alloy or diffuse into each other at temperatures near room temperature up to $\sim$ 100 °C; the sample could experience heating during deposition of the superconductor.

We also tried fabricating and measuring Al islands on a thin Au layer. The results are reported in the Appendix. Given that Al is not as easy to lift-off as Nb, and has a significantly lower bulk $T_c \sim 1.1$ K, we were unable to reproducibly fabricate thick, very closely spaced Al islands. Upon studying arrays with farther spacings than those reported in the Appendix, we quickly pushed the T_c below the measurement range of our dilution cryostat. An additional complication was that the samples needed to be cooled within a couple hours of fabrication; at room temperature, the resistance of the arrays would triple within a few hours, stabilizing only after the sample was cooled to 77 K. This is a strong indication of diffusion between the layers.

It is important that the superconductor-normal interface in the arrays is transparent. In Section A of the Appendix, we discuss in detail our attempts at creating a fabrication process with an almost ideal S-N interface. This involved starting with bilayers grown via molecular beam epitaxy. We fabricated an array of a masking material on the bilayer, then attempted to use reactive ion etching to remove the unmasked regions. Given the complications associated with sufficient removal of the superconductor in these regions, we decided instead to use the process specified in the following section.

2.1.2 Sample Fabrication Procedure

We developed a fabrication procedure for triangular arrays of Nb islands on Au that enabled reproducible samples with good superconducting properties. We chose a triangular geometry because, with each island having six equidistant nearest neighbors, it may be a better model of grains in a granular film than an array of square geometry (only four nearest neighbors). Figure 2.1 on page 27 is a schematic of our fabrication process. The details of the procedure are in the Appendix (Section B), but we will provide a summary here.

Standard photolithographic techniques and electron beam evaporation were used to create 10-nm thick four-point pattern of Au with an underlying 4 Å - 1 nm Ti adhesion layer on highly resistive Si substrates. These substrates have a 500 nm thick surface oxide layer. Using electron-beam lithography, triangular arrays of islands were patterned into a bilayer of electron-beam sensitive resists – 950K A2 PMMA on 495K A2 PMMA. Lower molecular weight PMMA (495K is lower than 950K) develops faster, creating a

slight undercut. This undercut makes it easier to remove the subsequently evaporated Nb overlayer. After development of the exposed resist in 1:3 MIBK:IPA, the sample is exposed to a UV/Ozone lamp which burns off resist residue that could contaminate the Nb-Au interface. The sample is then placed in an ultra-high vacuum electron beam evaporator ($\sim 3 - 8 \times 10^{-10}$ torr). An ultra-high vacuum is required to evaporate clean Nb with a reproducible T_c; Nb is very sensitive to oxygen, which creates Nb_2O_5 grain boundaries that lead to a suppression in the T_c. Prior to electron beam evaporation of Nb and without breaking vacuum, approximately 5 Å of the Au surface was Ar^+ ion milled to establish a clean interface. Nb was then evaporated at a rate of 1 Å/s. Nb requires a high power for evaporation and the process transfers significant heat to the deposition system; for devices requiring a layer of Nb thicker than 65 nm, the evaporation was broken up into two evaporations, separated by approximately 30 minutes, to prevent the chamber and sample from overheating.

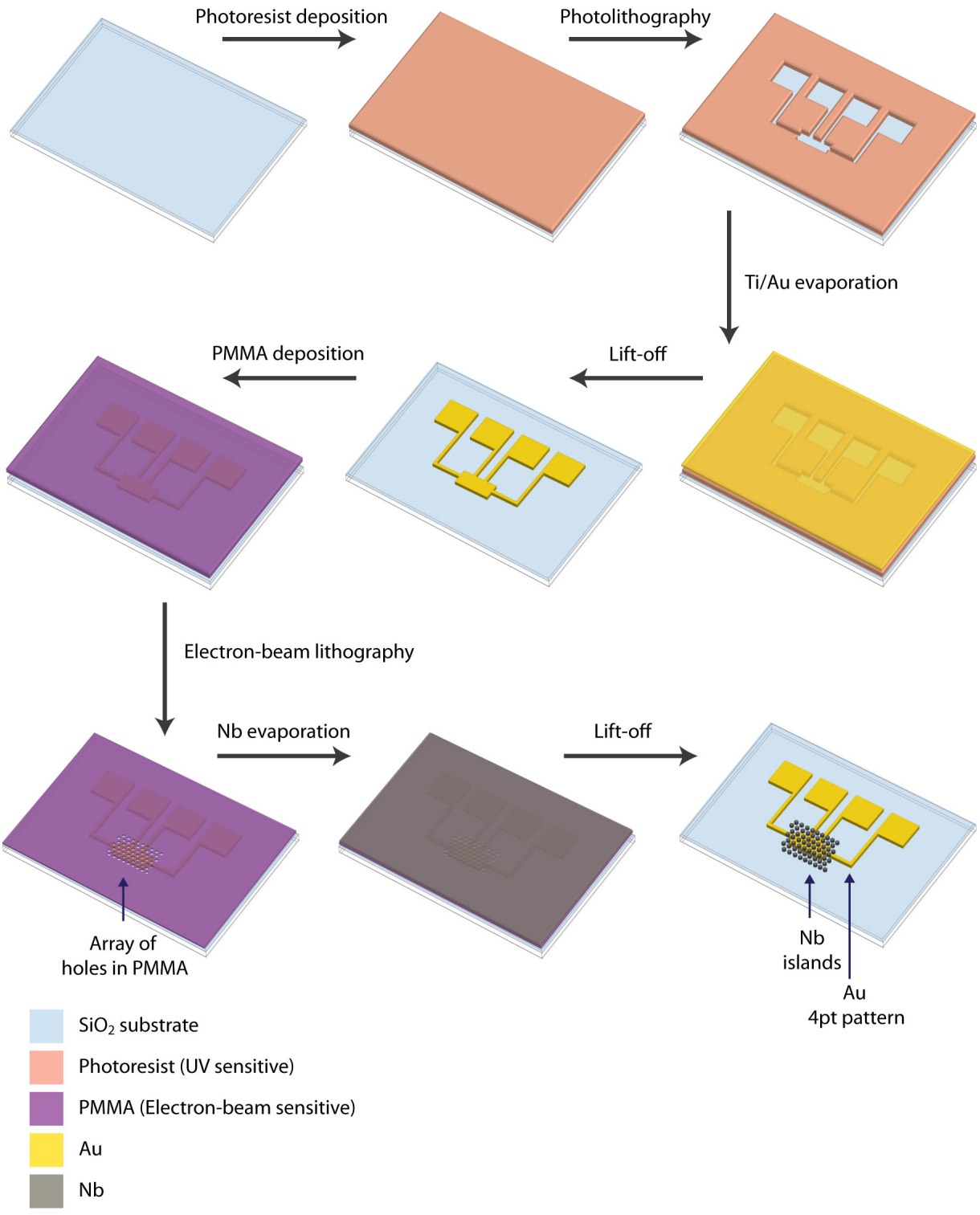

Figure 2.1: **Schematic of the Nanofabrication Process for Nb-Au SNS Arrays**. Six devices are fabricated on SiO_2 substrates using **(a)** photolithography and **(b)** electron-beam evaporation to create the Au four point patterns, **(c)** electron beam lithography to define the array of islands, **(d)** UV/Ozone exposure and ion milling to clean the interface, and **(e)** electron beam evaporation of Nb islands. In this schematic, for clarity, we show only a single device on a substrate.

2.2 Summary of Samples Presented in this Thesis

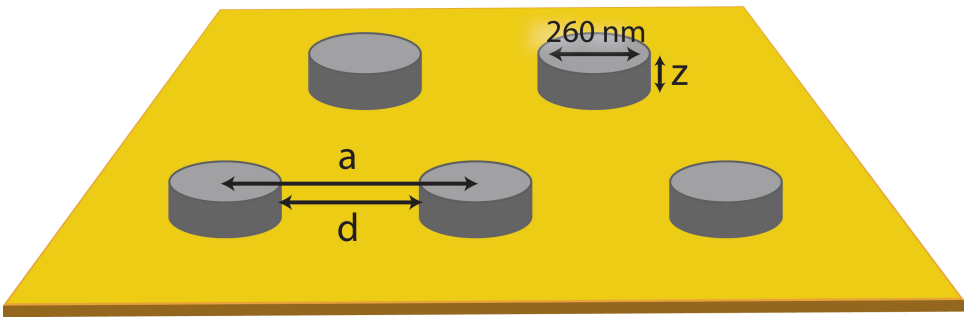

Figure 2.2: **Schematic of Array Geometry**. The arrays reported here have triangular geometry. All islands in all arrays have a diameter of 260 nm. The edge-to-edge island spacing will be represented by d, center-to-center island spacing (array lattice constant) by a, and island height (Nb film thickness) by z.

All Nb islands in all arrays reported here have a diameter of 260 nm. The array geometry is triangular, therefore each island has six equidistant nearest neighbors. Each individual triangular unit cells will be referred to as a *plaquette* of area A. The edge-to-edge island spacings will be represented by d; this spacing is relevant to proximity-effect related phenomena. The center-to-center island spacing (array lattice constant) will be represented by a (simply $d + 260$ nm); this variable will be used in any calculations requiring the unit cell size or number of unit cells, such as magnetic frustration. Each sample (i.e., each individual substrate) can have up to six different arrays. On each sample, the island height z is fixed, but each device has a different lattice constant a. We fabricated and studied many samples with a wide range of geometries: d = 90 – 1240 nm and z = 34 – 145 nm. An atomic force microscope (AFM) was used to verify the sample geometry. Refer to Figure 2.3 for AFM images of arrays with (a) d = 140 nm and (b) d = 340 nm; both arrays have island height z = 87 nm.

Table 2.1 delineates the properties of the main samples from which we present results. (The resistivity of each array, which is used to calculate D, is included in Table B.1 in the Appendix.) The size of the Au rectangle underneath each array on a single sample is fixed. For example, the measurement area of all devices with inter-island spacings of d = 90 nm – 340 nm is 120 μm × 30 μm, so the number of islands in each array ranges from approximately 11,400 to 33,900, depending on the island spacing. For devices with inter-islands spacings of d = 440 nm - 1240 nm, we used a photolithographic mask that produced a larger measurement area of 500 μm × 150 μm, resulting in approximately 38,300 – 155,800 islands per array. The large number of islands ensures that discrete percolation paths, individual junction properties, or edge effects do not dominate the conductance. Figure 2.4 on page 31 is a false-color scanning electron microscopy

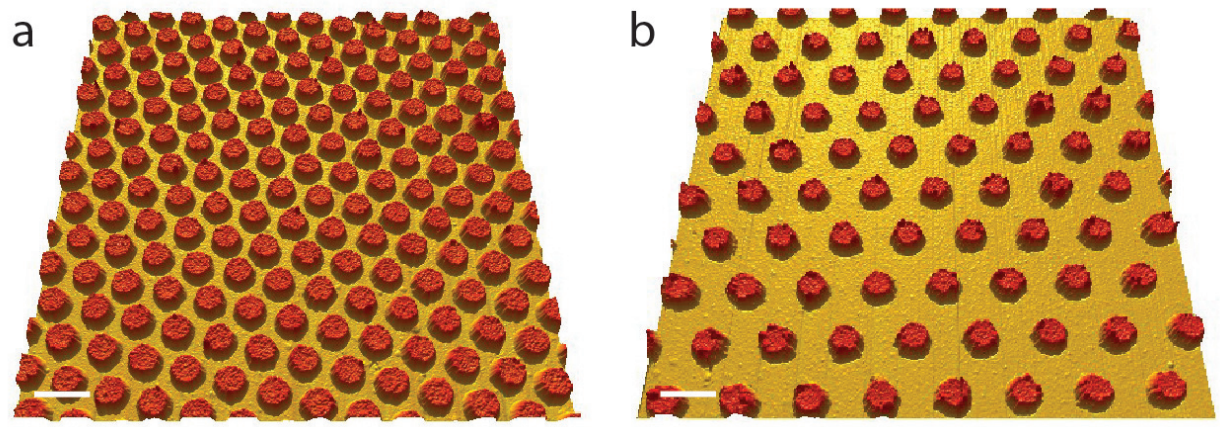

Figure 2.3: **AFM Topography of Arrays of Nb Islands on Au**. Atomic force microscopy (AFM) images of arrays of 87-nm thick Nb islands (red) on 10-nm thick Au underlayer (yellow). The arrays have edge-to-edge spacings of (**a**) 140 nm and (**b**) 340 nm. The white scale bar is 500 nm.

(SEM) image of an array of islands overlapping an Au four point pattern, labelled with our measurement scheme.

The BCS coherence length in Nb is $\xi_0 = 38$ nm, so our islands are roughly seven times the Cooper pair size[63]. The Ginzburg-Landau (GL) coherence length is a measure of the characteristic length within which the order parameter varies. The proper method of accurately measuring the GL coherence length in Nb is to extract it from the temperature dependence of the critical field. Ginzburg-Landau theory finds that $H_{c2}(T) = \frac{\Phi_0}{2\pi\xi_s^2}(1 - T/T_c)$, where Φ_0 is a flux quantum; ξ_s could be extracted from a linear fit to H_{c2} versus T. Unfortunately, we have not yet performed this series of measurements on an unpatterned Nb film. We can, however, roughly estimate the GL coherence length from the mean free path ℓ, using $\xi_s = 0.852(\xi_0\ell)^{1/2}(1 - T/T_c)^{-1/2}$, for a mean free path $\ell \approx 8$ nm. The GL coherence length diverges at the transition, and is roughly 27 – 140 nm within 2 K of the transition in our Nb. We estimate ℓ from the Einstein relation $\rho^{-1} = e^2 n_s(\epsilon_F)D$, where $D = \frac{1}{2}v_F\ell$ is the diffusion constant; $v_F = 1.37 \times 10^6$ m/s, $\epsilon_F = 5.32$ eV, and $n_s(\epsilon_F) = 5.56 \times 10^{28}$ m^{-3} are the are the Fermi velocity, Fermi energy, and density of states at the Fermi level[64], respectively, in Nb. The normal state resistivity $\rho(10\text{ K}) \approx 1.12 \times 10^{-5}$ Ω·cm was measured near the transition of a 87-nm thick, unpatterned Nb film. Given that our islands are only moderately larger than their coherence lengths, significantly larger than the mean free path, and much smaller than the inelastic scattering length[65] (~ 10 μm), they can be considered *mesoscopic*.

X-ray diffraction (XRD) spectra of both 87 nm and 145 nm thick Nb films, and scanning electron microscopy of Nb islands showed that the Nb is polycrystalline, with growth along the (110) direction and grain height equivalent to the film thickness. The XRD results are show in Figure 2.5. SEM images, shown

Sample	z_{Au} [nm]	z_{Nb} [nm]	d [nm]	Array Size [μm $\times$ μm]	No. of Islands [$\times 10^3$]	D [cm^2/s]	$\xi_{\rm N}$ [$\times T^{-1/2}$ nm]
1	10	87	90, 140, 190, 240, 290, 340	120 $\times$ 30	33.9, 25.8, 20.5, 16.6, 13.7, 11.4	94.2	268
2	10	145	90, 140, 190, 240, 290, 340	120 $\times$ 30	33.9, 25.8, 20.5, 16.6, 13.7, 11.4	94.2	268
3	10	47	440, 540, 640	120 $\times$ 30	8.4, 6.5, 5.1	95.3	270
4	10	125	490, 540, 590, 640, 690	500 $\times$ 150	153.8, 135, 119.4, 106.6, 95.7	96.6	272
5	10	145	740, 840, 940, 1040, 1140, 1240	500 $\times$ 150	86.5, 71.3, 59.9, 51.1, 43.9, 38.3	67.7	227
6	10	103	740, 840, 940, 1040, 1140	500 $\times$ 150	86.5, 71.3, 59.9, 51.1, 43.9	72.7	236

Table 2.1: **Properties of Notable Samples Reported in this Thesis**. All islands are 260 nm in diameter. Normal metal and superconductor layer thickness (height) are as represented by $z_{Au,Nb}$ and d is the edge-to-edge island spacing. So, the array lattice constant a is 260 nm greater than the specified d. The arrays sizes noted are the dimensions of the rectangular Au layer between the current leads. The corresponding "no. of islands" in the adjacent column is the number of islands on top of this layer, rounded to the nearest hundredth. (See the Appendix for the specific value). The Au four point pattern size is the same for all devices on a single sample such that the number of islands differs between devices. The diffusion constant in the Au, D, and corresponding Thouless length, $\xi_{\rm N}$, are in the last two columns.

in Figure 2.6, reveal an elongated, columnar grain structure. This columnar grain structure, as well as evidence of intergranular voids, has been previously observed in evaporated Nb films[66,67].

The Au film resistivity in devices in samples **1** and **2** (see Table 2.1) is ρ (10 K) $\approx (6.25 \pm 0.75) \times 10^{-6}$ $\Omega\cdot$ cm, which is extracted from unpatterned 10 nm thick films. Using the Einstein relation, we estimate a diffusion constant $D \approx 94.2$ cm^2 s^{-1} which yields a mean free path of $\ell \approx 13$ nm and a temperature-dependent coherence length $\xi_{\rm N}(T) = \left(\frac{\hbar D}{k_b T}\right)^{1/2} \approx \frac{268}{\sqrt{T}}$ nm. The results for other samples presented in Table 2.1 were similarly calculated.

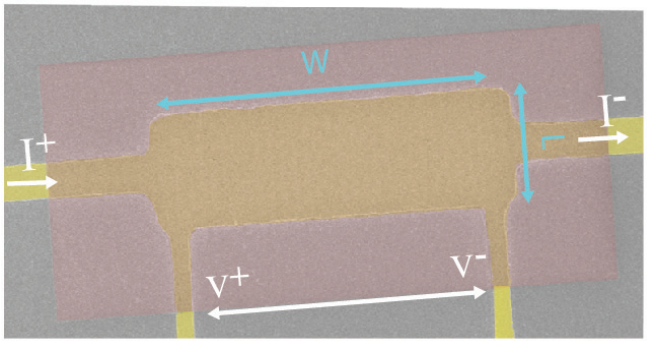

Figure 2.4: **SEM Image of Device**. False color scanning electron microscopy (SEM) image of array of islands (red rectangle) overlapping Au four-probe pattern (yellow), with the measurement schematic indicated with white arrows and lettering. Two different four point pattern sizes ($W \times L$) were used in this study: 120 μm $\times$ 30 μm and 500 μm $\times$ 150 μm.

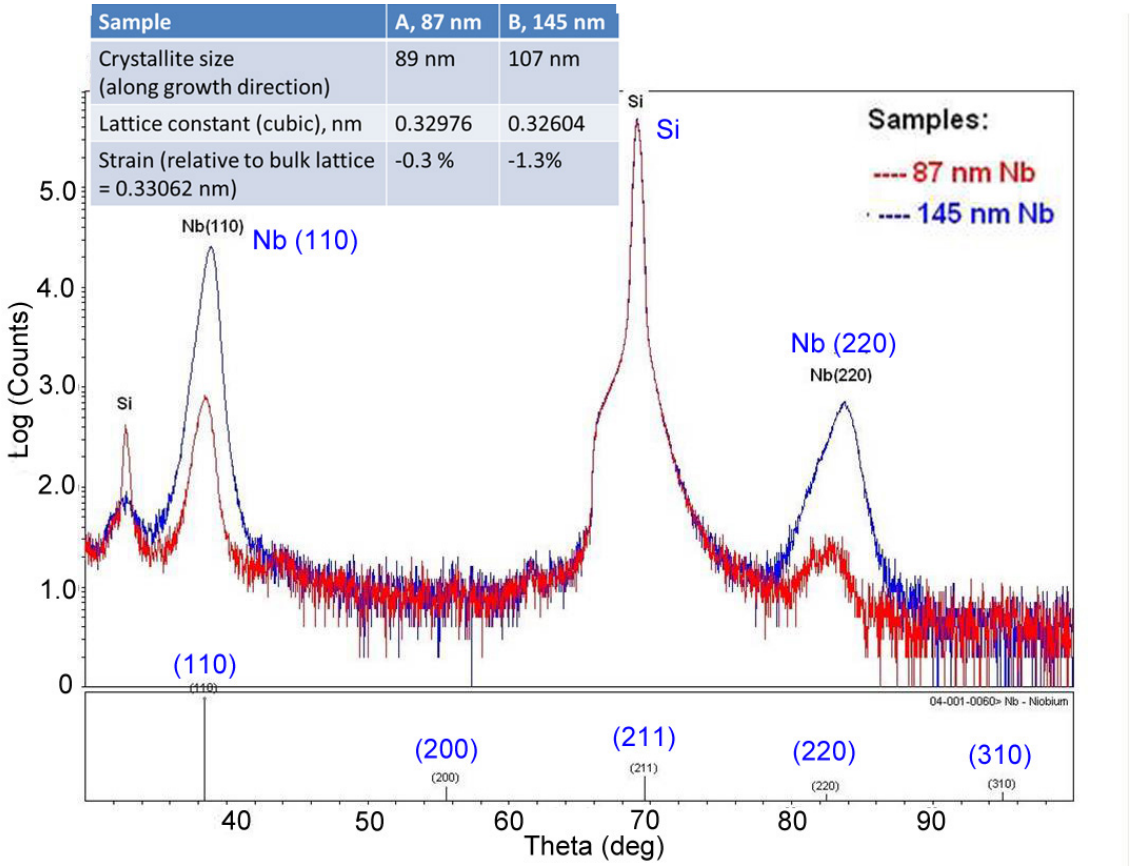

Figure 2.5: **X-Ray Diffraction of Nb-Au Bilayer Films**. X-ray Diffraction (XRD) micrograph of two Nb-Au films. In both films, the Au thickness is 10 nm. The sample with 87-nm thick Nb is represented by the red curve and the one with 145-nm thick Nb is represented by the blue curve. Blue labels were added on to the original micrograph for clarity. The large peak labelled "Si" represents the Si detected from the SiO_x substrate. Both films show (110) orientation of Nb grains and a lattice constant similar to that of bulk Nb. The grain height is similar to the film thickness; it is 89 nm in the 87-nm thick film and 107 nm in the 145-nm thick film. Scan taken by Dr. Mauro Sardela.

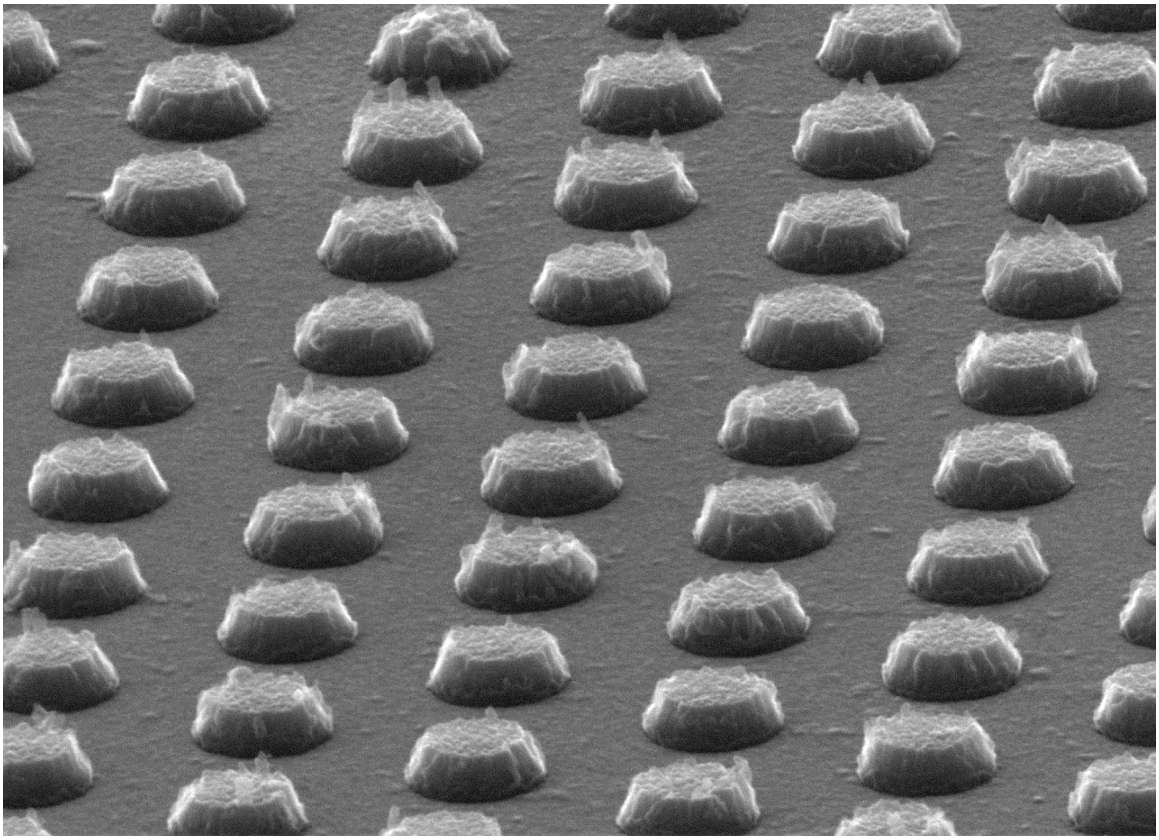

Figure 2.6: **Side-view SEM Image of Array of Nb Islands on Au**. Scanning electron micrograph of Nb islands showing columnar grain structure. Image taken by Dr. Jim Mabon.

2.3 Measurement Set-up

Transport measurements were performed in three different cryostats, each with different accessible temperature ranges: a pumped ^{4}He cryostat, a ^{3}He refrigerator, and a ^{3}He/^{4}He dilution refrigerator. A Janis SVT-400 pumped ^{4}He system was used for measurements requiring temperatures above 1.6 K. By pumping on a bath of He(ℓ), the boiling point of ^{4}He is reduced until the vapor pressure becomes too small to further reduce. For lower temperatures, ^{3}He is necessary, as it maintains a higher vapor pressure at lower temperatures than ^{4}He. ^{3}He is used in both the ^{3}He and dilution cryostats in which ^{3}He or, in the latter case, a mixture of ^{3}He/^{4}He gas is brought into contact with a pumped ^{4}He reservoir (1K pot). We used an Oxford Heliox ^{3}He cryostat for measurements in the 245 mK to 2 K temperature range, and to apply magnetic fields up to 8 T. Temperatures down to 15 mK were achievable using a Kelvinox MX-400 dilution refrigerator equipped with a 10 T magnet, which uses an external gas handling system to circulate a stoichiometric mixture of ^{3}He/^{4}He. Below the triple point of ^{3}He/^{4}He, the mixture separates into two liquid phases: a ^{4}He-rich phase and a ^{3}He-rich phase. By pumping on the ^{4}He-rich phase, a disproportional amount of the lighter ^{3}He is removed, causing ^{3}He from the ^{3}He-rich phase to cross the phase boundary in order to restore equilibrium. The energy to cross this phase boundary is provided by heat from the walls of the mixing chamber on which our sample is mounted and well thermally coupled.

All measurement systems are equipped with electrical boxes containing capacitor input filters (also known as pi filters) and low temperature resistors that act as noise filters. The dilution cryostat is situated in a shielded room; the current and voltage sources, helium level meter, magnet power supply, and computer station were all set-up outside the room to minimize external noise that could be coupled into the device under testing. All data was collected using LABVIEW programs, and analyzed in OriginPro. Short Labtalk programs were written to efficiently perform the same analysis on multiple data sets. Figure 2.7 is a schematic of our experimental set-up.

Superconducting devices are highly sensitive to small magnetic fields. Our set-up was carefully designed to exclude magnetic components. Both the chip carrier and the socket in which it is mounted are made exclusively of non-magnetic components. This prevents distortions in the field experienced by the sample, and the unintentional generation of residual fields when the fridge magnet has been turned off.

Resistance measurements were performed using a Stanford SRS 830 lock-in amplifier, by converting an AC $f = 17.177$ Hz, 100 mV – 5 V output into a 10 nA – 500 nA signal using 1 – 10 MΩ resistors. In consideration of the cryostat cooling power and minimizing the effects of Joule heating on the sample, the typical excitation current was reduced with reduced temperature. For example, measurements taken in the pumped ^{4}He cryostat and dilution cryostat typically involved excitation currents of 500 nA and 10 nA,

respectively. A voltage pre-amplifier multiplied the measured voltage by 10,000 and used a low pass filter to attenuate signals higher than 100 Hz. Use of the pre-amplifier significantly reduced the noise coupled into the low resistance measurements. All plots show the results of sweeping the temperature up from the system base temperatures. In the pumped ^{4}He cryostat, the temperature was swept at 0.5 K/min; no hysteresis was observed in the up and down sweeps at this rate. In the dilution cryostat, the temperature sweep typically took approximately 1 hour.

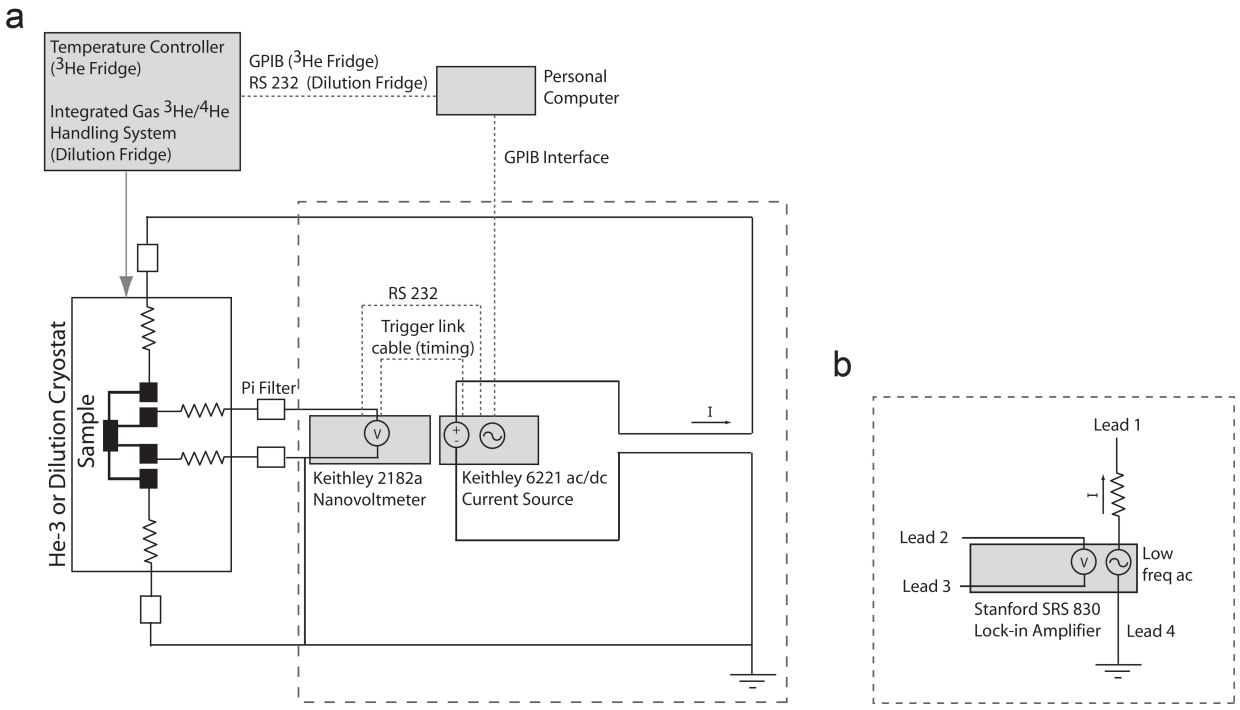

Figure 2.7: **Transport Measurement Set-up**. A schematic of the general set-up for (**a**) pulsed-IV and differential resistance characteristics, and (**b**) low-noise resistance measurements.

2.3.1 Magnetic Field Offset: Cancelling Trapped Flux

The magnets in both the dilution and ^{3}He cryostats are wound from superconducting Nb_3Sn wires. After using the magnets, a persistent current may be stored, that is, flux may be trapped. Trapped flux presents a challenge not only once the magnet is ramped back down to zero, but even after the system has been warmed and re-cooled. Typically, the trapped flux in our magnets is approximately 0.1 – 6.6 mT. Hence, measurements intended to be taken in zero-field (magnet off), might actually be taken in a field. In SNS arrays and superconducting devices with low critical fields, trapped flux will significantly alter results. Specifically in our arrays, IV characteristics indicative of BKT transitions are obscured; low current ohmic

tails appear from de-pinned, field-induced vortices.

To prevent these problems, we took careful precautions. Prior to measurements, magnet degaussing procedures were followed to first minimize the amount of trapped flux. Afterwards, characteristics of the sample (e.g. the symmetry of magnetoresistance oscillation around $B = 0$, linear $\log I$ - $\log V$ curves in zero field) were used to find an appropriate offset field to cancel out the trapped flux. All zero-field measurements reported here were taken in an appropriate offset field, therefore, in true zero-field.

Chapter 3

Two-Step Transition to Superconductivity

In this chapter, we will present the temperature-dependent resistance behavoir in arrays with island spacings ranging from $d = 90$ nm to $d = 1.14$ μm. We will show that, as the temperature is reduced, the arrays undergo two-step transitions to the superconducting state. Additionally, we will qualitatively discuss and compare the shape of two-step transitions in multiple arrays. In Chapter 4 and 5, we characterize the superconducting transitions in these systems as a function of island thickness and spacing.

3.1 Two-Step Transitions in Arrays with Island Spacings $d = 90 - 340$ nm

Figure 3.1 shows the temperature-dependent resistance for two devices: the first (Figure 3.1a) has $z = 87$ nm ($\pm$ 2 nm) thick Nb islands, and the second (Figure 3.1b) has 145 nm ($\pm$ 2 nm) thick ones. The normal state resistances in the arrays is $R_N \approx 15$–25 Ω; the y-axis shows the resistance normalized to its 10 K value. The resistance drops to zero in two steps as the temperature is lowered. The higher-temperature drop, T_1, is associated with the superconducting transition of the individual islands. The lower-temperature drop, at temperature T_2, is associated with superconducting phase-locking across the array. Both T_1 and T_2 decrease with increasing island spacing. In both samples, the device with the closest spaced islands $d = 90$ nm exhibit a single transition. This is not surprising given that the normal metal coherence length at T_1, $\xi_n(T_1) \approx 100$ nm, is on the order of the edge-to-edge spacing. Also, the temperatures T_1 and T_2 are higher in the sample with thicker islands. As the island spacing increases, the first drop in resistance becomes less steep. The transition in the 240-nm spaced islands, the green curve in Figure 3.1a, shows an anomalous shape, that was

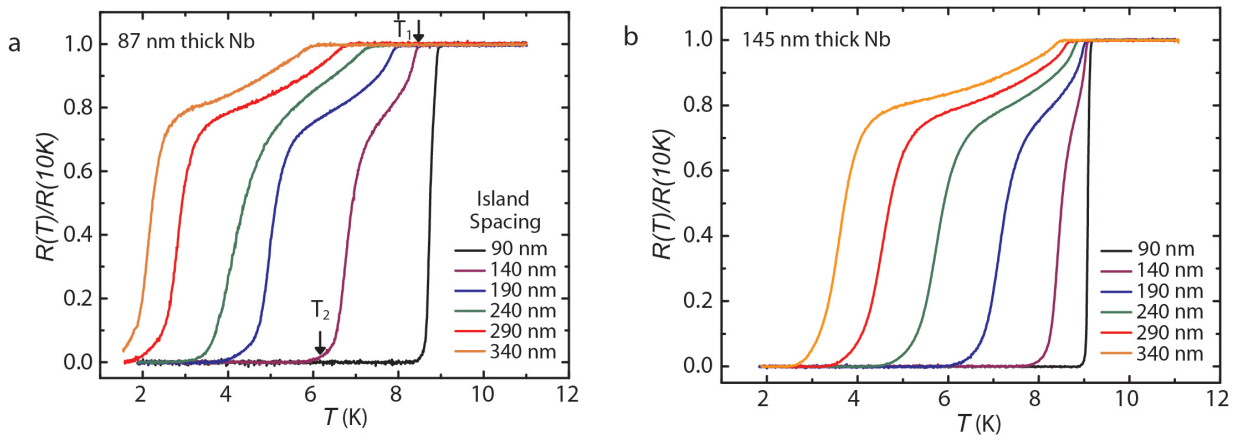

Figure 3.1: **Superconductivity in Nb Arrays with Island Spacings d = 90 – 340 nm**. (**a, b**) Temperature-dependent resistive transitions in arrays with different edge-to-edge island spacings d. The island diameter is 260 nm for all arrays. The islands are (**a**) 87 nm thick and (**b**) 145 nm thick. Arrows in (**a**) mark T_1 and T_2 for the islands spaced 140-nm apart. The data are normalized to the resistance at 10 K. Note that T_1 and T_2 occur at higher temperatures for thicker islands. In Panel (**a**), the lowest temperature curves are cut off by the minimum attainable temperature of our apparatus. For more parameters relevant to each sample, see Samples (**a**) **1** and (**b**) **2** in Table 2.1

.

precisely reproducible[1].

[1]We verified that this was not due to a problem with the measurement system by rotating the sample and re-taking all of the data using different transports leads. We also observed similar smearing in the 240-nm spaced islands in other samples.

3.2 Dependence of Transitions on Island Height in Arrays with Island Spacings $d = 90 - 340$ nm

To continue investigating the dependence of the transitions on island height, we measured multiple samples containing arrays with $d = 90$ – 340 nm. The island height was fixed in all arrays on a single sample, but varied between samples. Results from five of these samples, with island heights $z = 32$ – 126 nm, are show in Figure 3.2.

The shortest islands studied were $z = 32$ nm in height, on the order of the coherence length $\xi_{\mathrm{Nb}}(T \approx 7\mathrm{K}) \approx 27$ nm. Results are shown in Figure 3.2a and we will focus on this array in this paragraph. The transition temperatures T_1 were significantly suppressed, far more-so than T_2. In the two arrays with the closest island spacings $d = 90$ nm and $d = 140$ nm, T_1 and T_2 are close enough that the transition exhibits a single step. However, for array with $d = 140$ nm, the bottom of the transition (near T_2) is slightly broadened, as would be expected in a BKT transition. The array with $d = 190$ nm exhibits two steps, though not very distinct, and a significantly broadened leg near T_2.

Now let's look at the two arrays with the farthest spaced islands, $d = 290$ nm and $d = 340$ nm. We see two very discernible steps in the transition. However, the array with intermediate spacing, $d = 240$ nm, is unusual. Its shape appears to be a crossover between the single-step and distinct two-step behavior. Strangely enough, this is the same spacing as the aberrantly shaped transition in the sample reported in the previous section with island heights of $z = 87$ nm, seen in Figure 3.1a (green curve).

The transitions in the four other samples, all having taller islands (Figure 3.2bcde), are more similar in shape to the results shown in Figure 3.1. Only two of these samples had working arrays with $d = 90$ nm — the one with island heights $z = 49$ nm, shown in Figure 3.2b, and the one with $z = 94$ nm, in Figure 3.2d. Both 90-nm spaced arrays demonstrate only a single transition.

The results for the samples with island heights $z = 49$ nm and $z = 51$ nm, shown in Figures 3.2b and 3.2c, are almost identical. Given the nominal 2 nm difference in island height between these two samples, within the measurement error of the atomic force micrographs, this attests to the reproducibility of our measurements.

The sample shown in Figure 3.2d has island height $z = 94$ nm. We now compare this sample to the one shown in Figure 3.1a, with fairly similar island height $z = 87$ nm. The spread in T_1 with an increase in island spacing appears very similar. However, surprisingly, T_2 is more suppressed in the sample with slightly taller islands [2].

[2] Note that we tested multiple samples with island heights $z \approx 87$ nm, and the results were identical to that shown in Figure 3.1a. The measurement is highly reproducible.

Lastly, we focus on the sample with the $z = 126$ nm tall islands, shown in Figure 3.2e. In comparison to the $z = 145$ nm islands (Figure 3.1b), T_1 is similar, but slightly suppressed. However, T_2 is significantly more suppressed than might be expected. In fact, for this sample with $z = 126$ nm, the arrays with $d = 140$ nm, 190 nm, and 240 nm all have *lower* transitions T_2 than the arrays with the same spacing, but *shorter* islands $z = 51$ nm and 49 nm.

Now that we have compared all of the samples in Figure 3.2, let us return to the sample with the shortest islands in this set ($z = 32$ nm), as it is the most anomalous. Though the transitions T_1 are suppressed the most in this sample, the transitions T_2 occur at are surprisingly high temperatures. In fact, T_2 for the array with $d = 140$ nm occurs around 6 K in this sample, and 5 K for the sample with taller islands $z = 94$ nm. Additionally, the array with $d = 290$ nm has a $T_2 \approx 3$ K in the 32-nm tall islands, yet $T_2 < 1.6$ K for all other 290-nm spaced arrays with taller islands.

For a single sample (*i.e.*, a set of arrays with fixed island heights) the overall trend between the transitions temperatures and spacing progresses as expected. However, we do not understand the changes in the transition temperatures with island height. It may be due to a change in the morphology of the islands or a charging energy due to an imperfect interface. In Chapter 4, we will plot T_1 versus d for all of these devices on a single plot and further discuss the height dependence.

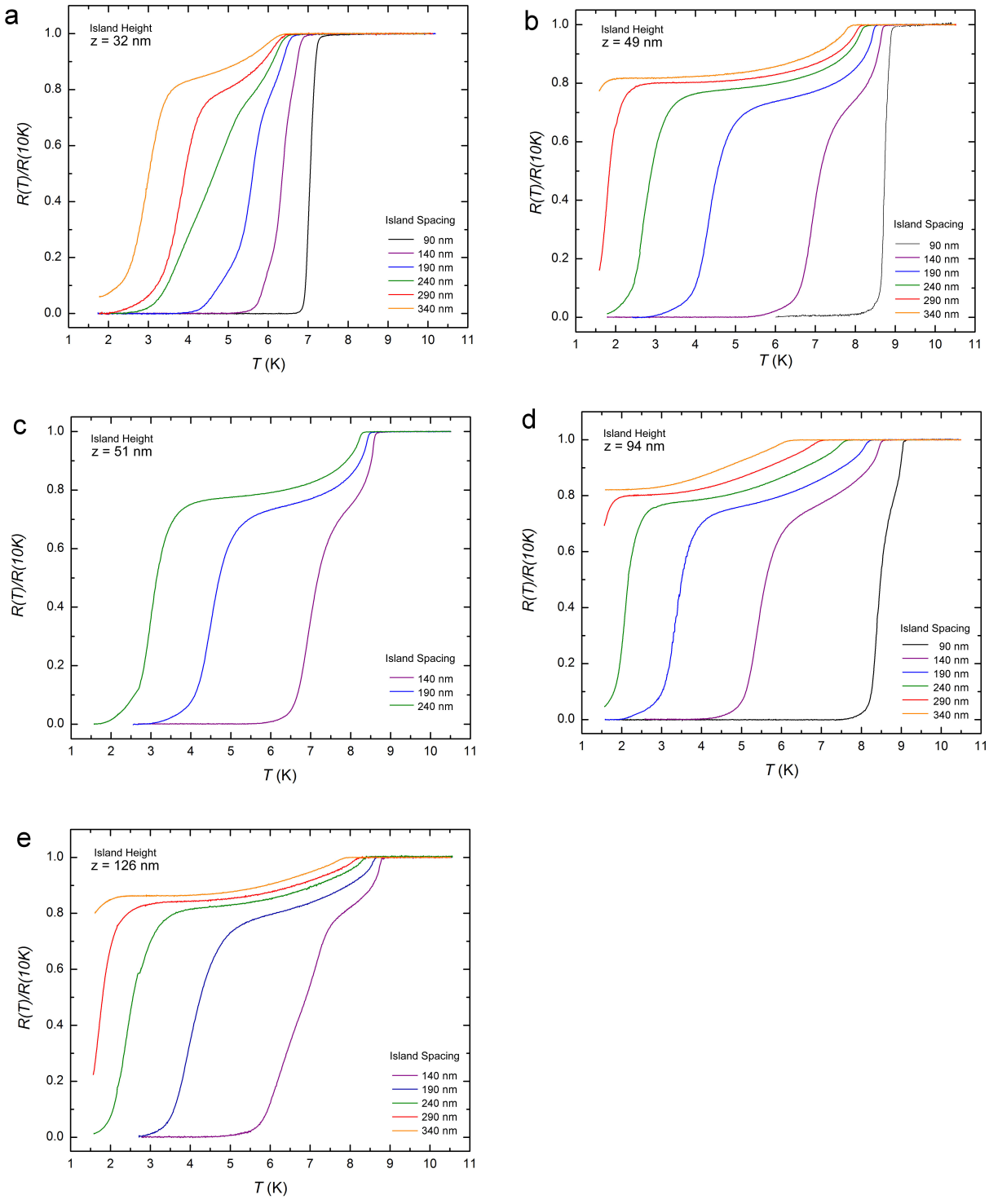

Figure 3.2: **Superconducting Transitions in Nb Island Arrays: A Comparison of Arrays with Different Island Heights**. The plots show the temperature-dependent resistances in arrays with d = 90 nm – 340 nm and island heights (**a**) z = 32 nm, (**b**) z = 49 nm, (**c**) z = 51 nm, (**d**) z = 94 nm, and (**e**) z = 126 nm.

3.3 Two-step Transitions in Arrays with Island Spacings $d = 490 - 640$ nm

In the previous two sections, we reported on arrays with island spacings $d = 90 - 340$ nm. In this section, we show results for arrays with farther island spacings, specifically $d = 490 - 640$ nm. The results for these arrays are displayed in Figure 3.3. The critical temperatures T_1 and T_2 occur within the accessible temperature ranges of two different measurement systems. Given this, the high temperature region, displayed in Figure 3.3b, was measured in the pumped ^{4}He cryostat, and the lower temperature region (Figure 3.3c), in the dilution cryostat. For direct comparison to the results in Figure 3.1, Figure 3.3a is a merged plot of the two regions; the arrow marks the transition between measurement systems. A continued suppression in both T_1 and T_2 with an increase in d is evident and the drop at T_1 continues to broaden. Below T_1, all curves dip down, exhibiting a local minimum, slightly rise, then flatten before the dropping to T_2 with a continued decrease in temperature. The local minima is most evident in Figure 3.3b and identified for $d = 490$ nm by a pink arrow. The reason for these local minima is not understood.

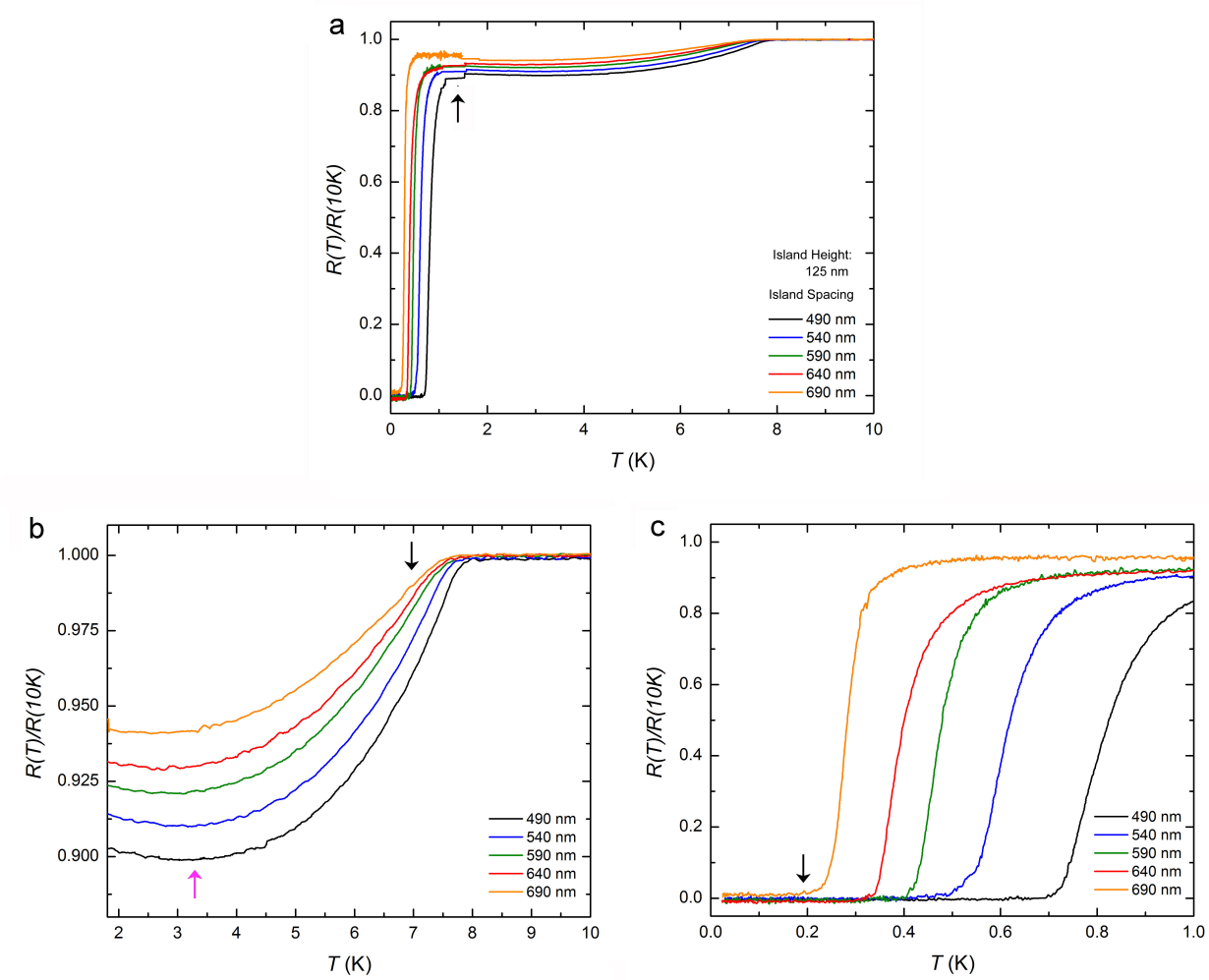

Figure 3.3: **Superconductivity in Nb Arrays with Island Spacings d = 490 - 690 nm**. Temperature-dependent resistive transitions in arrays with five different edge-to-edge island spacings d. The island diameter is 260 nm for all arrays. The islands are 125-nm thick. Two different measurement apparatuses were necessary to capture both transitions. (**a**) A merged plot of the results from both systems, showing the full transition from the completely normal state to superconductivity across the arrays. The black arrow indicates transition between measurement systems, where the data was merged. (**b**) The high-temperature resistive transitions were measured in a pumped ^{4}He cryostat down to $T = 1.8$ K, capturing transitions T_1. The black arrow shows T_1 in the 690-nm spaced islands, and the pink arrow points out an anomalous local minimum. (**c**) The low-temperature transitions measured in the dilution cryostat down to $T = 15$ mK, capturing the transitions to the zero-resistance superconducting state T_2. The black arrow shows T_2 in the 690-nm spaced islands. For more parameters relevant to this sample, see "Sample **4**" in Table 2.1.

3.3.1 Phenomenological Model of Array of Mesoscopic Granular Superconducting Islands on Normal Metal Film

As can be seen from Figures 3.1 and 3.2, T_1 has a pronounced dependence on island spacing. From the Ginzburg-Landau perspective, T_1 for an isolated island of lateral dimensions comparable to ξ_s should equal the transition temperature for a continuous film of the same height, as observed in the study by Resnick *et al.* of Pb islands with a Sn overlayer[19]. Furthermore, the Thouless length at temperatures near T_1 is shorter than the edge-to-edge spacing, so there should be negligible coupling between the islands at these temperatures. These two presumptions led us to expect no spacing dependence in T_1, as was also observed in Resnick's study. These expectations are inconsistent with the pronounced spacing-dependence of T_1 seen in the data in the previous section; the trend cannot be explained by conventional theories. We were thus prompted to consider the importance of the granularity in the islands and develop the model of transitions in arrays of granular islands described in this section [(3)].

Instead of considering each island as having a single, fluctuating superconducting phase, it was necessary to consider the phase fluctuations of the individual grains. To this end, we developed a phenomenological model to describe arrays of granular superconducting islands on a normal metal film[68]. Figure 3.4 is an illustration of our model. Similar to LAT, our phenomenological model predicts that the arrays undergo a two-step drop in resistance to a zero-resistance superconducting state with a decrease in temperature. The lower-temperature drop, at temperature T_2, is associated with superconducting phase-locking across the array. The higher-temperature drop, T_1, is associated with the superconducting transition of each island. We characterize these transitions as caused by stabilization of superconductivity on each island via a weak coupling to and feedback from its neighbors. The system has two characteristic energy scales: (a) J, the coupling between grains on an individual island, and (b) $J'(< J)$, the coupling between grains on neighboring islands. The temperature scale in Figure 3.4 is divided into regions separating different regimes. An explanation of the inter- and intra-island coupling in each region is described below:

- **Region I**

  For $T > T_1$, the separate grains on each island have incoherent superconducting phases. At T_1, intra-island phase coherence develops, and the system's resistance decreases as Cooper pairs from the superconducting grains diffuse into the underlying Au. For very large islands, T_1 would depend only on J, which grows with island height, but is spacing-independent. For mesoscopic islands, however, the T_1 of an isolated island is depressed by phase fluctuations among the grains. These fluctuations are reduced by the inter-island coupling J', leading to stabilization of superconductivity in the islands.

[3] Sarang Gopalakrishnan developed the theory behind this phenomenological model.

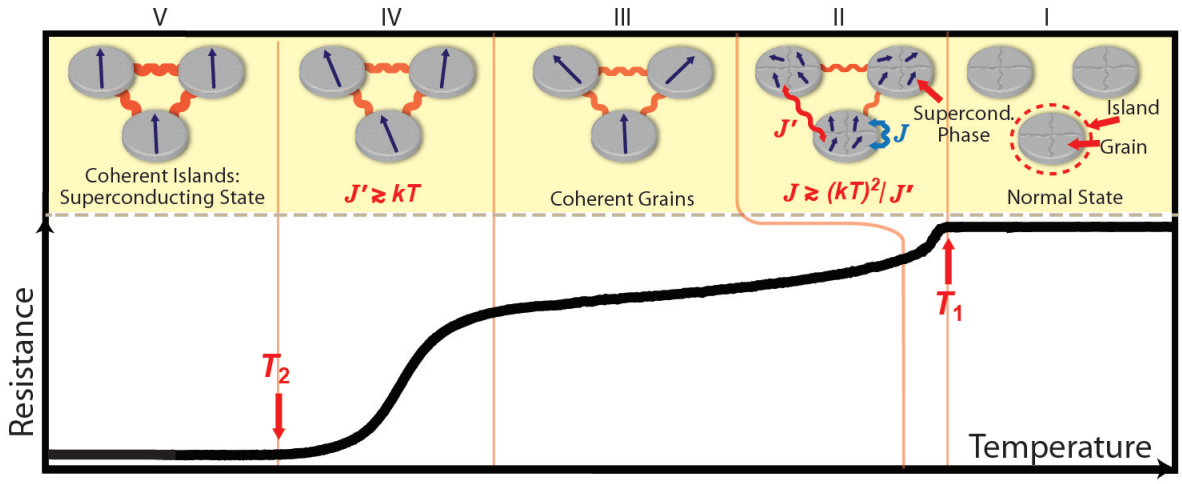

Figure 3.4: **Phenomenological Model of Superconductivity in Arrays of Mesoscopic Granular Superconducting Islands on a Normal Metal**. The gray circles represent islands made up of a superconducting material divided into grains. Nearest neighbor grains experience a Josephson coupling J, and each grain is coupled to grains in other islands with strength J'. Black arrows represent the fluctuating phase of the superconducting order parameter in the grains and the islands. In region I, the islands are normal metals. In region II, the phases of the grains start to become coherent and the resistance drops at T_1 due to diffusion of Cooper pairs from the grains into the underlying normal metal. In region III, J' increases as the normal metal coherence length $\xi_N(T)$ increases. In region IV, the phases of the islands start to lock when ξ_N becomes on the order of the island spacing. Lastly, in region V, the system has long-range phase coherence and is superconducting below T_2.

Thus, we would expect T_1 to decrease for larger spacings (i.e., as J' decreases).

- **Region II**

  Below T_1, the intra-island phase coherence strengthens continuously as we further decrease the temperature. This leads to a gradual, rather than steep, drop at T_1.

- **Region III**

  Region III shows the familiar proximity effect behavior. Here, the normal-metal coherence length ξ_N increases as the temperature decreases. J has saturated and J' continues to increase.

- **Region IV**

  When ξ_N becomes comparable to the edge-to-edge island spacing, inter-island phase coherence begins to emerge. At T_2 the system undergoes a Berezinskii-Kosterlitz-Thouless transition to a fully superconducting state. Because J' is weaker for farther spaced islands, T_2 is also suppressed with increasing island spacing.

Modelling each island as a one-dimensional chain of XY spins, this theory can predict the trends in T_1 and T_2 with island spacing. The following Hamiltonian considers the intra-island coupling energy (first term)

and the inter-island coupling energy (second term) within the framework of this model:

$$H = -J\sum_{p}\sum_{\langle ij\rangle\in p}\cos(\phi_i-\phi_j) - J'\sum_{\langle pp'\rangle}\left(\sum_{i\in p}\cos(\phi_i)\right)\left(\sum_{j\in p'}\cos(\phi_j)\right) \tag{3.1}$$

The superconducting phase of a grain i is ϕ_i, p indexes islands, $\langle ij\rangle \in p$ denotes nearest-neighbor grains on island p, and $\langle pp\rangle$ denotes nearest-neighbor islands. The model assumes that each grain on an island couples with equal strength to every grain on neighboring islands. The inter-island coupling $J' \approx J'_0 e^{-d/\xi_N(T)}$, where d is the edge-to-edge spacing of the islands and J'_0 is the coupling amplitude. Similarly, the intra-island coupling follows the standard proximity effect form, $J \approx J_0 e^{-\alpha/\xi_N}$, where α is a constant that depends on individual island parameters. The criteria for superconductivity in the individual islands (Eq. 3.2) and across the array (Eq. 3.3) is

$$\frac{k_B T_1}{\sqrt{zJJ'}}\coth(m\sqrt{\frac{zJ'}{J}}) = 1 \tag{3.2}$$

$$zm^2 J'(T_2) \approx k_B T_2, \tag{3.3}$$

where m is the number of grains per island and z the coordination number. For our triangular arrays, $z = 6$; each island has six nearest neighbors.

Using Eqs. 3.2 and 3.3, the prediction for the dependence of T_1 on island spacing is:

$$d + \alpha = -\ln\left[\frac{J_0 J'_0}{\xi_N^2(T_1)}\right]\xi_N(T_1). \tag{3.4}$$

In the next two chapters, we separately discuss the spacing dependence of transition temperatures T_1 and T_2. In Chapter 4, we will fit T_1 versus d to Eq. 3.4 from our phenomenological model.

Chapter 4

First Transition: Superconductivity in the Islands

In Chapter 3, we presented resistance versus temperature curves for arrays with island spacings $d = 90$ – 690 nm. We also presented a qualitative comparison of the trends in these arrays. In this chapter, we will focus on the transition T_1 and present a more quantitative analysis.

4.1 T_1 in Arrays with Island Spacings $d = 90 - 340$ nm

Figure 4.1a shows a plot of T_1 versus island spacing for the two samples presented in Section 3 in Figure 3.1 on page 37. The data for the device with the 90-nm spaced islands has been excluded. It is in a different regime, as it shows only a single transition. The dotted curves are fits to Eq. 3.4 from our phenomenological model of proximity coupled granular islands described in Section 3.3.1, and the solid lines are linear fits. The model fits the data reasonably well, though the T_1 is clearly *linearly* suppressed with island spacing. Capturing the trends of the data, the model predicts that (a) T_1 is suppressed with an increase in island spacing, (b) T_1 does not saturate as $d \to \infty$, and (c) T_1 extrapolates to a finite value at $T = 0$.

Figure 4.1b shows the results for more samples, including the ones shown in Figure 4.1a for comparison. For Figure 4.1b, T_1 was extracted from the resistance versus temperature curves in Figure 3.2 on page 40. The only difference between the samples presented in Figure 4.1 is the Nb island height, specified in the legend. Though the rate at which T_1 changes with island spacing depends on the height of the islands, the trend is linear in all cases.

The dependence of T_1 on island height z is not fully understood. One explanation would be an effective

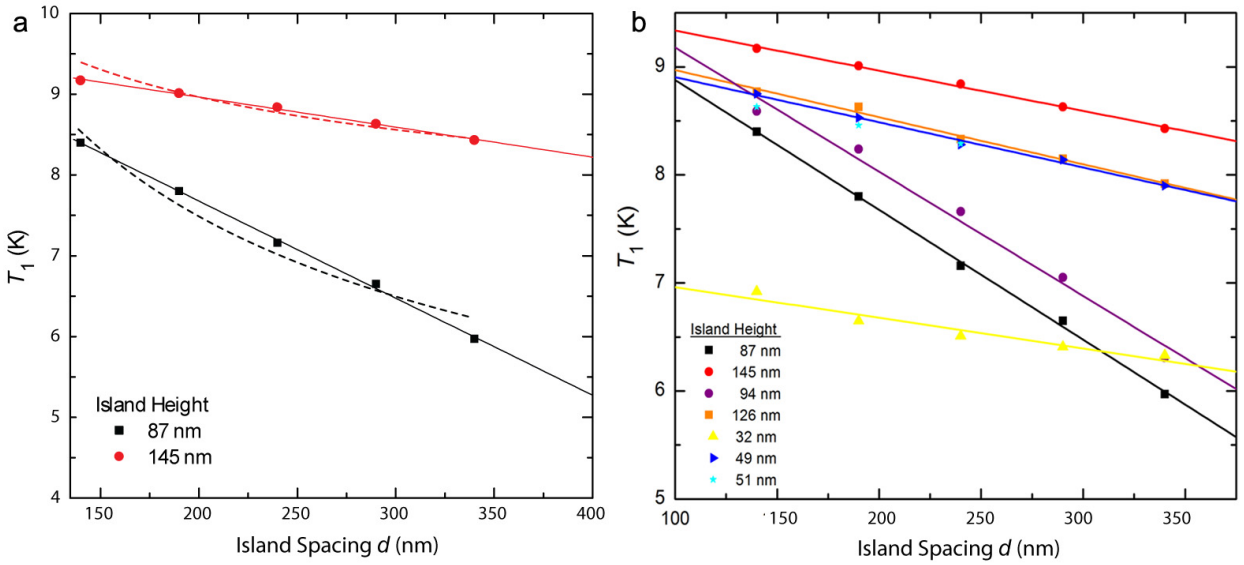

Figure 4.1: **Dependence of T_1 on Island Height and Spacing in Arrays with $d = 140 - 340$ nm.** The transition temperature T_1 is plotted versus island spacing for 87-nm thick islands (black squares) and 145-nm thick islands (red circles). Solid lines are linear fits, and dashed curves are fits to Eq. 3.4, that is, the a model of a coupled one dimensional chain of XY spins (Sec. 3.3.1). The points for the 90-nm island spacings are not shown, as the transitions for this spacing do not show two steps; for a similar reason, the 140-nm spacing for the thicker islands is shown, but not included in the fit. The data were extracted from the transitions show in Figure 3.1. (**b**) T_1 for samples with a range of Nb island heights $z = 32 - 145$ nm. The solid lines are fits to the data. The data were extracted from the transitions show in Figure 3.2.

charging energy that is larger in shorter islands and competes with superconductivity. If this were the case, there would be a systematic decrease in T_1 with island height. However, though the 145 nm tall islands do have the highest values of T_1, the samples with an island heights of 49 nm show higher T_1 values than the samples with island heights of 94 nm and 87 nm. We believe this result is reproducible; the two different samples with island heights of 51 nm and 49 nm show very similar transitions. Further, we tested multiple samples with island heights $z \approx 87$ nm, all producing identical resistance versus temperature curves. Even more surprisingly, the devices with $z = 126$ nm have nearly identical values of T_1 as the devices with $z = 49$ nm and $z = 51$ nm.

We postulate that changes in the grain structure with island height could be responsible for these unexplained trends. Nevertheless, x-ray diffraction micrographs of our evaporated superconducting films show that the grain height is approximately equal to the film thickness. So, it is unlikely that grain structure changes are fully responsible for the T_1 versus z relationship. In the thinnest islands, the significant suppression in T_1 could be simply due to the proximity effect. Nb-Au bilayer films of thickness similar to the thinnest islands tested would experience measurable suppression in T_c based on the DeGennes-Werthamer prediction. This expected suppression can be seen in our fit to bilayers shown in Figure 1.6.

4.2 T_1 in Arrays with Island Spacings $d = 490 - 690$ nm

Distinctly identifying T_1 becomes increasingly difficult for more dilute arrays, as seen in Figure 3.3(b) on page 42, due to a broadening of the transition. We consistently (and somewhat arbitrarily) define a criteria for choosing T_1 for these arrays. Defining T_1 as the temperature at which the resistance falls to $0.997\mathrm{R}_n$, we plot T_1 for arrays with island spacings $d = 490$ nm, 540 nm, 590 nm, 640 nm, and 690 nm in Figure 4.2. It is now clear that the linear trend remains robust as the concentration of superconducting islands decreases.

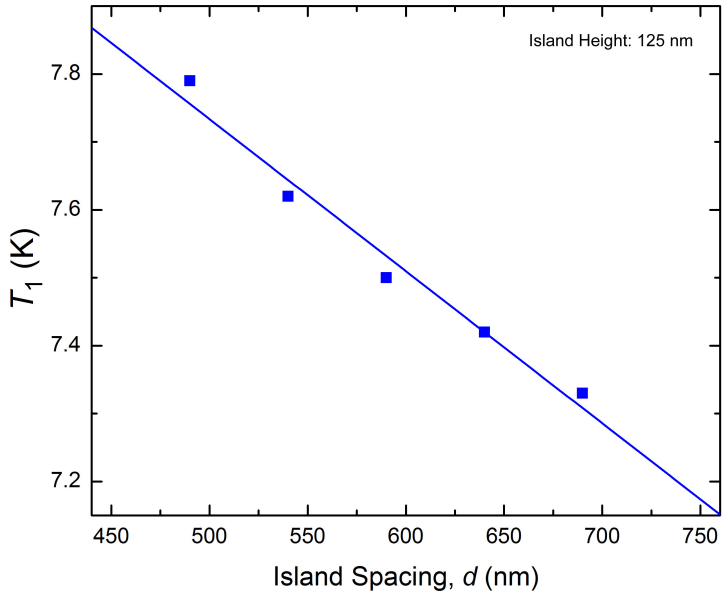

Figure 4.2: **Dependence of T_1 on Island Spacing in Arrays with $d = 490 - 690$ nm**. The transition temperature T_1 is plotted versus island spacing for 125-nm thick islands (blue squares). The solid line is a linear fit.

4.3 T_1 in Arrays with Island Spacings $d = 740 - 1140$ nm

We also studied arrays with island spacings $d = 740$ – 1140 nm. We did not show these results in Chapter 3 because these arrays are in a different regime; they do not become superconducting. We will show the resistance versus temperature behavior of these arrays in Chapter 5.6. However, they did exhibit distinct T_1 transitions. The T_1 versus d trend in these arrays was also markedly linear. The results for these arrays are shown in Figure 4.3.

The weakening of superconductivity in the islands with farther island spacing implies that superconduc-

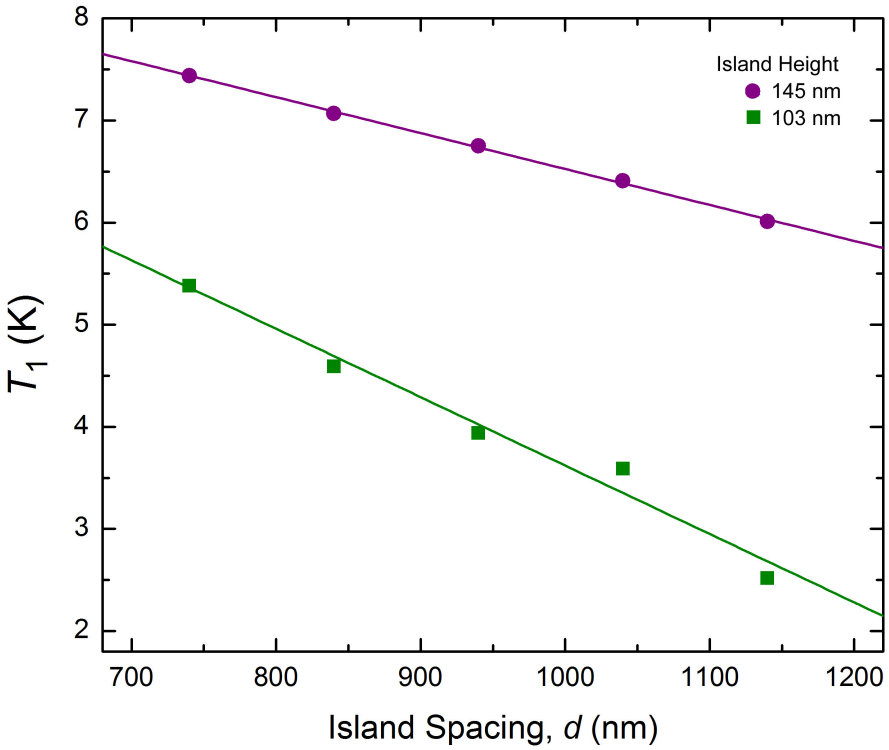

Figure 4.3: T_1 **in Dilute Arrays**. T_1 is plotted versus island spacing for a sample with 145-nm thick islands (purple circles) and 103-nm thick islands (green squares). We have excluded data for the farthest spaced islands, $d = 1240$ nm, as it may be in a different regime; the shape of the curve not understood. The solid lines are linear fits to the data. This linearity is consistent with the trends for the denser arrays reported in this section that, unlike these devices, become fully superconducting.

tivity on individual islands is fragile, and that a metallic state might be realizable for very weakly coupled islands. For samples **1** and **2**, T_1 extrapolates to zero at ~ 840 nm and ~ 2600 nm, respectively. The resulting $T = 0$ states would thus be metallic in that they would have finite resistance at finite island spacing. This is consistent with the Spivak model prediction of a superconductor-metal transition at a critical island concentration. Our simple extrapolation technique does avoid the issue of localization at low-temperatures; Spivak's model assumes the localization length will be larger than that of the array, thus localization effects can be ignored.

Our results could have implications for many 2D systems. Specifically, further investigation of our results at temperatures between T_1 and T_2 could help probe some of the mysteries within the complicated phase diagrams of high-temperature superconductors. Hole-doped high-temperature superconducting cuprates exhibit a so-called pseudogap at temperatures above T_c. In this regime, the systems are resistive, yet a gap appears. Unlike the standard superconducting energy gap in the electronic density of states, in the

pseudogap regime there is evidence of *few*, rather than *no*, states within this energy range. The origin of the pseudogap is highly controversial. Some researchers believe that it is either due to the formation of electronic stripes[69,70] or due to anit-ferromagnetic ordering[71–76]. Others believe that it is caused by the existence of superconducting correlations, such as the onset of Cooper pairing or vortex dynamics, above the critical temperature[77–84]. By nature of a distinct T_1 and T_2, we have superconductor fluctuations above the transition temperature T_2 in our arrays. So, we could directly test the latter theory by comparing tunnelling conductance measurements at temperatures between T_1 and T_2 to results in hole doped high-T_c cuprates [(1)]. To this end, we plan to perform scanning tunnelling microscopy measurements in our arrays.

4.4 Understanding Intra-island Coupling through IV Characteristics

In this section, we will analyze the temperature-dependent critical current of the individual Nb islands. Because the Josephson coupling between grains in a granular film is related to the supercurrent between the islands, understanding $I_c(T)$ versus T could help us better understand intra-island coupling in our arrays, therefore, the anomalous linear dependence of T_1 with increasing island spacing.

Figure 4.4 shows the differential resistance in response to an applied current for arrays from sample **1** with spacings (**a**) 90 nm, (**b**) 140 nm, (**c**) 190 nm, and (**d**) 240 nm, each at the temperatures specified in the figure caption. The measurements were taken in the pumped ^{4}He cryostat, which has high enough cooling power to properly dissipate heat from high currents. For all of our samples, we use one of three configurations to determine the differential resistance. In the first method, we add a small AC signal from a SRS 830 lock-in amplifier to a swept DC signal from a Keithley 2400 sourcemeter using a battery-powered sum box and measure the resulting change in voltage using the lock-in amplifier. Secondly, we can use the Keithley 6221 AC/DC current source and 2182a nanovoltmeter to directly measure the differential resistance. Lastly, we can differentiate the pulsed-IV curves taken by the Keithleys 6221/2182a. In many cases, all scenarios produced the same results. In such cases, we typically used method two, as it was the fastest. However, for arrays with high critical currents, or when $\frac{dV}{dI}$ was taken at extremely low temperatures (e.g. 20 mK in the dilution refrigerator), methods one and two would produce a slightly suppressed I_c and little-to-no variation with temperature at low temperatures. In these cases, it was evident that Joule heating was problematic; more often than not, we rely on differentiated pulsed-IV curves.

[1] Ultrathin titanium nitride films show a pseudogap state induced by superconducting fluctuations. This is thought to be caused by the two-dimensionality and proximity to the insulating state in the SIT picture.[85]. These results have been compared to those for high-T$_c$ superconductors.

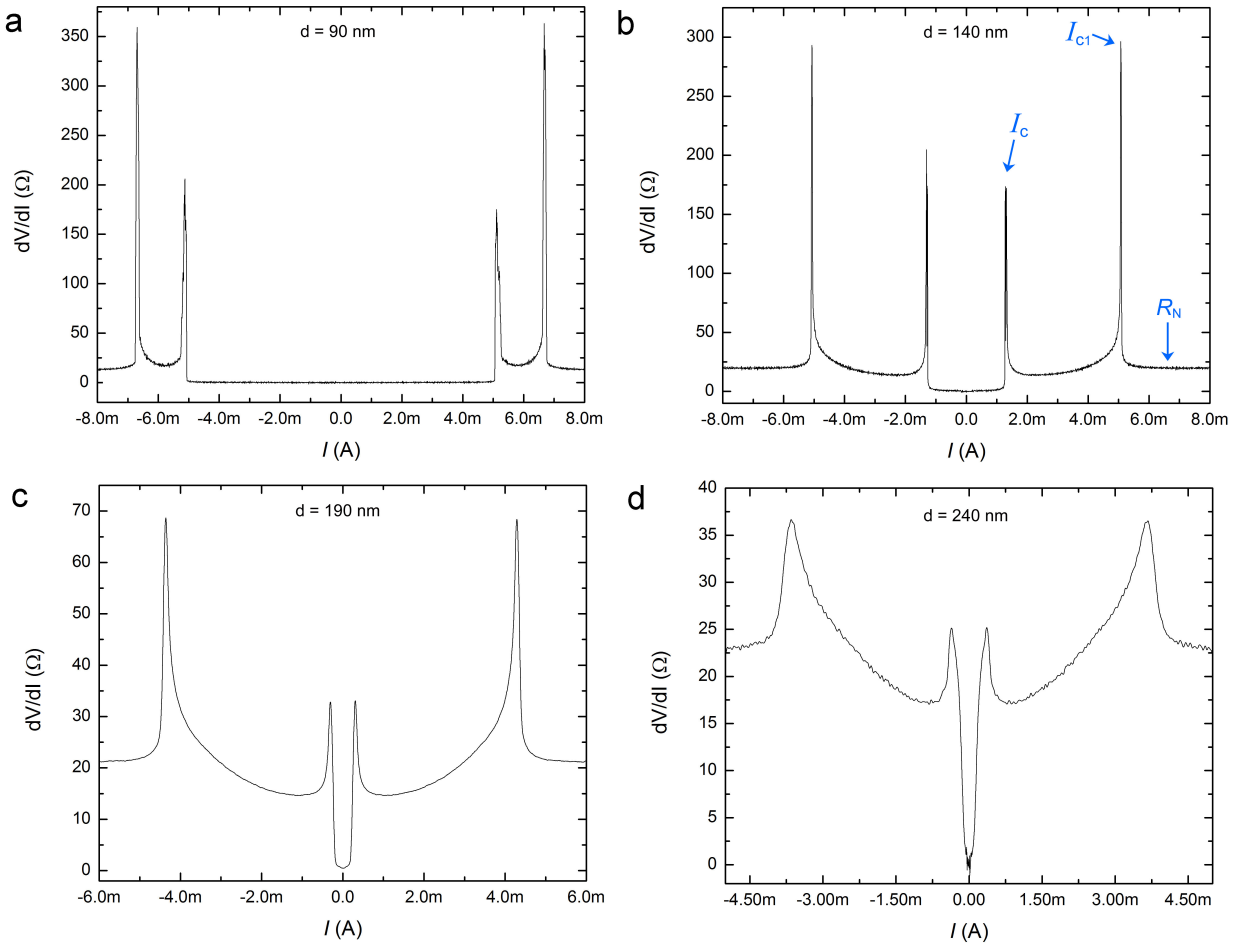

Figure 4.4: **Multiple Peaks in Current-Biased Differential Resistance Curves in Nb Arrays**. Differential resistance measurements for (**a**) 90-nm spaced islands at 2.327 K, (**b**) 140-nm spaced islands at 1.894 K, (**c**) 190-nm spaced islands at 2.411 K, and (**d**) 240-nm spaced islands at 1.755 K. For $I > 0$, the low current peak represents the critical current I_c of the device; the high current peak at I_{c1} may signify loss of superconductivity in the individual Nb islands.

In Figure 4.4, we observe four peaks. The curves are symmetric about $I = 0$. The low current peaks mark the critical current of the device, I_c, and the higher current peak may signify that of the individual Nb islands, I_{c1}. Notice that though the resistance versus temperature curves in Figure 3.1 showed a one-step transition to superconductivity for the 90-nm spaced islands, the two transition behavior is quite evident in the differential resistance measurement (Figure 4.4a) for this array. This section focuses exclusively on the high current peak I_{c1}.

The $I_c R_N$ product of Josephson junctions should be invariant; both the inverse resistance R_N^{-1} and critical current should scale with the junction size. By using BCS theory, Ambegaokar and Baratoff derived an analytical expression for the temperature dependence of the $I_c(T)R_N$ product for a junction of small

capacitance[86]

$$I_c(T)R_N = \frac{\pi\Delta(T)}{e}\tanh\left[\frac{\Delta(T)}{2k_BT}\right]. \tag{4.1}$$

There is no exact analytical expression for the temperature dependence of the superconducting energy gap; it can only be calculated numerically. Hence, we use two analytical approximations for the energy gap, each valid in different temperature ranges[87,88]. At high temperatures $T \approx T_c$

$$\Delta(T) \approx 1.74\Delta(0)\left(1-\frac{T}{T_c}\right)^{1/2}, \tag{4.2}$$

and at low temperatures

$$\Delta(T) \approx 1 - 3.33\left(\frac{T}{T_c}\right)^{1/2} e^{-1.76T_c/T}. \tag{4.3}$$

Figure 4.5 demonstrates the accuracy of each approximation within different temperature intervals[88].

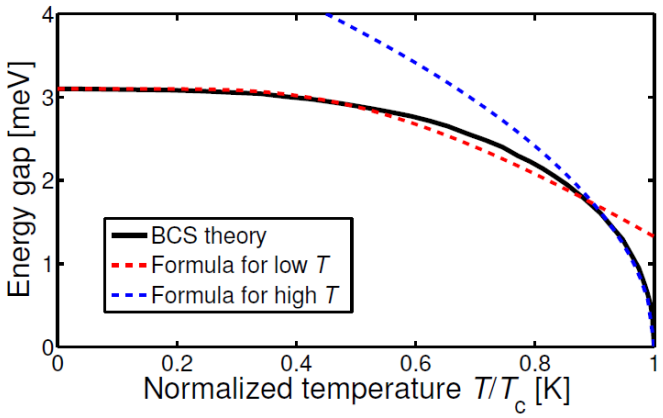

Figure 4.5: **The Energy Gap in Niobium**. The energy gap in Nb is plotted versus normalized temperature T/T_c. The red dashed curve shows the analytical approximation Eq. 4.3 and the blue dashed curve shows Eq. 4.2. The black solid curve is the numerical calculation of the gap. This figure was extracted from Kaiser[88].

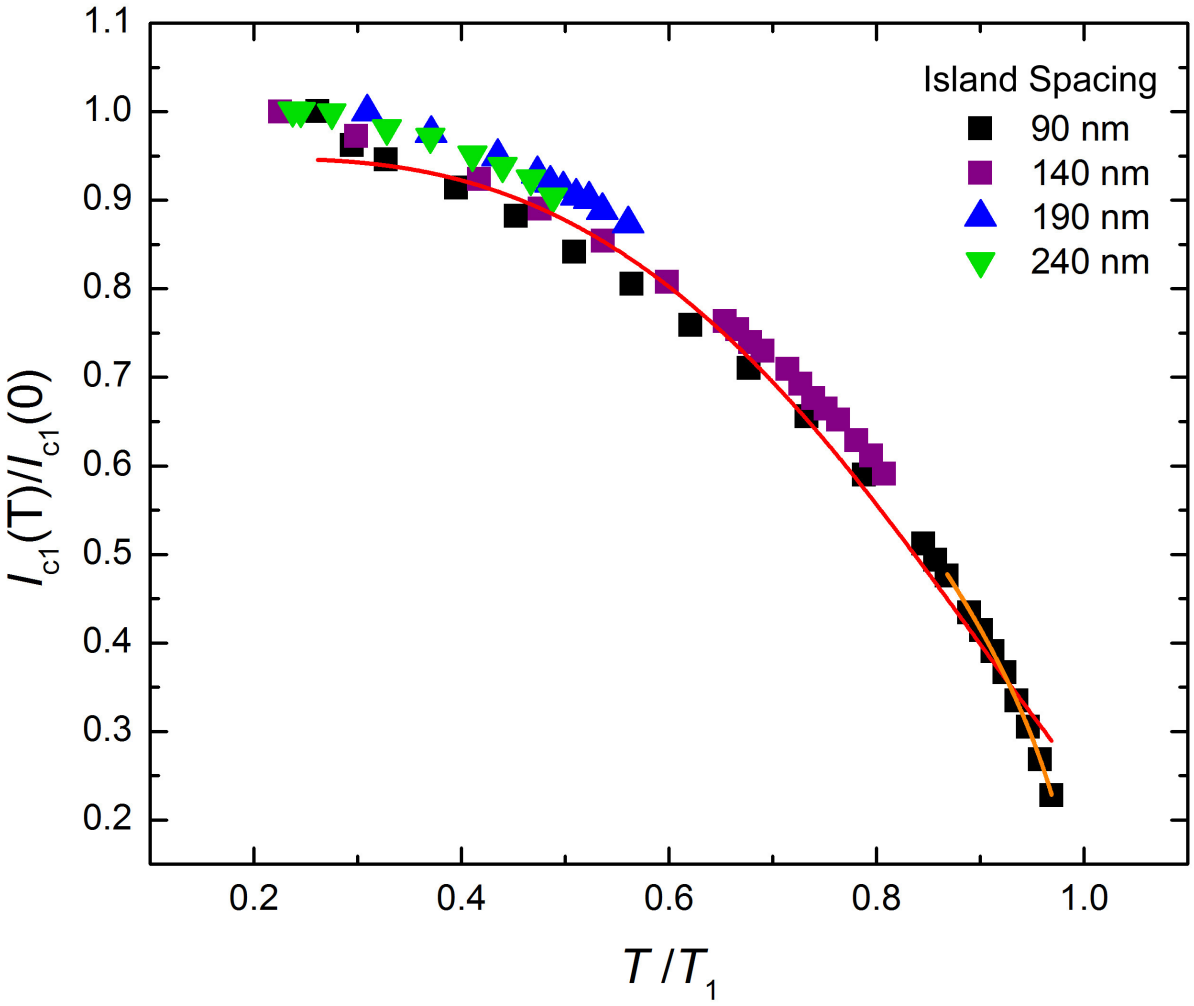

Figure 4.6: **Temperature Dependence of the Island Critical Currents**. The normalized critical current is plotted versus temperature for arrays with d = 90 nm, 140 nm, 190 nm, and 240 nm. Critical currents were extracted from the position of high current peak in the differential resistance. The critical current is normalized to $I_{c1}(0)$, which we approximated from our lowest temperature critical current measurements. The temperatures were normalized to an island critical temperature of T_1. The curves are fits to the Ambegaokar-Baratoff relation in Eq. 4.1; the red curve represents the fit using the low-temperature analytical approximation of the energy gap (Eq. 4.3), and the orange curve uses the high-temperature approximation (Eq. 4.2).

We extracted the island critical current I_{c1} at different temperatures from the position of the high current peaks in the differential resistance isotherms. Figure 4.6 shows the temperature dependence of the island critical currents arrays with $d = 90$ nm, 140 nm, 190 nm, 240 nm. We have limited data on these high current peaks; Joule heating prevented us from sweeping to high enough currents to accurately capture the peak for measurements in the ^{3}He and dilution cryostats. Also, we have limited temperature ranges for different arrays because we tended to stop collecting current-biased differential resistance data at temperatures only

slightly higher than T_2 for each array. Due to these limitations, $I_{c1}(0)$ for each array was taken to be the critical current at the lowest measured temperature interval; for all arrays the critical current appeared to saturate around this value. However, doing this introduces slight error, as the temperature was still fairly high.

Data for all arrays appears to fit along the same curve, meeting the predictions of an invariant $I_c R_N$ for Josephson junctions. As can be seen from the solid line fit, the critical current behavior accurately fits the predictions of Ambegaokar-Baratoff. The fit was specifically performed for $d = 90$ nm using an energy gap $\Delta(0) \approx 2.5$ meV.

As discussed in Section 3.3.1, each island becomes superconducting due to a combination of inter-island and intra-island coupling between the grains within an island. This analysis shows that, once an island *does* become superconducting, superconductivity within an island is orthodox; it can be described by simple microscopic theory based on the BCS theory.

Though our phenomenological model captures the general trends in the data, a few questions remain unanswered and prompt further investigation. We have yet to understand the linear relationship between T_1 and d, including the significance of the slope. If further investigation confirms that the properties of our individual islands are indeed completely consistent with the predictions of Ambegaokar-Baratoff, we may be able to better understand the intra-granular coupling that cooperates with inter-granular coupling to lead to the linear dependence of T_1 on d. The dependence of T_1 on island height z is still a mystery.

Chapter 5

Second Transition: Superconductivity Across the Array

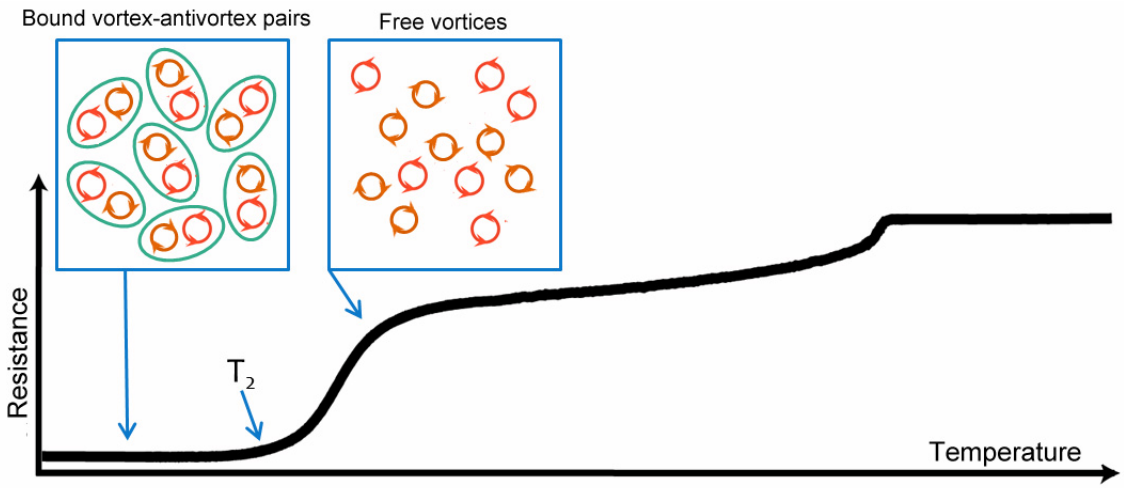

Figure 5.1: **Illustration of BKT Transition**. At high temperatures, phase fluctuations generate vortices and antivortices, which form pairs below a critical temperature.

As discussed in Section 1.4, 2D superconducting films and SNS arrays undergo Berezenskii-Kosterlitz-Thouless (BKT) vortex-antivortex binding transitions to a superconducting state. Resnick *et al.* observed a BKT transition in SNS arrays of large Pb islands. Though our results for T_1 in mesoscopic granular islands drastically differed from those of Resnick, we too observe a BKT transition in these arrays at a temperature we term T_2. Figure 5.1 illustrates the presence of free vortices above T_2, and bound vortex-antivortex pairs below T_2, which characterize BKT transitions.

5.1 Extracting T_2 from IV Isotherms

The zero-field IV characteristics can provide information on vortex dynamics in the system as well as proximity coupling, and are vital to accurately determining T_{BKT}. Applying a current across an array induces a Lorentz force on a vortex. The current acts as a driving force on vortices which competes with the pinning force created by Josephson coupling between the islands. This pinning force can be thought of as the maximum restoring force against fluctuations. The potential of a single vortex is $U_p(y) = -\frac{1}{2}E_B\cos(\frac{2\pi y}{a})$ such that the resulting pinning force is $F_P(y) = -\frac{dU_P}{dy} = -\frac{\pi}{a}E_B\sin\left(\frac{2\pi y}{a}\right)$ (for a current in the $\hat{x}$-direction causing a Lorentz force in the $\hat{y}$-direction), where a is the array lattice constant. We represent the energy barrier for a vortex to move from the center of one plaquette to the center of another plaquette as E_B, the maximum energy barrier for vortex motion. The full potential landscape for a vortex resembles an egg crate potential that tilts under an applied current. The position of lowest energy for a vortex is in the center of a plaquette. In triangular arrays, such as ours, the energy difference between a vortex in the center of a plaquette and directly between two islands on the edge of a plaquette[12] is $E_B = 0.043E_J$. (Note that this barrier is substantially higher in square arrays, $E_B = 0.199E_J$). In the case of overdamped junctions (i.e., metallic barriers with low capacitance) such as ours, quasiparticles diffuse rather than hop (single jump) over the barriers.

In the case of bound vortex-antivortex pairs of separation r under a Lorentz force $F_L = \pm\Phi_0\mathbf{j}\times\hat{y}$ ("+" is for vortices and "-" for antivortices), the current adds potential energy $U_I = -j\Phi_0 r$ such that we can use Eq. 1.6 on page 15 to find that the total potential energy of a pair is $U_B = 2\pi E_J\ln\frac{r}{a} - j\Phi_0 r$. ($U_B$ is the total potential energy a vortex must overcome to escape the potential, based on its position.)

Now, we discuss our results. The Berezinskii-Kosterlitz-Thouless transition temperatures T_2 were extracted from the temperature-dependent pulsed-IV characteristics. Below T_2, the Lorentz force from the finite excitation current used to measure resistance causes some vortex-antivortex pairs to unbind. The dissipation created by current-induced free vortices can overwhelm that caused by thermally unbound vortices near T_2, causing a measurable resistance at temperatures less than T_2. Consequently, it is standard practice to extract T_2 from IV characteristics instead of fitting the resistance versus temperature curves to the so-called flux flow resistance form $R(T) \propto n_{fT} \propto e^{-b/\sqrt{T-T_2}}$, where n_{fT} is the density of thermally generated free vortices[89].

By considering the rate of vortices overcoming the energy barrier U_B, and the rate of re-binding of pairs, the net density of current-induced free vortices is

$$n_{fI} \propto \sqrt{\frac{i_c(T)R_0}{\Phi_0}} \left[\frac{i}{i_c(T)}\right]^{\pi E_J/k_B T}. \tag{5.1}$$

This leads to an expected time averaged voltage $\langle V \rangle \propto n_{fI}$. So, $V \propto I^{\alpha(T)}$ describes the expected temperature-dependent IV characteristics of a 2D superconducting system, where

$$\alpha(T) = \begin{cases} = 1, & \text{if } T > T_2 \\ \geq \frac{2T_2}{T} + 1, & \text{if } T \leq T_2. \end{cases} \tag{5.2}$$

For $T < T_2$, the IV characteristics are expected to exhibit power-law behavior. For $T > T_2$, the arrays exhibit Ohmic resistance due to the motion of free vortices. There is a jump in superfluid density, and subsequently a jump in the temperature dependent exponent $\alpha(T)$ from $\alpha(T > T_2) = 1$ to $\alpha(T_2) = 3$. Referred to as the Nelson-Kosterlitz jump[90], this is considered a universal signature of a BKT transition, although finite-size effects and weak magnetic fields can smear this transition. We extract T_2 by finding the temperature at which the slope of the log I-log V plot is 3.

Current-voltage characteristics were measured using a Keithley 6221 AC/DC current source and 2182a nanovoltmeter. To minimize Joule heating, we used rectangular current pulses, with a current-on time of 3.5 ms and current-off time of 3 ms. A trigger timing cable connected the current source and voltmeter such that the output and readout were appropriately synchronized. See Figure 2.7 on page 34 for a schematic of our measurement set-up.

Figure 5.2 on page 59 shows a log-log plot of the IV isotherms for devices with 340-nm spaced islands, 590-nm spaced islands, and 640-nm spaced islands. From the insets, we can see a slightly smeared jump at $\alpha(T) = 3$ and extract $T_2 = 1.54$ K, $T_2 = 360$ mK, and $T_2 = 260$ mK for arrays with spacings $d = 340$ nm, $d = 590$ nm, and $d = 640$ nm, respectively. Note, however, that the low temperature behavior of $\alpha(T)$ vs. T does not resemble the expected power law form. Though the Nelson-Kosterlitz jump has proven a reliable means of determining $T_{\rm BKT}$, the theoretical prediction for the trend in $\alpha(T)$ for $T < T_{BKT}$ is generally considered incorrect[19,57,91,92]. Further, the jump is clearly more distinct in the devices with 590-nm and 640-nm spaced islands than the one with 340-nm spaced islands. A different four point pattern was used for the latter array, such that the number of islands in each of the former arrays is significantly higher. From this, we determine that finite sized effects may play a role in smearing the jump.

Additional errors in the extracted values for $T_{\rm BKT}$ can come from stray magnetic fields. IV characteristics measured in both the ^{3}He and dilution cryostats showed low current Ohmic tails in the log-log plots prior to setting an offset magnetic field (true zero-field) to account for trapped flux. Such tails are caused by

depinning of field-induced vortices. It is also likely that the arrays are sensitive to fields as low as the Earth's magnetic field. IV characteristics measured in the pumped ^{4}He cryostat always displayed small tails in the log-log plots. Unfortunately, the pumped ^{4}He cryostat was not equipped with a magnet at the time of this study, so no appropriate offset field could be set. Future studies may consider the use of μ-metal shielding to exclude magnetic fields.

Despite the error introduced by these tails, we are fairly confident in our data trend; a small field tends to slightly broaden the resistance versus temperature curves near the transition, but not effect the temperature at which we see a jump in superfluid density. In the dilution fridge, we compared the results of following the T_{BKT} extraction procedure for a sample in a field of 0.05 mT to the results in zero field. We did this for five arrays with island spacings d = 490 nm, 540 nm, 590 nm, 640 nm, and 690 nm. We also compared resistance versus temperature curves under both conditions. Under the small field, the resistance versus temperature curves were slightly broader near the transition. However, the extracted values of T_{BKT} were either identical to the zero-field results or higher by only up to 0.004 mK. This change is minute and well below the measurement resolution in the pumped ^{4}He system.

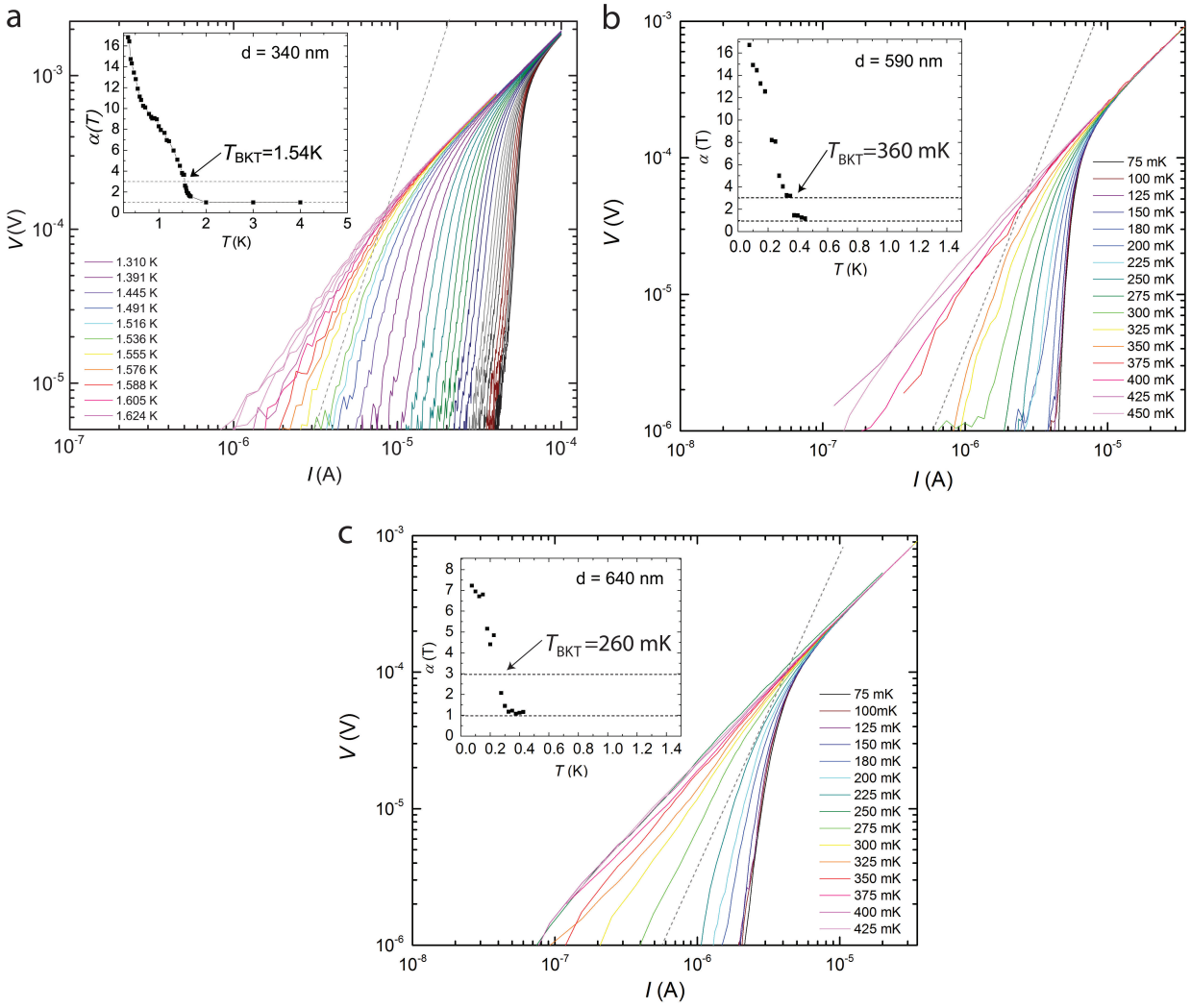

Figure 5.2: **Identification of BKT Transition**. Non-linear IV isotherms for (**a**) 340-nm spaced islands in array with 87-nm thick Nb (Sample **1**), (**b**) 590-nm spaced islands (Sample **4**), and (**c**) 640-nm spaced islands (Sample **4**), where $V \propto I^{\alpha(T)}$. A slope of $\alpha(T_2) = 3$ is marked by the dotted line. The **insets** show the evolution of the slope of the IV curves, $\alpha(T)$, with temperature and identifies the Nelson-Kosterlitz jump[90] in $\alpha(T)$ at T_2.

5.2 T_2 in Arrays with Island Spacings d = 90 – 690 nm

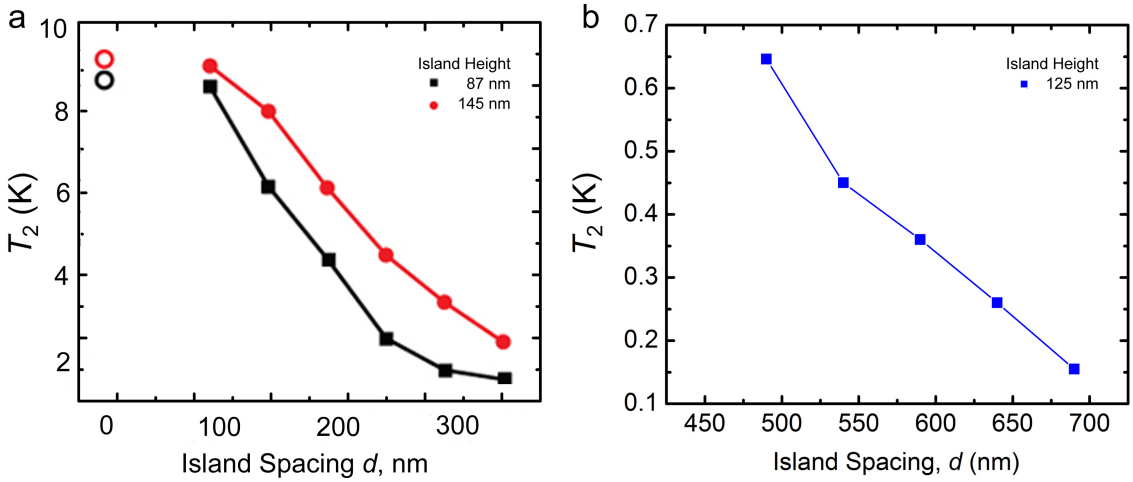

Figure 5.3: **Dependence of T_2 on Island Height and Spacing for d = 140 – 690 nm**. The temperature T_2 for each device was extracted from the IV isotherms (see Section 5.1) (**a**) The plot shows T_2 for each device versus edge-to-edge spacing, for 87-nm thick islands (black squares) and 145-nm thick islands (red circle). The open circles mark the T_c of the unpatterned bilayers (8.75 K and 9.1 K, respectively). This data was taken on Samples **1** and **2**. (**b**) T_2 versus spacing for 125-nm thick islands (Sample **4**).

Figure 5.3 is a plot of the BKT transitions in (**a**) samples **1** and **2**, and (**b**) sample **4**, which shows how T_2 decreases with increasing island spacing. For each device, T_2 was extracted by measuring the temperature at which the IV curves became non-linear, as described in the previous section. The data in Figure 5.3a also show that T_2 is more strongly depressed for the shorter islands in sample **1** than for taller islands in sample **2**.

In following section, we will look at the trend in the normal metal coherence length at the superconducting transition $\xi_N(T_2)$, and compare our results to LAT theory.

5.3 Comparison to Lobb-Abraham-Tinkham (LAT) Theory

Figure 5.4 shows the systematic dependence of $\xi_N(T_2)$ on island spacing, where the normal-metal diffusion constant $D \approx 94$ cm^2/s, as calculated in Section 2.2. Fits to LAT theory are shown as dotted curves. We observe $\xi_N(T_2)$ to vary approximately linearly with island spacing in samples **1** and **2** with spacings d = 140 – 340 nm. This approximate linearity is robust; it is also seen in arrays with further spaced islands d = 490 – 690 nm (Figure 5.5) and a diffusion constant $D \approx 96.6$ cm^2/s. This deviates from LAT theory both quantitatively and qualitatively. Not only does T_2 decrease more rapidly with island spacing than predicted, but it also depends strongly on island height.

LAT is explicitly valid for long junctions $d > \xi_N$, presumably our measurement regime. However, we can

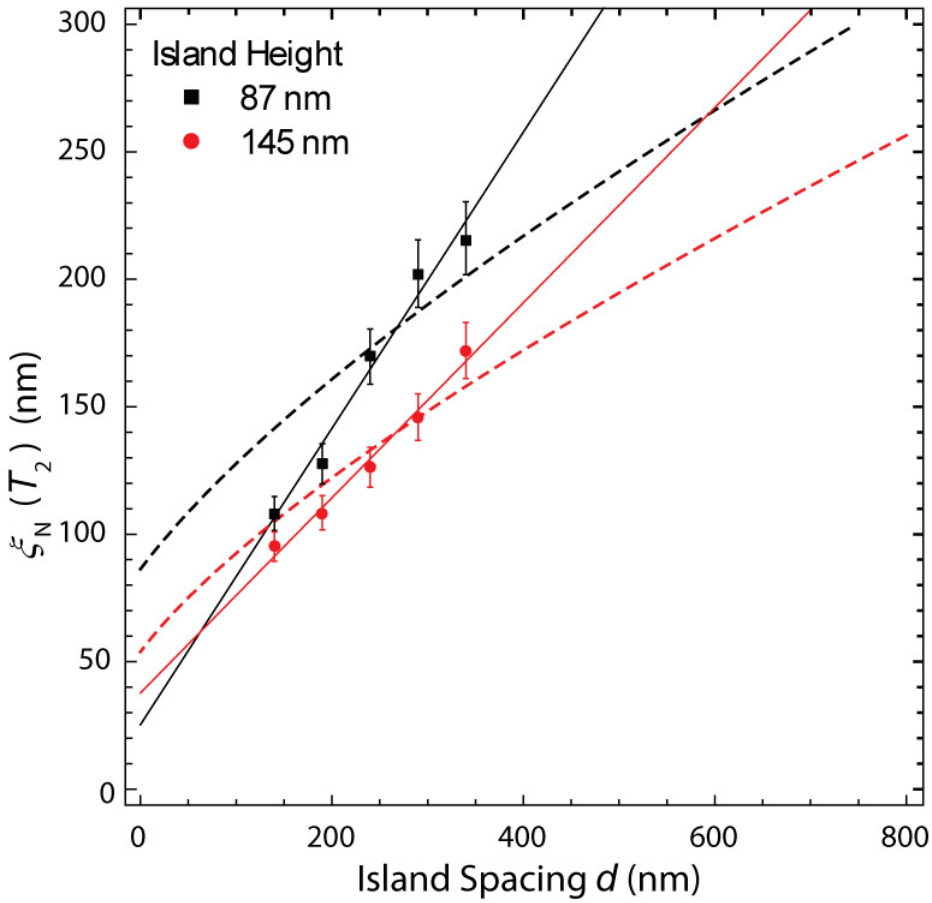

Figure 5.4: **Dependence of $\xi_N(T_2)$ on Island Height and Spacing for $d = 140 - 340$ nm**. The plot shows the normal-metal coherence length at T_2, $\xi_N(T_2)$, as a function of island spacing d. The temperature T_2 for each device was extracted from the IV isotherms (see Section 5.4). The error bars primarily result from to the standard deviation in the Au resistance at 10 K. Solid lines are linear fits and dashed lines are fits to LAT theory[12]. The point for the 90-nm spaced islands is excluded from the plot; the transition shows only one step and is therefore in a different regime.

obtain a linear relation between $\xi_N(T_2)$ and T_2 by modifying LAT using the expected inter-island coupling for closely-spaced islands $d \leq \xi_N(T_2)$. This quasiclassical $T = 0$ expression[61], $J' \sim 1/d^2$, yields a linear relationship. It does not, however, explain the dependence of T_2 on island height. As may be one of the reasons for the dependence of T_1 on island height, the islands may have a non-negligible charging energy that also accounts for the height dependence of T_2.

According to the LAT theory, the $T = 0$ state is always superconducting. No zero-temperature metallic state should appear. In Sections 5.5 and 5.6, we will more carefully look at the spacing dependence of T_2 over a wide range of spacings and present results demonstrating a possible metallic state in dilute arrays.

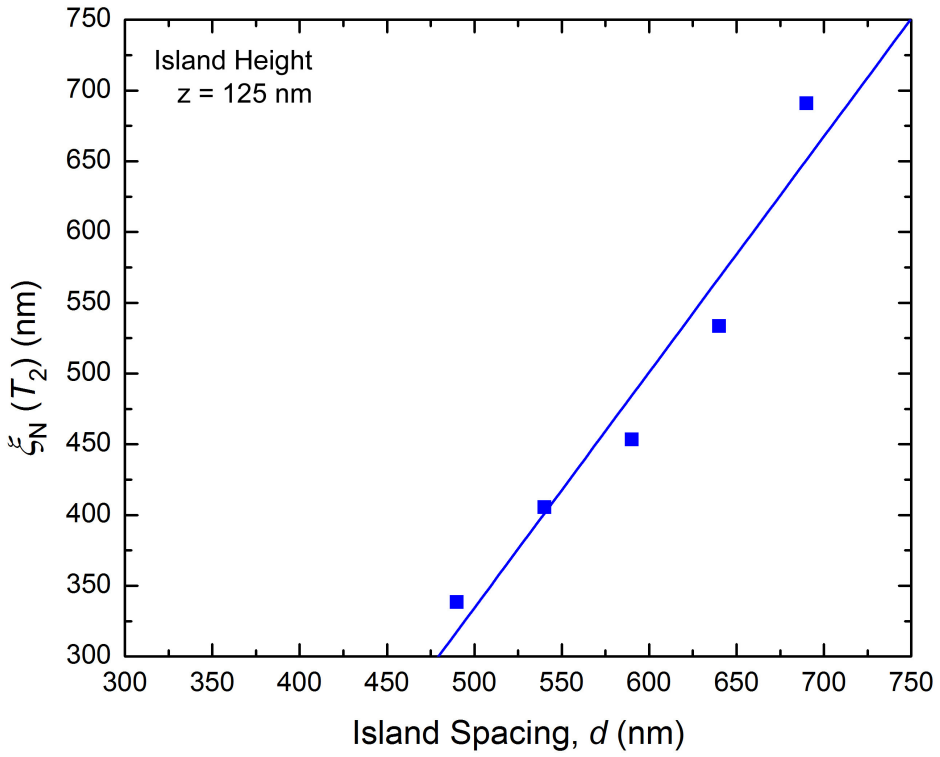

Figure 5.5: **Dependence of T_2 on Island Spacing for $d = 490 - 690$ nm**. The BKT transitions, T_2, in arrays with spacings $d = 140$ nm – 340 nm and island height $z = 125$ nm is plotted versus the normal-metal coherence length at T_2, $\xi_N(T_2)$. The solid blue line is a linear fit to the data; the transitions continue to occur when the normal metal coherence length is on the order of the edge-to-edge spacing (Sample **4**).

5.4 Understanding Inter-granular Coupling through IV Characteristics

The temperature dependence of the critical current can tell us about the nature of the proximity coupling in our arrays. The Josephson coupling energy in Josephson junctions is proportional to the critical current $I_c(T)$. So, understanding the temperature dependence of our critical currents should prove useful in understanding the proximity coupling, and subsequently the spacing dependence of T_2.

Figure 5.6 shows the $\frac{dV}{dI}$ vs. I at temperatures ranging from 107 mK to 900 mK for an array with $d = 490$ nm. Only one peak is evident for $I > 0$ because we were unable to measure $\frac{dV}{dI}$ at high currents where the second peak should appear; the effects of Joule heating dominate the results at higher currents due to limited cooling power in the dilution refrigerator.

Assuming the arrays have low capacitance, we can consider the expected IV behavior of a single, overdamped Josephson junction[93,94]

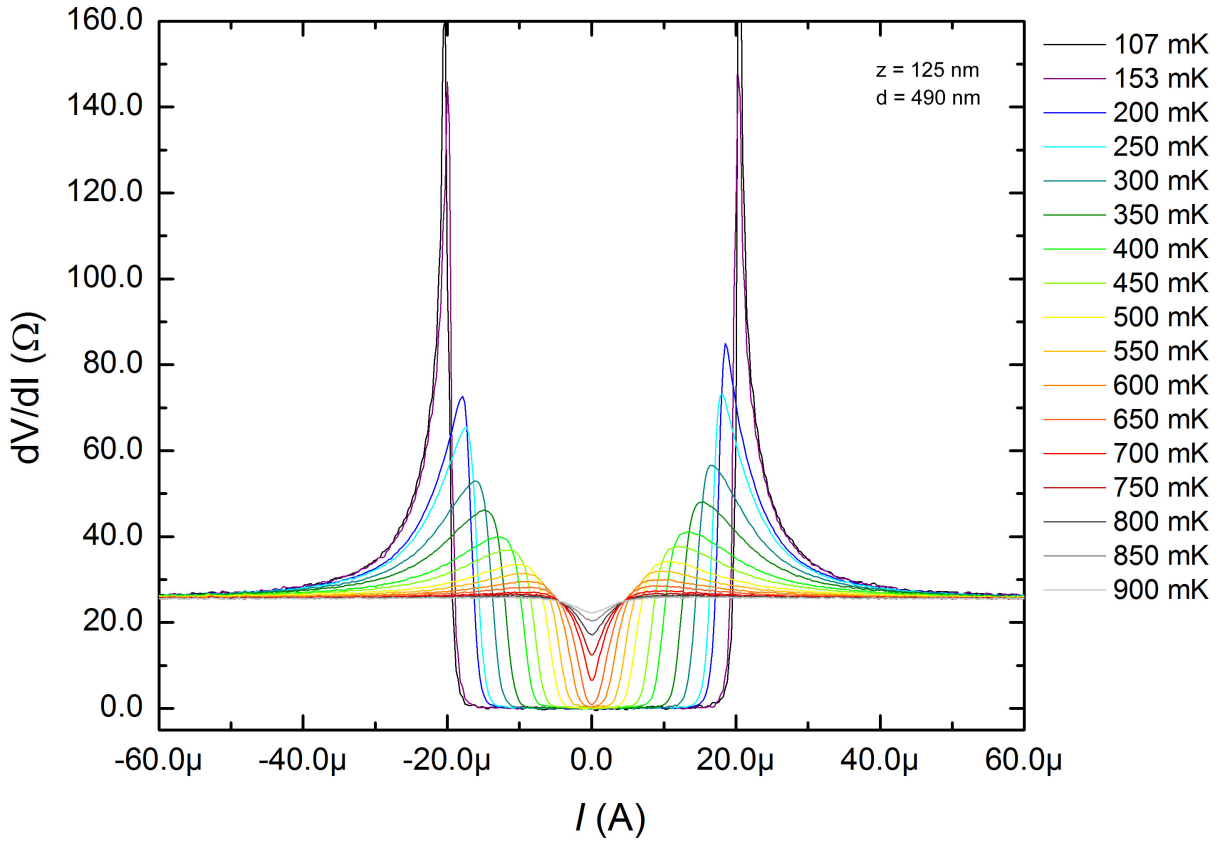

Figure 5.6: **Differential Resistance Isotherms in Array with Island Spacing $d = 490$ nm**. Current-biased differential resistance in 490-nm spaced islands (Sample **4**) taken at multiple temperatures $T = 107$ – 490 mK. The peak height and position are reduced with an increase in temperature. Note that only one peak is observed (for $I > 0$) because we were unable to sweep the current high enough to observe the second peak in the dilution cryostat to observe the second peak due to Joule heating.

$$\langle V \rangle = \begin{cases} 0, & \text{if } i_{dc} < i_c \\ R_n \sqrt{(i_{dc}^2 - i_c^2)}, & \text{if } i_{dc} > i_c. \end{cases} \tag{5.3}$$

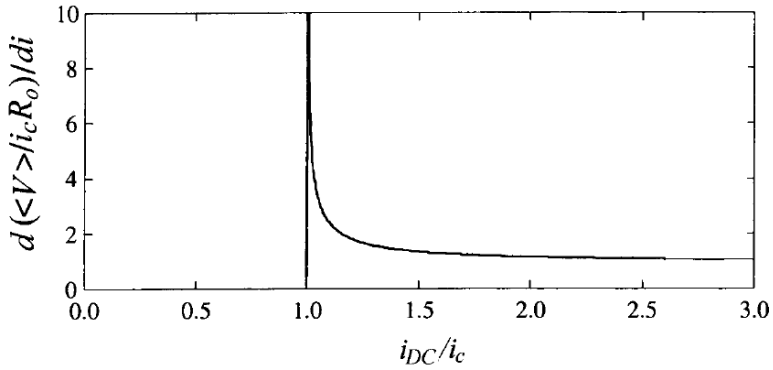

Figure 5.7: **Theoretical Current-biased Differential Resistance**. The plot shows the theoretical expectation for the differential resistance in accordance with Eq. 5.3. This image was extracted from Newrock [89].

Figure 5.7 shows the expected differential resistance in accordance with Eq. 5.3. The shape of the curves taken at the lowest temperatures in Figure 5.6 resembles that of the single junction result in Figure 5.7, having a very narrow peak. The slight amount of broadening could be due to thermal effects and any slight inhomogeneities between the junctions. As the temperature is increased, thermal fluctuations cause significant rounding and broadening of the peak. Given that thermal energy reduces the barrier height U_B, we see the critical current decrease with an increase in T. Lastly, the arrays exhibited no hysteresis in the zero-field IV characteristics, as would be expected from overdamped Josephson junctions.

As previously mentioned, the current-voltage relation Eq. 5.3 does not account for noise due to thermal fluctuations. This noise competes with Josephson coupling between islands; there is always finite resistance at low currents $I < I_c$ due to thermally activated phase slips. Ambegaokar and Halperin modified Eq. 5.3 for the case of a Josephson junction in parallel with a resistor and capacitor, known as the RSCJ model. This model considers the equation of motion of a junction with non-negligible capacitance:

$$C\frac{dV}{dt} = I - I_c(T)\sin\theta - \frac{V}{R} + L(t) \tag{5.4}$$

where L(t) is the fluctuation noise current, R is the junction resistance, θ is the difference in phases of the order parameters of the superconducting banks, and C is the junction capacitance.

By considering the Josephson equation for voltage (Eq. 1.6) and RSCJ equation (Eq. 5.4), they compared

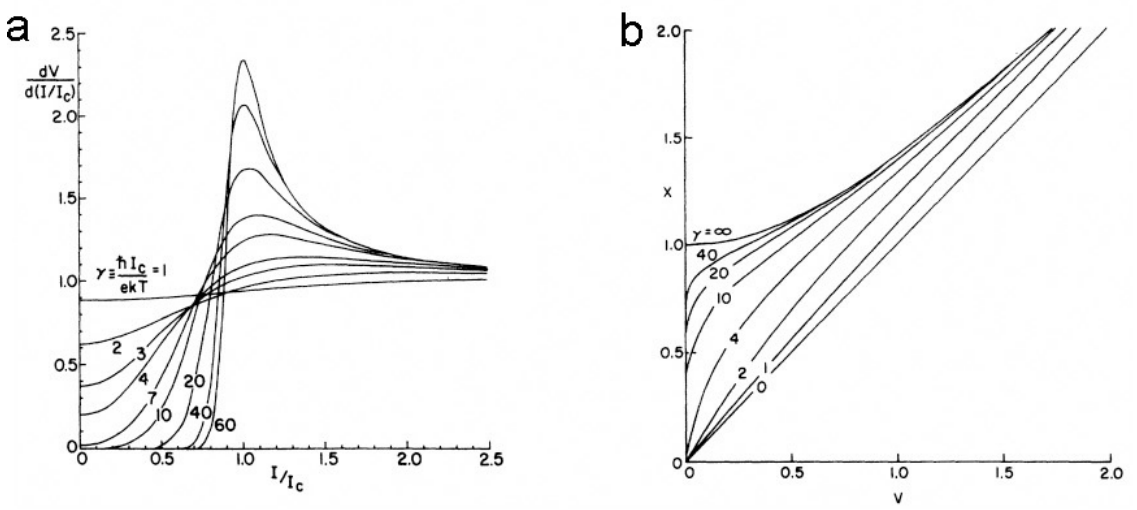

Figure 5.8: **Predicted Current-Voltage Characteristics in Junctions**. Rounding in the (**a**) differential resistance and (**b**) IV curves due to thermal noise[95].

the problem to the Brownian motion of a massive particle in a potential U. Their result is as follows:

$$\frac{\overline{V}}{I_c R_N} = \frac{4\pi}{\gamma}\{(e^{\pi\gamma x}-1)^{-1}\left[\int_0^{\infty} d\theta f(\theta)\right]\left[\int_0^{2\pi} d\theta' \frac{1}{f(\theta')}\right] + \int_0^{2\pi} d\theta \int_0^{2\pi} d\theta' \frac{f(\theta)}{f(\theta')}\}^{-1} \tag{5.5}$$

where $f(\theta) = \mathrm{e}^{U(\theta)/T}$, $x = \frac{I}{I_c(T)}$, and $\gamma = \frac{hI_c(T)}{2\pi e k_B T}$.

The analytic expression[96]

$$\frac{V}{I_c R_n} = 2(1-x^2)^{1/2} e^{-\gamma[(1-x^2)^{1/2} + x\sin^{-1}x]} \sinh(\frac{\pi\gamma x}{2}) \tag{5.6}$$

can be used in the case of small currents $x < 1$ and low temperatures $\gamma \gg 1$. However, there is no simple analytic result for the more general case[97]. More specifically, we are interested in fitting $I_c(T)$ for a wider range of temperatures, from low values $T \ll T_2$ to those near T_2. In fact, the only reason Eqs. 5.5 and 5.6 are displayed here is to justify our search for a simple, analytical approximation for $I_c(T)$; it can be quite cumbersome to fit the Ambegaokar-Halperin result to our experimental data, and requires extensive numerical analysis or simplification for limiting cases. Figure 5.8a shows the expected rounding of the differential resistance due to thermal fluctuations. This is clearly similar to the rounding we observe in the differential resistance in our arrays, as seen in the higher temperature curves in Figure 5.6.

From the Usadel equations, Dubos *et al.*[61] derived an analytical expression for the temperature dependence of the critical current for mesoscopic, diffusive SNS junctions. They considered a single junction with length significantly greater than the mean free path, but smaller than the dephasing length, which is appli-

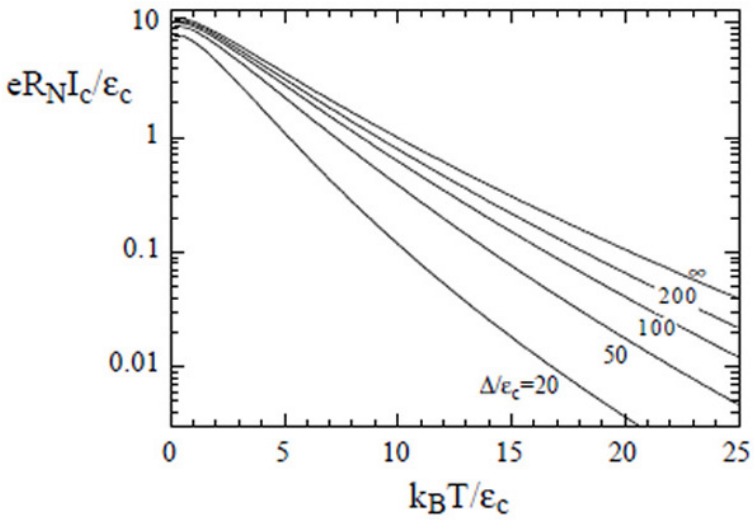

Figure 5.9: **Temperature-dependent Critical Currents in SNS Arrays**. Dubos *et al.*[61] performed numerical analysis on the Usadel equations to find $I_c(T)$ vs T for an SNS junction, and derived an analytical approximation, Eq. 5.7. This plot shows the results of their numerical analysis which, at low temperatures, fits Eq. 5.7. The results for junctions with a range of values of Δ/E_{TH}, labelled adjacent the curves, are shown, where ε_c is the Thouless energy (referred to in this thesis as E_{TH}). In the long junction limit, labelled $\Delta/E_{TH} \to \infty$, Dubos extracted the coordinates $a = 10.82$ and $b = 1.3$. The coordinates are expected to be less in the case of our arrays, as shown in Table 5.1.

cable to our system. They proceed to dichotomize their findings for the so-called short- and long-junctions limits based on comparing the system BCS energy gap Δ, to the Thouless energy E_{TH}. While the energy gap $\Delta \approx 1.76k_BT$ is merely set by the superconducting islands, the Thouless energy $E_{TH} = \frac{\hbar D}{d^2}$ accounts for the diffusion rate $\frac{E_{TH}}{\hbar}$ of electron pairs between the islands. Up to a distance d, only electrons of energy less than E_{TH} are paired. The long junction limit applies for $d \gg \sqrt{\frac{\hbar D}{\Delta}}$, meaning $\Delta \gg E_{TH}$; the short junction case is the opposite, $\Delta \ll E_{TH}$. So, in the short junction limit, the critical current is determined by the superconductor and in the long junction limit it is determined by the diffusion coefficient of the normal metal. Figure 5.9 shows a graph of the Dubos prediction for $I_c(T)$ vs. T and how it changes with $\frac{\Delta}{E_{TH}}$.

We calculate the energy gap from the transition temperature of the superconducting islands, T_1. As seen in Table 5.1, the energy scale of our arrays is $\Delta \approx 1 - 75$ times E_{TH}, falling into the intermediate to long junction limit regime.

In the low temperature limit and assuming a fully transparent interface, Dubos found the following analytical approximation to be fairly accurate:

$$\frac{eR_nI_c}{E_{TH}} = a\left[1 - be^{-aE_{TH}/(3.2k_BT)}\right]. \tag{5.7}$$

Coefficients a and b are found to be 10.82 and 1.3, respectively, in the extreme long junction limit $\frac{\Delta}{E_{TH}} \geq 100$.

Sample	d[nm]	T_2[K]	D[cm^2/s]	ξ_N[nm/T$^{-1/2}$]	$\Delta(0)$[meV]	E_{TH}[meV]	$\frac{\Delta}{E_{TH}}$	a	b
1	90	8.538	94.2	268	1.295	0.765	1.69	5.25	5.83
1	140	6.15	94.2	268	1.274	0.316	4.027	4.28	2.21
1	190	4.42	94.2	268	1.183	0.172	6.888	5.91	2.26
1	240	2.45	94.2	268	1.086	0.108	10.088	6.20	1.88
1	290	1.76	94.2	268	1.009	0.074	13.680		
1	340	1.53	94.2	268	0.905	0.054	16.881	7.85	2.27
4	490	0.646	107	285	1.181	0.029	40.278	9.38	2.87
4	540	0.45	107	285	1.156	0.024	47.850		
4	590	0.36	107	285	1.137	0.020	56.222		
4	640	0.26	107	285	1.125	0.017	65.450		
4	690	0.155	107	285	1.112	0.015	75.153		

Table 5.1: **Effective Energy Gap and Thouless energy in Nb Island Arrays**. The diffusion constant is calculated using the Einstein relation and the normal metal coherence length from $\xi_N(T) = (\hbar D/k_B T)^{-1/2}$, as described in Section 2.2. The effective energy gap was determined by the BCS relation $\Delta(0) \approx 1.76 k_B T_1$, and Thouless energy is $E_{TH} = \hbar D/d^2$. Given that our ratios Δ/E_{TH} are between 1 and 100, our junctions can be considered in the intermediate regime between the long- and short- junction limits. The last two columns show our results for the free fitting parameters from fitting to the Dubos $I_c(T)$ prediction noted in Eq. 5.7.

However, the formula was found to capture the trend of $I_c(T)$ in both the short and long junction cases. In the case that $\frac{\Delta}{E_{TH}} < 100$, the coefficient $a < 10.82$. In the short junction limit, $eR_n I_c(T=0) \approx 2.07\Delta$.

Figure 5.10 shows I_c vs T in our arrays with island spacings $d = 90$ – 490 nm, where I_c is extracted from the peaks in the $\frac{dV}{dI}$ vs. I. The peak occurs within 2% of the intrinsic critical current value if the dynamic resistance of the peak is at least 1.5 times[95] the high current $\frac{dV}{dI} \approx R_N$. As T approaches T_c, the peaks become broader and too low to accurately extract I_c. Subsequently, for the arrays with spacings of 540 nm to 690 nm, the accessible temperature range over which $\frac{dV}{dI}$ vs. I could be taken was not low enough to produce peaks above this threshold. Thus, we were unable to determine the temperature dependent trend in I_c for these devices. As can be seen from Figure 5.10 and Table 5.1, the analytic form of the numerical behavior qualitatively fits our results. The coefficients differ for all junctions because Δ/E_{TH} varies. The coefficient a is less than 10.82 in all cases, as expected for $\Delta/E_{TH} < 100$. Also as expected, as Δ/E_{TH} increases, a increases. In fact, the array with 490-nm spaced islands has the highest Δ/E_{TH} (≈ 40), and the coefficient $a = 9.38$ is fairly close to the long junction limit value. To our knowledge, the exact coefficients for different ratios of Δ/E_{TH} have not been published. Angers *et al.*[98] studied Al/Au/Al wires with Δ/E_{TH} ≈ 64 and 78. The corresponding coefficients, a, were found to be 7.22 and 6.125. This is very close to the extracted coefficients in our arrays.

This analysis shows that the coupling in our arrays is similar to that in a diffusive SNS wire. Though LAT is specifically formulated for an SNS array, models of single junctions *may* be more accurate for our systems. In the future, we would like to perform a more precise fit to these curves that does not involve two

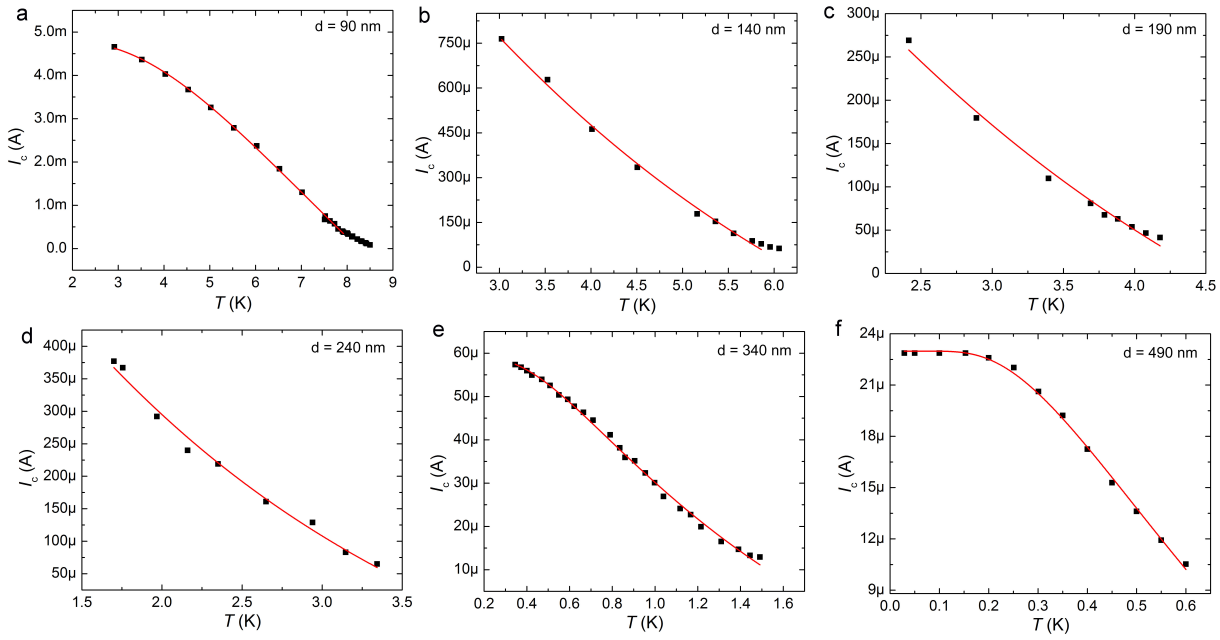

Figure 5.10: **Temperature Dependence of the Critical Current in Nb Arrays**. The critical current vs. temperature for arrays with spacings d = (**a**) 90 nm (**b**) 140 nm, (**c**) 190 nm, (**d**) 240 nm, (**e**) 340 nm, and (**f**) 490 nm. Each critical current value was extracted from the position of the low current peak in the current-biased differential resistance. The solid red curves are fits to the Dubos analytical expression (Eq. 5.7).

free fitting parameters; this may involve numerical analysis of the Ambegaokar-Halperin equations or other forms of the Usadel equations. In light of these results, in the following section we will analyze the trend in T_2 with island spacing d using a model of a diffusive SNS junction.

5.5 T_2 vs d: Comparison to Model of Single, Diffusive SNS Junction

As discussed in the previous section, in closely spaced junctions, the so-called short-junction limit, the maximum supercurrent the junction can carry will be determined by the energy gap Δ. In the long-junction limit, this critical current depends upon the diffusivity D of the normal metal; the characteristic energy scale of the metal is the Thouless Energy $E_{TH} = \frac{\hbar D}{d^2}$. Our junctions were shown to be in an intermediate regime (see Table 5.1); we might expect that the properties would thus depend on a combination of the energy gap Δ and the Thouless energy E_{TH}.

We also determined in Section 5.3 that the predictions of LAT do not fit our data well. LAT assumes that because electron pairs in a long junction diffuse a length of approximately $\xi_N \propto 1/\sqrt{T}$, the critical

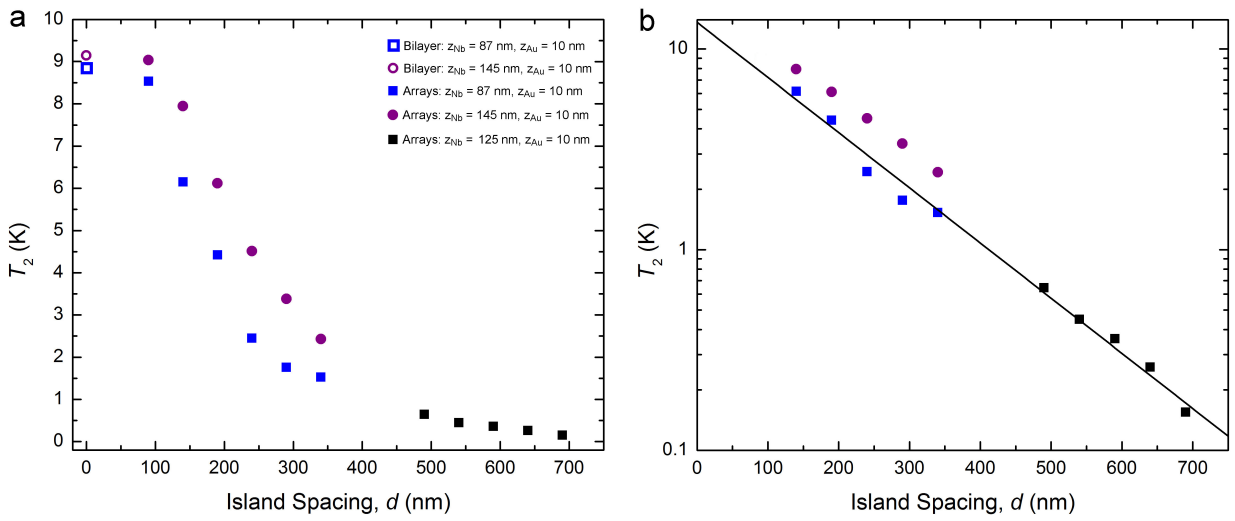

Figure 5.11: **Dependence of T_2 on Island Spacing**. (**a**) T_2 is plotted versus island spacing for three samples (**1**, **2**, and **4**). (**b**) Log T_2 versus island spacing. The linear fit shows that T_2 may exponentially decrease with an increase in d.

current relations should go as $i_c(T) \propto e^{-d\sqrt{T/\beta}}$, where β is a constant. However, we are not the only study that has found this relation inappropriate. LAT does not fit the predictions for a diffusive wire of mesoscopic S-N junctions, studied by Courtois *et al.*[99]. In the previous section, we showed that our arrays may in fact fit the predictions for a diffusive SNS wire better than that of LAT.

Courtois *et al.* studied a 1D series of Cu-Al junctions and a series of Ag-Al junctions. The height of the superconducting islands was greater than the Al coherence length ($z \gtrsim \xi_{Al}$), and thickness of the normal metal links were 100 nm. All wires studied were 80 μm in length, and they compared results for a range of island spacings $d = 0.4$ – 2.5 μm. Additionally, the samples were in the dirty limit $\ell \ll \xi$. Courtois *et al.* found that though the LAT prediction did not fit their data, $i_c(T) \propto e^{-T/\kappa}$ fit the data quite well, where κ is a constant. Based on this discrepancy, Wilhelm *et al.*[62] used the quasiclassical Usadel equations[59] to derive an approximation for the temperature dependence of the critical current in a 1D series of superconducting islands connected by diffusive normal metal links. By assuming that the longest junction in such a wire serves as the "bottleneck", they decided that the critical current of a single unit cell is sufficient to determine $I_c(T)$ for the entire system. Though in 2D arrays we are not limited by a "bottleneck", it may also be true that models of a single junction are sufficient to determine the properties of the critical current in our N such junctions. Suppression of the superconducting gap in the islands was neglected. In the low temperature limit $k_BT \ll E_{TH}$, they predicted that the critical current would be $i_c(T) = \frac{\Delta}{eR_n} \arctan\left(\frac{E_{TH}}{2\Delta}\right)$, which resembles that of the Ambegaokar-Baratoff relation for tunnelling between SIS junctions[86]. Specifically, it is similar to the $T \to 0$ Ambegaokar-Baratoff relation for non-negligible Δ/E_{TH}. Qualtitatively, this meets our criteria

for a model that considers both the energy gap and the Thouless energy, for our junctions in the intermediate junction limit.

The spacing dependence of T_2 on d for our arrays is plotted in Figures 5.11 and 5.12. We found that Wilhelm's result describes the spacing dependence of T_2 in our islands. We modify the LAT prediction $k_B T_2 \sim i_c(T)$ to use Wilhelm's approximation for $i_c(T)$ and find that

$$T_2 = \alpha \frac{\pi \Delta}{R_n e k_B} \arctan\left(\frac{E_{TH}}{2\Delta}\right). \tag{5.8}$$

Neglecting suppression in the superconducting energy gap $\Delta = 1.76 k_B T_c$ from the Au, we used $T_c = 9$ K. Being in the long junction limit $\Delta \gg E_{TH}$, the relation is fairly insensitive to this choice of T_c. For the normal resistance R_N, we use the sheet resistance $R_\square(10\text{ K}) \approx 6\ \Omega$. An average of the diffusion constants in both samples $D \approx 95.4\ \text{cm}^2\text{s}^{-1}$ is used to determine the Thouless energy E_{TH}.

The resulting prediction is shown as the solid curve in Figure 5.12, which fits the data decently. The only free fitting parameter we added is α, which we find to be $\alpha \approx 1.09$. Some error may come from the differences in island height between the samples that slightly shifts T_2.

There may be a variety of approximations that capture the trend quite well. Because $\frac{E_{TH}}{\Delta}$ is small in our arrays, $\arctan\left(\frac{E_{TH}}{\Delta}\right) \approx \frac{E_{TH}}{\Delta} \propto \frac{1}{d^2}$. So, we can conclude that $T_2 \propto \frac{1}{d^2}$ in our arrays. Also, from Figure 5.11b, T_2 appears to exponentially decrease with $T_2 \sim e^{-d/\tau}$, where τ is a constant. However, we have yet to determine the significance of this constant. On the other hand, the fit to Eq. 5.8 shown in Figure 5.11 fits the data without the flexibility of free fitting parameters.

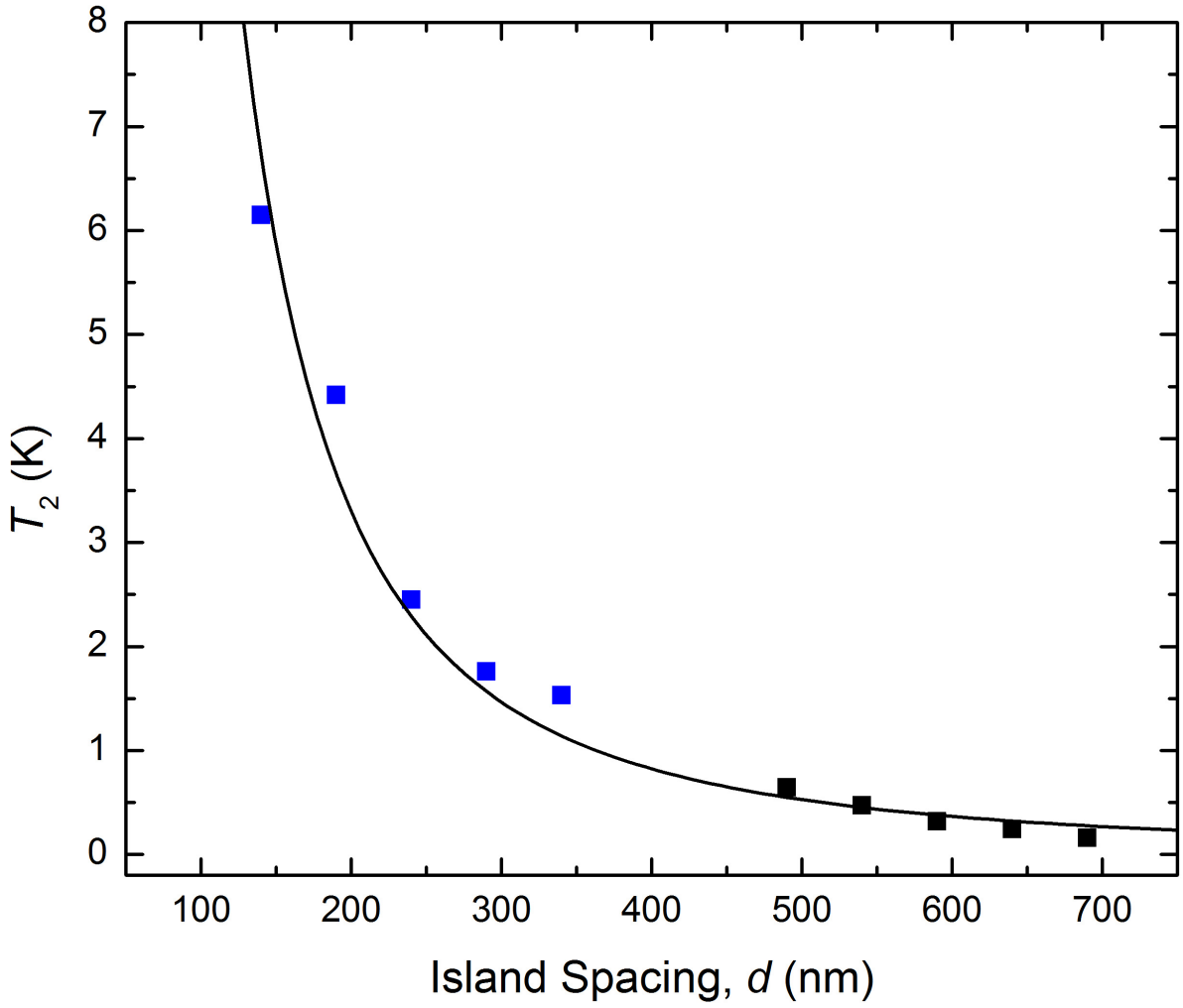

Figure 5.12: T_2 **vs.** d**: Fit to Single, Diffusive SNS Junction for Island Spacings** $d = 140 - 690$ **nm**. The blue squares are from sample **1** and black squares from sample **4**. The solid line is a fit to Eq. 5.8, where the only free fitting parameter is $\alpha = 1.09$.

5.6 Possible Emergence of a Metallic Phase in Arrays with Island Spacings $d = 740 - 1240$ nm

In the previous sections, we reported on arrays with a wide range of geometries, specifically islands heights $z = 34 - 145$ nm and spacings $d = 90 - 690$ nm. All of these arrays transition to a fully superconducting state below a T_2 measurable within the accessible temperature ranges of our cryostats. In Chapter 4, we introduced T_1 vs d data for islands with farther spacings $d = 740 - 1140$ nm. In this section, we will show the full resistance versus temperature curves in these arrays. We expected to either observe an incomplete transition down to 15 mK, or indications these arrays were no longer superconducting.

Figure 5.13 shows temperature dependent transitions in arrays with island heights z = 145 nm and d = 740 – 1240 nm. Capturing both transitions required the use of the pumped ^{4}He cryostat and dilution cryostat. Figure 5.13a is a merged plot of results from both cryostats; the break in the graph indicates the transition between systems. For clarity, Figure 5.13b shows the high-temperature results and Figure 5.13c the low-temperature ones.

The arrays with the closest island spacings, d = 740 nm, 840 nm, and 940 nm, exhibit a two-step transition to a state with finite resistance. The reason the high-temperature curve for the 740-nm spaced islands crosses that of the 840- and 940-nm spaced islands is not understood. It is, however, repeatable for this sample. Arrays with d = 1040 nm and 1140 nm exhibit only a one-step transition; there is a distinct T_1, but the resistance flattens out with a continued decrease in temperature. (Though it appears that $R(T \approx 20\text{ mK})/\text{R}(10\text{ K}) \gtrsim 1$, four of the curves shift consistently upon changing measurement systems). Unusual behavior is evident in the most dilute arrays (d = 1240 nm). As the array is cooled below 10 K, the resistance first increases, then decreases around the projected T_1. Upon further cooling, the resistance first decreases, then increases. This increase in resistance may be symptomatic of insulating behavior. The clear flattening of resistance at a finite value down to low temperatures is *possibly* indicative of a zero-temperature metallic state. Such a state is a clear violation of LAT and Anderson localization.

External sources of this resistance must be ruled out. Our measurement systems do not have copper powder microwave filters, which is something we can consider installing in the future. The sample is, however, mounted inside a radiation shield. Current-carrying wires attached to the sample make it difficult to reach low electron temperatures. The sample is mounted in a chip carrier, which is thermally attached to the mixing chamber through wires. These wires are well-thermally attached to copper and brass components on the coldfinger, and subsequently, to the mixing chamber. Despite these careful considerations, there is always concern over insufficient sample cooling. RuO_x temperature sensors are mounted both on the mixing chamber and on the coldfinger. Unfortunately, it is impractical to mount sensors directly on the sample. Temperature sensors mounted near the sample could continue to cool, when the sample itself has stopped cooling due to its connection to the transport wires. In this scenario, we would expect a flattening of resistance as the measured temperature continues to decrease. However, magnetoresistance measurements of our samples show a distinct difference in behavior at temperatures below 150 mK (see Figure 6.2), evidence that the samples do in fact sufficiently cool below 150 mK.

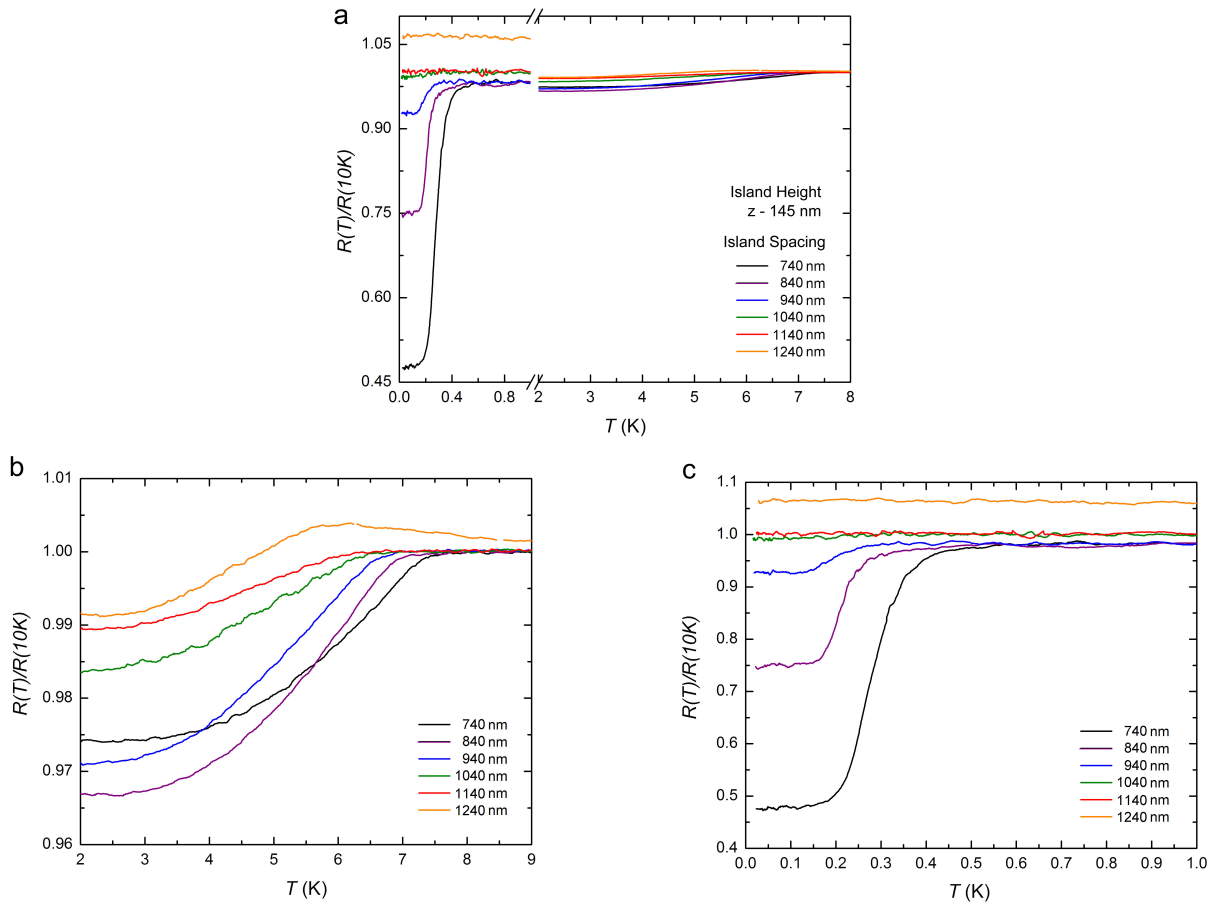

Figure 5.13: **Transitions in Nb arrays with Island Spacings d = 740 – 1240 nm: Possible $T \to 0$ Metallic State**. Temperature-dependent resistive transitions in arrays with six different edge-to-edge island spacings d. The island diameter is 260 nm for all arrays. The islands are 145 nm thick. Two different measurement apparatuses were necessary to capture both transitions. (**a**) A merge plot of the results from both systems. (**b**) The high-temperature resistive transitions were measured in a pumped ^{4}He cryostat down to $T = 1.8$ K, capturing transitions T_1. (**c**) The low-temperature transitions measured in the dilution cryostat down to $T = 15$ mK. The arrays with spacings $d = 740$ nm, 840 nm, and 940 nm undergo a two-step transition to a temperature-independent resistive state below $T \sim 170$ mK, 148 mK, and 133 mK, respectively. Arrays with $d = 1040$ nm and 1140 nm undergo a one-step transition; the resistance is temperature-independent below ~ 1 K. These five arrays appear to exhibit metallic behavior out to $T = 0$. Lastly, the resistance in the array with the farthest-spaced islands $d = 1240$ nm increases as temperature decreases, possibly indicative of insulating behavior. For more parameters relevant to this sample (Sample **5**), see Table 2.1 on page 30.

A 2D zero-temperature metallic state has been seen in very few systems. To date, we have not fully determined the origin and nature of this state in our devices. To better understand the metallic state observed in these arrays, we now review $T = 0$ metallic states reported in the literature.

In Section 1.4, we discussed the appearance of an anomalous intervening metallic states in the superconductor-to-insulator transition in granular films, an example of why the dirty boson model is considered incomplete. The mechanism behind low temperature resistive tails and subsequent characteristics of the metallic states in these films may differ from that in our regularly ordered arrays. Ultrathin, granular films have high disorder. The coupled grains have a wide range of junction capacitances, sizes, and separations; percolation effects may play an important role. Intervening metallic states in Josephson junction arrays may be a better comparison to our system may be an intervening metallic state in regular arrays of Josephson junctions.

Chen *et. al.*[26] observed a possible $T = 0$ metallic state in a regular array of superconductor-insulator junctions. Their research focused on angle-evaporated Al-AlO_x junctions; the insulating layer was sandwiched between 25-nm and 35-nm thick layers of Al. The junction size was 0.02 μm^2 and plaquette size was 1 μm^2. They measured the resistance in several different junctions, systematically changing the $\frac{E_J}{E_C}$ ratio. Arrays with $\frac{E_J}{E_C} \sim 4.8 - 7.8$ exhibited BKT transitions to a fully superconducting state and showed magnetoresistance oscillations consistent with magnetic frustration. However, the arrays with $E_J \sim E_C$ and normal-state resistances on the order of R_Q showed a flattening of resistance at low temperatures. Possible external causes of this resistance, such as self-heating from excitation currents or the existence of external magnetic fields, were ruled out. In order to rule out effects from microwave radiation, they installed additional copper powder filters and saw no change in the results. The authors attribute this flattening to vortex quantum tunnelling, which will be described below.

As previously described, the minimum energy state of a vortex places it in the center of a plaquette. Nevertheless, the vortex can appear anywhere in the array. In triangular arrays, such as ours, the energy difference between a vortex in the center of a plaquette and directly between two islands on the edge of a plaquette[12] is $0.043E_J$. The energy landscape set up by the array lattice resembles an "egg crate" potential, which is tilts under an applied current. At higher temperatures, vortex motion is thermally assisted; a vortex hops or diffuses over the energy barrier defined by this egg crate potential. At sufficiently low temperatures, thermal energy is too low to excite vortices. There is, however, a finite probability the vortex will move under the energy barrier, that is, quantum tunnel.

To characterize quantum tunnelling, one can consider a series of potential wells, $U(s)$, separated by barriers of height $H(x)$, where $x = I/I_c$. Let ω_0 be the natural frequency of a particle in a well and τ to be the transition rate of a particle out of the well. Thermal activation causes a particle to transition *over* the

barrier; quantum mechanical tunnelling causes it to transition *through* the barrier. The rate of macroscopic quantum tunnelling is[38,100]

$$\tau_{MQT}^{-1} = \frac{\omega_o}{2\pi}\left(\frac{b}{2\pi}\right)^{1/2} e^{-b} \tag{5.9}$$

$$b = \frac{\alpha H(x)}{\hbar\omega_0} + \frac{A(\Delta s)^2}{\hbar R}, \tag{5.10}$$

where α depends on the shape of the barrier, the second term in Eq. 5.10 is the correction for dissipation, R is the shunt resistance between wells, $A \sim 1$, and Δs is distance the under barrier. The crossover from thermal activation to quantum tunnelling[100] is projected to occur when $k_B T \sim \frac{1}{7}\hbar\omega_0$. Dissipation reduces this critical temperature[38].

A 1981 study showed evidence of macroscopic quantum tunnelling of vortices below 100 mK in arrays of 20,000 Nb-NbO_x junctions, each 1 μm^2 in size[100]. Using a low-frequency AC signal, they mapped out the distribution of currents at which superconductivity was destroyed in the junctions. These probability distributions, $P(I)$, were measured at different temperatures down to 3 mK [(1)]. The distribution widths decreased with a decrease in temperature (a decrease in I_c) down to 100 mK, at which point the width becomes temperature independent. Relating the transition rate to the probability distribution through the relation $P(I) = \tau^{-1}(I)|dI/dt|^{-1}[1 - \int_0^1 P(i)di]$, they extracted the transition rate due to thermal activation versus that due to quantum tunnelling. Quantum tunnelling dominated below 100 mK and the effects of dissipation on the transition rate were systematically and predictably less evident with a decrease in temperature. To our knowledge, vortex quantum tunnelling has not been observed in SNS arrays. Dissipation suppresses the probability of the tunnelling of a vortex[38], but sources of dissipation are thought not to survive down to $T = 0$. It is possible that we observe macroscopic quantum tunnelling in our arrays. We are unsure as to whether we can investigate this with our present measurement scheme; this warrants further investigation.

Now, we compare the results to phase separation models. According to the Feigel'man model, we would expect a transition to a metallic state at a critical spacing $d_c \sim 5$ μm, based on the size of our islands and high conductivity of our system. This is at significantly farther spacing than where we see a transition. Similarly, the critical temperature T_2 in our islands falls faster with an increase in spacing than would be predicted by LAT. It is possible that this faster suppression is caused by a non-negligible charging energy competing with superconductivity across the arrays. As previously mentioned, evidence of the significance of this charging energy comes from the height dependence of both critical temperatures.

[1]The sample was mounted inside the ^{3}He-^{4}He mixing chamber

In comparison to the Spivak model (page 20), the trend in T_2 with inverse island density in our arrays is *qualitatively* very similar to their phase diagram. However, as of yet, it remains unclear whether it is quantitatively similar. Figure 5.14 is a roughly sketched phase diagram of these granular Nb arrays on Au. The highest concentration of islands should show a single-step transition to superconductivity because $d \sim \xi_N(T_{c,Nb})$; these arrays would definitely be in the short-junction regime may exhibit different behavior from arrays with farther spacings. This regime is outlined by the dotted, purple curve. The solid curve is a connection between the data for T_2 versus inverse island density in our arrays. Within this solid line, the arrays exhibit clear two-transition behavior – equivalent to the "sc puddles" regime noted in the Spivak phase diagram. Similar to the Spivak model, the arrays transition to a metallic state at a critical concentration. As we continue to increase the island spacing, hints of an insulating state appear in the most dilute array. Given evidence of an insulating phase, one could surmise that the localization length in the system can not be neglected, as it is in the Spivak model.

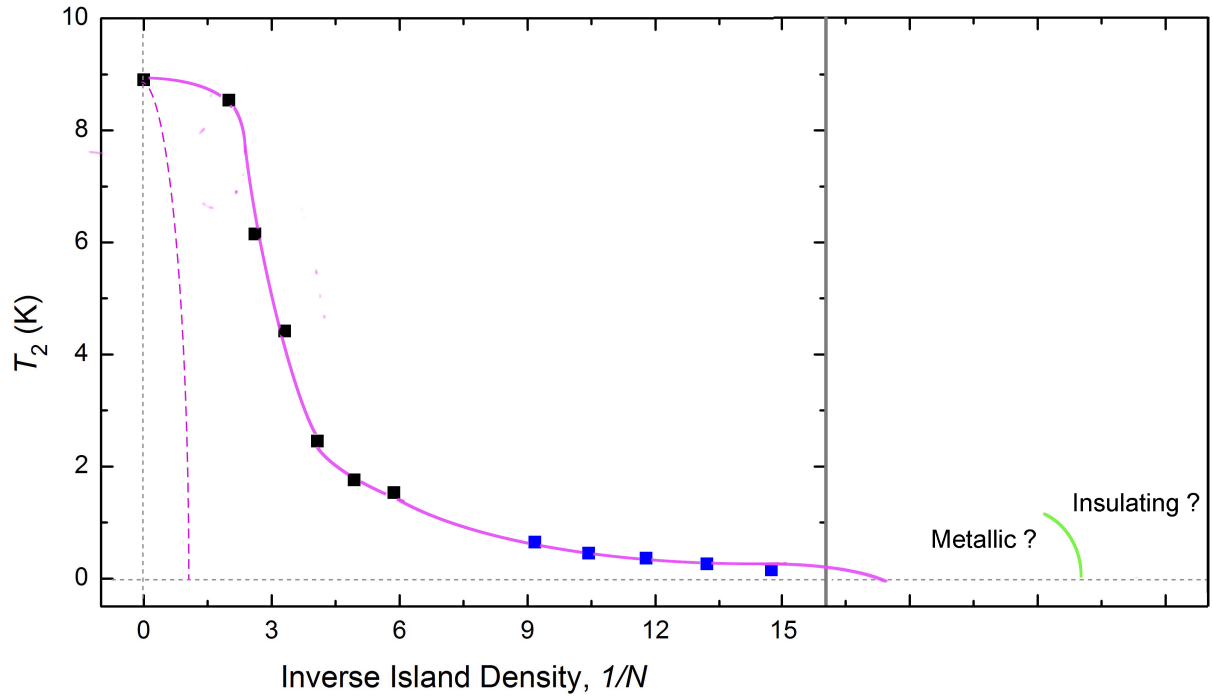

Figure 5.14: **Sketch of Temperature vs Island Concentration Phase Diagram: Arrays of Nb Islands on Au**. This sketch shows the Temperature vs Inverse Island Density in our arrays. The data points are our actual T_2 values for different inverse island densities from samples **1** and **4**. The purple solid line is a drawn between the data points as a guide to the eye. The purple dashed line is a rough, qualitative separation between the single-step and two-step transitions in the resistance versus temperature behavior. At a critical inverse island density, we see a transition to a metallic state. At a higher critical value, we see a possible insulating state. This illustration is intended for direct qualitative comparison to the phase diagram in Spivak *et al.*, shown in Figure 1.10 on page 20.

Chapter 6

Effects of a Perpendicular Magnetic Field

6.1 Magnetic Frustration

In Section 1.6, we discussed how at $T = 0$ and $B = 0$, the energy of a SNS array is minimized when the phases of the islands are identical, therefore, no vortices exist in the system. However, in a magnetic field, the presence of a vortex can be energetically favorable.

For $B \neq 0$, Eq. 1.4 becomes

$$\sum_{junctions} \gamma_{ij} = 2\pi(n-1) \tag{6.1}$$

$$\sum_{junctions} (\Delta\phi_{ij} - \frac{2e}{\hbar}\int_i^j A \cdot dr) = 0. \tag{6.2}$$

The lowest energy state of the system is found when $n = 1$; the phase difference $\Delta\phi_{ij}$ can vary to cancel the vector potential term. First of all, for convenience, we can define the externally applied field in terms of the number of flux quantum per plaquette, $f = \frac{BA}{\Phi_0}$, known as the magnetic frustration. Revisiting the Hamiltonian of the system for $B = 0$, Eq. 1.5, we can modify this using a gauge $A = B \times \hat{y}$ and find the potential energy of the system for non-zero field

$$H = -\sum_{<ij>x} E_J \cos(\Delta\phi_{ij}) - \sum_{<ij>y} E_J \cos\left[\Delta\phi_{ij} - 2\pi f n(j-1)\right], \tag{6.3}$$

where $\sum_x$ sums across junctions parallel to the x axis, $\sum_y$ across those parallel to the y axis, and $\langle ij \rangle$ sums over nearest neighbors. (We assume that, by the Meissner Effect, magnetic flux is excluded from the

individual islands).

From the second term in the Hamiltonian we can clearly see that (a) a non-zero $\Delta\phi_{ij}$ can be energetically favorable, (b) the frustration dictates the difference in phases $\Delta\phi_{ij}$ required to minimize the system energy, and (c) for integral f, the minimum energy state can be found either if the phases of the islands in a plaquette are equal or wrap around by exactly 2π. It is impossible, however, to minimize all junction energies for non-integral f; the system is frustrated.

As the field varies, the vortex configuration in the system will vary. Vortex motion is dissipative, creating resistance in the array. Experimentally, this manifests itself as periodic variations in resistance as the field is varied. At certain rational values of frustrations, vortices are pinned, indicated by dips in the magnetoresistance. In the case of a triangular array, these dips[101] are expected to occur at $f = \frac{1}{20}, \frac{1}{7}, \frac{1}{6}, \frac{1}{4}, \frac{1}{3}, \frac{3}{8}, \frac{2}{3}, \frac{1}{2}, \frac{3}{5}, \frac{5}{8}, \frac{2}{3}, \frac{3}{4}, \frac{5}{6}, \frac{6}{7}, \frac{19}{20}$, and 1. Such magnetoresistance oscillations have been measured in arrays of Josephson junctions[25,26,92,101] and superconducting films with periodic pinning centers[102]. Figure 6.1 is a schematic of these magnetoresistance oscillations and corresponding illustrations of the vortex configuration for the $f = \frac{1}{2}$ and $f = \frac{1}{3}$ cases.

Magnetoresistance measurements were taken in either the ^{3}He or dilution cryostat using a similar set-up to that described in Section 3. Most measurements involved an excitation current of 500 nA. At base temperature, this excitation current is significantly lower than the critical current in the arrays. Additionally, no measurable effects due to Joule heating were observed using this value. The magnetic field was swept at 5 mT/min, for measurements taken in a ^{3}He fridge, and 1 mT/min for those taken in the dilution refrigerator. These slow sweep rates were determined as optimal for reducing the generation of eddy currents and subsequent additional heating. In all results presented here, the field was swept up from the minimum value. Additionally, the lock-in amplifier and voltage pre-amplifier were wrapped in aluminium foil to exclude noise from the magnet power supply [(1)]. The magnetoresistance plots in Figure 6.2 on page 80 show clear evidence of magnetic frustration in arrays with island spacings $d = 490$ nm and 690 nm at a wide-range of temperatures below and above T_2. Magnetic frustration data for arrays with island spacings $d = 290$ nm, 540 nm, 590 nm, and 640 nm can be found in the Appendix (C). Our arrays show periodic variations in resistance in response to a magnetic field, exhibiting weak dips at $f = \frac{1}{8}, \frac{1}{6}, \frac{3}{8}, \frac{2}{5}, \frac{3}{5}$, and $\frac{5}{6}$, and deeper minima at $f = \frac{1}{4}, \frac{1}{3}, \frac{1}{2}, \frac{2}{3}, \frac{3}{4}$, and 1. As expected, for magnetoresistance curves taken below T_2, the arrays return to a completely zero resistance superconducting state at $f = 1$, when there is one vortex pinned in every plaquette. At $f = \frac{1}{2}$ and $f = 1$, the ground-state energy per junction is higher than the zero-field ground state energy, making it less stable to thermal fluctuations. Hence, as we increase the temperature,

[1] In the past, we found that noise from the magnet power supply can lead to high "y" components in the lock-in voltage read-out that would normally indicate high sample impedance or capacitance.

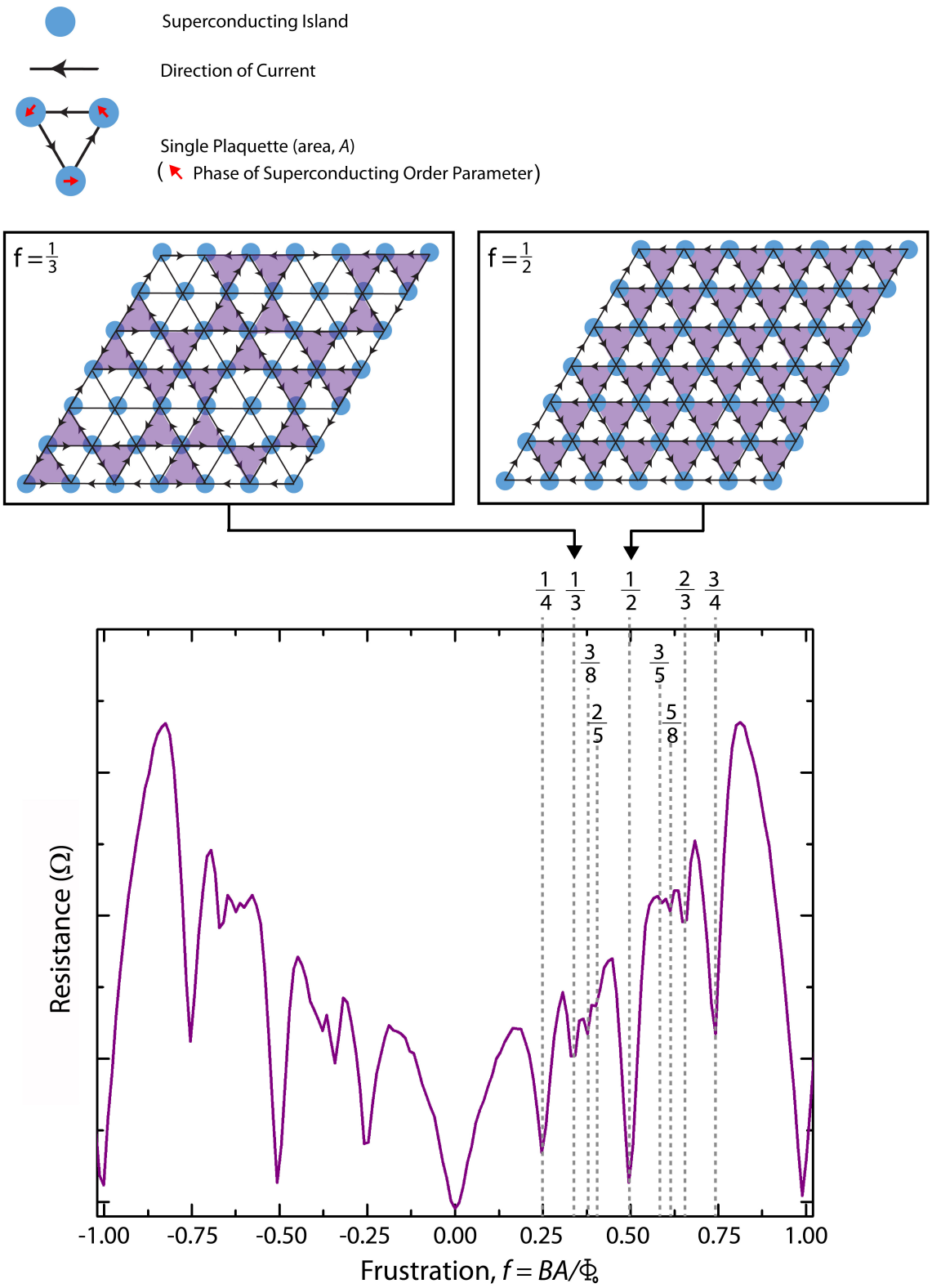

Figure 6.1: **Schematic of Magnetic Frustration**. Plot shows magnetoresistance oscillations in our frustrated, triangular arrays. The vortex configuration for (**left**) $f = \frac{1}{3}$ and (**right**) $f = \frac{1}{2}$ are schematized above the plot. Shaded purple regions represent the position of vortices of positive vorticity.

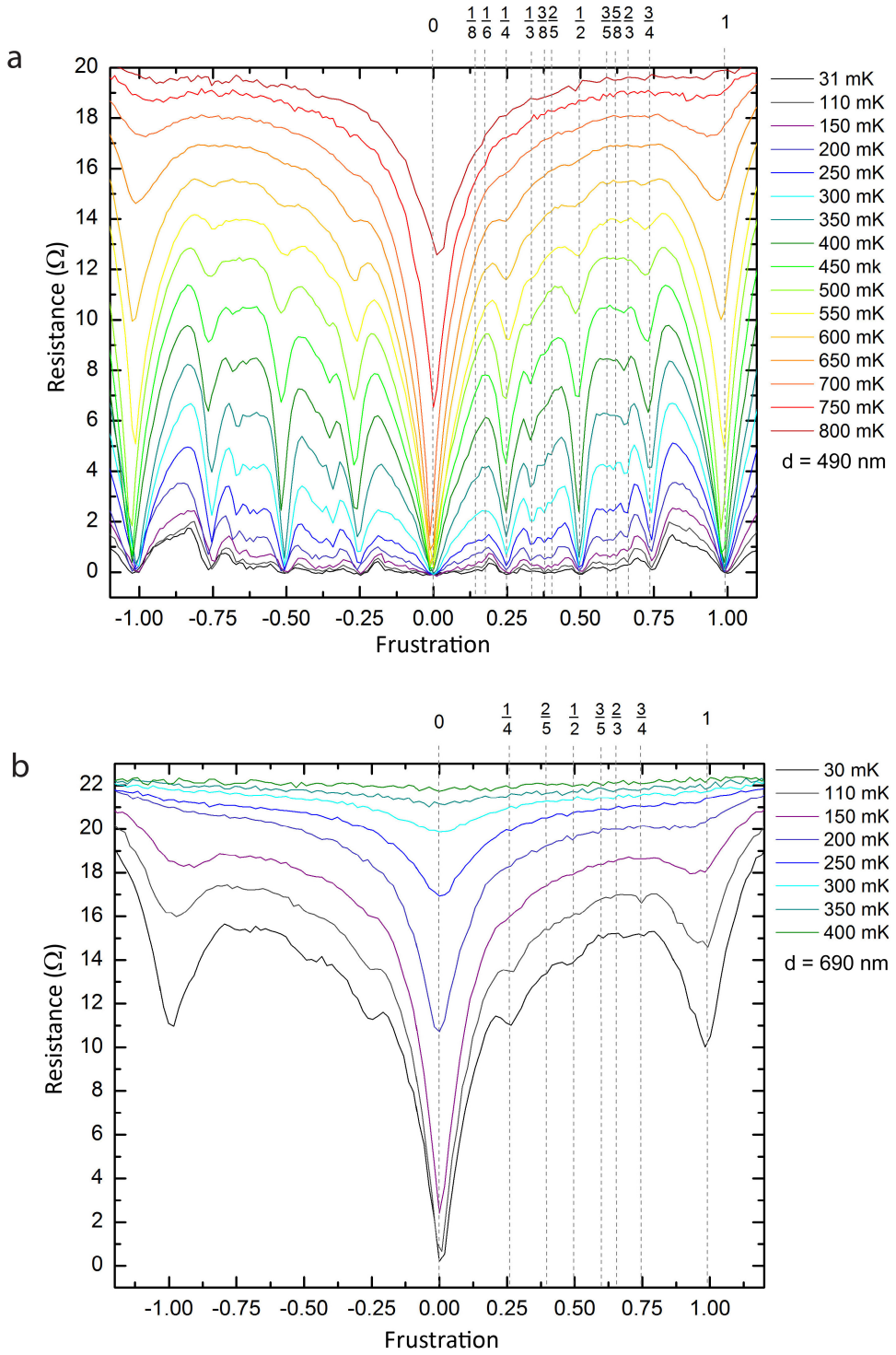

Figure 6.2: **Magnetic Frustration in Nb Arrays**. Magnetic frustration is a manifestation of competing magnetic ground states. The plots show the evolution of magnetoresistance oscillations in arrays with $d =$ (**a**) 490 nm and (**b**) 690 nm at a range of temperatures. Dips occur at rational values of frustration $f = \frac{BA}{\Phi_0}$, where the area of the plaquette is A, and B is an applied, perpendicular magnetic field.

the magnetoresistance dip at $f = \frac{1}{2}$ rises faster than both the $f = 0$ and $f = 1$ dips. In general, the depth of the dips is consistent with the theoretical prediction for the ground-state energies at different values of frustration for triangular arrays[103], shown in Figure 6.3. Frustration values $f = 0, \frac{1}{4}, \frac{1}{2}, \frac{3}{4}$ and 1 show the deepest dips. At these configurations, the vortex superlattices is most strongly coupled to the egg crate potential lattice; we will refer to these configurations as strongly commensurate. Given that the Hamiltonian in Eq. 6.3 includes an even function (cosine), the magnetoresistance oscillations should not depend on the sign of the field. Our results are symmetric across $f = 0$.

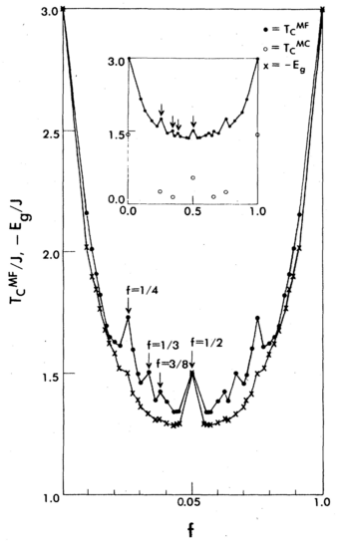

Figure 6.3: **Predictions of the Ground State Energy and Transition Temperatures of Arrays in Different Fields**. The plot show the predicted mean field transition temperatures, T_c^{MF} (dots), and ground state energies E_g (x), for a triangular array at different values of frustration. The data points are their results for discrete values of frustration. The line is just a guide to the eye; $E_g(f)$ and T_c^{MF} may have richer structure than detailed here. The **inset** shows estimated Monte Carlo transition temperatures T_c^{MF} (open circles) for $f = 0$, $\frac{1}{4}$, $\frac{1}{3}$, and $\frac{1}{2}$. For more information, please refer to Shih *et al.*[104], from which the figure was extracted.

At very low temperatures $T \ll T_2$, the pinning barrier is strong enough that we are unable to measure the magnetoresistance oscillations below the voltage sensitivity of our lock-in amplifier. This was evident for the arrays with spacings of 90 nm, 140 nm, and 190 nm; we only have a magnet in the ^{3}He and dilutions fridges so the accessible temperature range was too low to measure magnetoresistance. We can, however, increase the barrier by increasing the applied current. A higher excitation current increases the magnitude of the oscillations either due this or to Joule heating. Increasing the sweep rate of the magnetic field has the same effect, due to heating from induced eddy currents.

Figure 6.4 shows a comparison of results for different arrays at a fixed temperature $T \approx 30$ mK. From the T_1 vs spacing data, we know that individual islands in denser arrays become superconducting at higher

temperatures than ones in more dilute arrays. This means that at a fixed temperature, the effective radii of islands in denser arrays should be greater than that in the sparser arrays. Hence, changing the island spacing at a fixed temperature has the same effect on the effective radii of an island as changing the temperature in an array with fixed island spacing. Evidence of this can be seen by comparing Figures 6.2 to 6.4.

Though magnetic frustration has been observed in many systems, we seem to observe clearer effects than many studies. Also, our results are unique in that we have also captured the spacing dependence of the transitions.

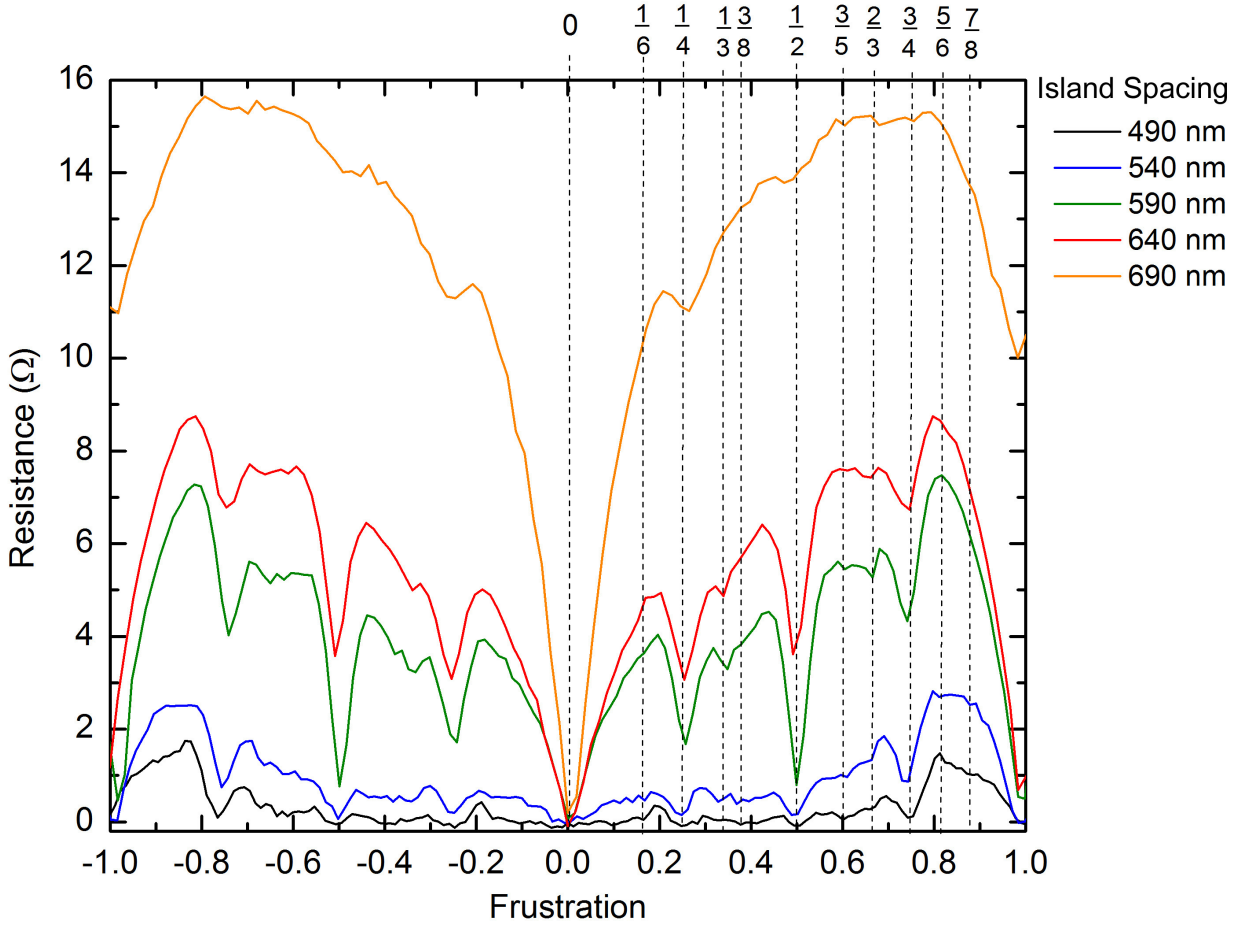

Figure 6.4: **Dependence of Magnetoresistance on Island Spacing**. Magnetoresistance at 30 mK in arrays with islands spacings d = 490 nm, 540 nm, 590 nm, 640 nm, and 690 nm.

6.1.1 Bardeen-Stephen Flux Flow

The magnetoresistance curves show evidence of Bardeen-Stephen flux flow for particular magnetic fields. Given that the energy barrier to vortex motion is highly dependent on the field, we certainly expect to

observe different regimes of behavior for different ranges of fields. (Specifically, in small fields, the energy barrier is lower than at $f = 0$ partially due to screening currents in the sample induced by the applied field).

Originally formulated to address how Abrikosov vortices [2] in type II films flow in an applied field, Bardeen-Stephen-like behavior has been seen in SIS junctions[25]. The Bardeen-Stephen theory considers how current-driven vortices flow under a viscous damping force as they traverse the sample. It is valid in the dirty limit. The resistance is proportional to the number $n(f)$ and mobility $\mu(f)$ of free vortices such that $R(f) \propto \Phi_0^2 n(f)\mu(f)$. Given that the number of field-induced vortices is $n(f) = \frac{BA}{\Phi_0 N}$ (N is the number of plaquettes), we retrieve the Bardeen-Stephen result $R(f) \propto N\Phi_0 R_n \propto BR_n \propto An(f)$. Simply put, the magnetoresistance is expected to be linear.

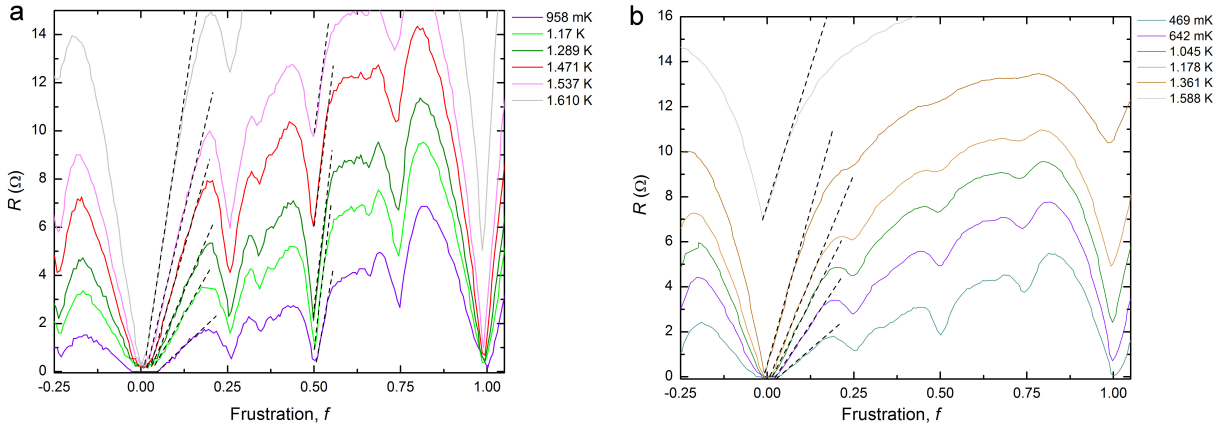

Figure 6.5: **Evidence of Bardeen-Stephens Flux Flow**. Temperature-dependent magnetoresistance for (**a**) 290-nm spaced islands and (**b**) 340-nm spaced islands. The dotted lines are linear fits within (**a,b**) $0 < f \leq 0.1$ and (**b**) $0.5 < f < 0.55$. Linear magnetoresistance is expected in Bardeen-Stephen flux flow.

We observe Bardeen-Stephen linear flux flow under the influence of low ($0 < f < 0.1$) and moderate ($\frac{1}{2} < f < 0.6$) magnetic fields and temperatures less than T_2. At higher temperatures, we see the expected increase in mobility, signified by an increase in the slope of the magnetoresistance. Above T_2, the magnetoresistance becomes rounded due to thermal fluctuations. Figure 6.5 shows the magentoresistance for the arrays with (**a**) 290-nm and (**b**) 340-nm island spacings. Regions of linear magnetoresistance are evident; the dotted lines are linear guides to the eye. At higher temperatures, the progressive rounding of magnetoresistance can be observed.

Only a select set of results are shown for clarity. Figure 6.6a is a plot of the extracted slopes of the magnetoresistance for $0 < f < 0.1$ at many different temperatures for six arrays. Though the slopes appears to increase exponentially with normalized temperature, the mobility seems to increase at different rates in

[2] In unpatterned, type II superconducting films, when the applied field is high enough to penetrate the sample, an array of so-called Abrikosov vortices naturally form.

some arrays. Note that the arrays with island spacings of 290 nm and 640 nm exhibit similar behavior, and as do the arrays with 490-nm and 540-nm spaced islands. Strangely enough, the 340-nm spaced islands seems to crossover between the faster rate of increase of the former devices to the slower rate of the latter arrays. Also, note that the device with 290 nm spaced islands is on a different sample than the one with 640 nm spacing. So, no obvious correlation exists between the sets that exhibit similar behavior. In Josephson junction arrays, the mobility[25] is expected to approximately follow the form $\mu(T) \propto (\frac{R_n A}{\Phi_0^2})e^{-E_B/(k_B T)}$. Figure 6.6b is a fit of this relation to the data for two different arrays. The trend seems to fit the data fairly well, but the proper method of performing the fits requires using the reduced temperature $\tau = T/\frac{\hbar}{2e} i_c(T)$. We extracted $E_B \sim 6.8E_J$ and $0.7E_J$, however, these may not be accurate given that we did not use the reduced temperature τ. A more rigorous analysis is warranted.

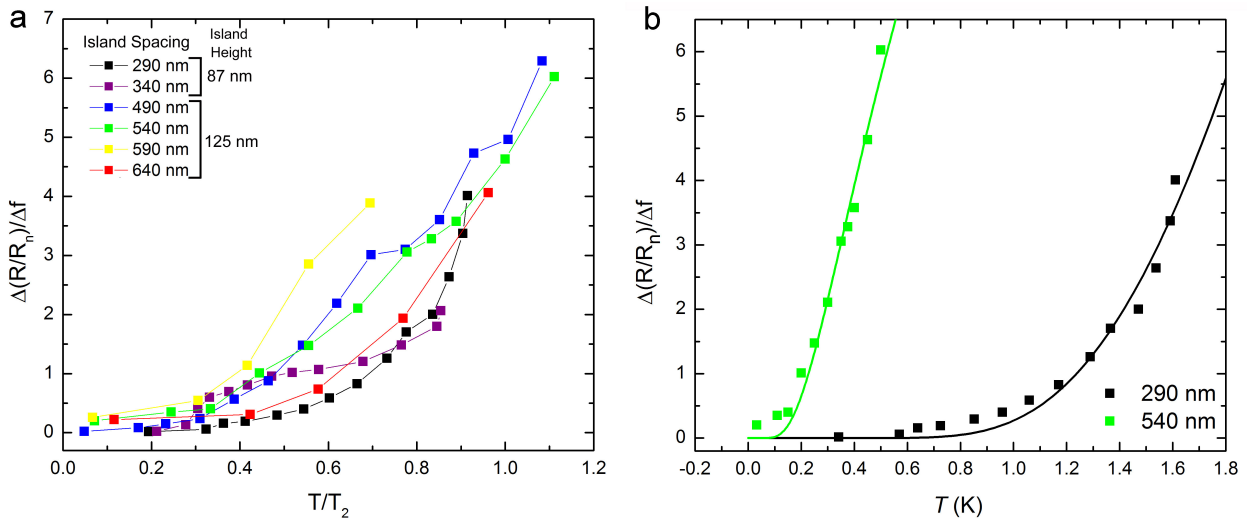

Figure 6.6: **Temperature Dependence of the Vortex Mobility in Arrays in a Magnetic Field**. According to the Bardeen-Stephens flux flow prediction, the vortex mobility follows the form $\mu(T) \sim \Delta(R/R_n)/\Delta f$. The mobility is plotted versus the normalized temperature for (**a**) arrays with spacings d = 240 – 640 nm, and (**b**) d = 290 and 540 nm. (**b**) The solid lines are fits of the extracted mobility, for the 290-nm spaced islands and 540-nm spaced islands. The fitting parameter E_{bv} is $6.8E_J$ and $0.7E_J$, respectively. However, a more rigorous analysis using the reduced temperature τ is warranted to make the free fitting parameters meaningful.

6.2 Two-step Transition to the Normal State

Section 6.1 focused on the effects of a low magnetic field ($f \leq 1$) on SNS arrays. This section will address the high field behavior. As previously mentioned, there has been limited research on effects in higher magnetic fields in which vortex-vortex interactions become significant. Competition between vortex-vortex

and vortex-lattice interactions is not well understood.

Magnetoresistance sweeps up to $B \approx 8$ T were taken on all arrays. Figures 6.7 (page 86) and 6.9 (page 88) show magnetoresistance curves in a single array with $d = 140$ nm, and five arrays with $d = 490$ – 690 nm, respectively. All devices undergo a two-step transition from a superconducting state [3] to the normal state value $R(10\text{ K})$. The low-field sudden rise to finite resistance, B_2, approximately corresponds to $f = 1$ and loss of superconductivity across the array. Presumably, the high-field step, B_1, results from loss of superconductivity in the individual islands.

As expected, at a fixed temperature, denser arrays have higher critical fields B_2. However, the transition from the knee above B_2 to B_1 becomes increasingly broad with an increase in d. This smearing of the second transition makes it impossible to distinctly identify B_1; we were unable to investigate the dependence of B_1 on island spacing.

Figure 6.7 is a plot of the magnetoresistance for a device with 140-nm spaced islands. Taken at 260 mK using an excitation current of 500 nA, the sweep rate was varied from 10 mT/min for low fields ($f < 1.5$) to 50 mT/min for moderate fields (up to 1 T), then 100 mT/min for high fields (up to 8 T). The field was swept both up and down; arrows denote the sweep direction. Clockwise hysteresis is clearly evident. It is likely due to intrinsic device properties rather than induced by the measurement technique. Hysteretic effects due to eddy currents from the sweep rate have been ruled out. If heating were the issue, the downward sweep would yield a lower B_2 than the upward sweep. Additionally, sweep rates of 5 mT/min up to 250 mT/min were tested for fields $B > 1$ T in numerous previous devices, and no differences were apparent. Furthermore, if the issue were simply trapped flux, the downward sweep would also be expected to have a suppressed critical field. The amount of hysteresis appears to decrease with an increase in island spacing.

Some research has attributed magnetoresistance hysteresis to glassiness[37,105,106]. In fact, one other observation of such hysteresis in 2D superconducting systems seen in the literature was by Mason *et al.* in disorderd amorphous MoGe films[105]. Deeming this the first observation of a vortex-glass phase in 2D superconductors, they attributed the observed hysteresis to a vortex-glass phase. Figure 6.8 is a plot of their results, which appear quite similar to ours. The mechanism behind this hysteresis is currently unresolved.

[3] Note that the seemingly flat, zero-resistance region may in fact be frustrated, with oscillations below our measurement sensitivity at 260 mK. See Section 6.1 for a discussion of and results showing magnetic frustration.

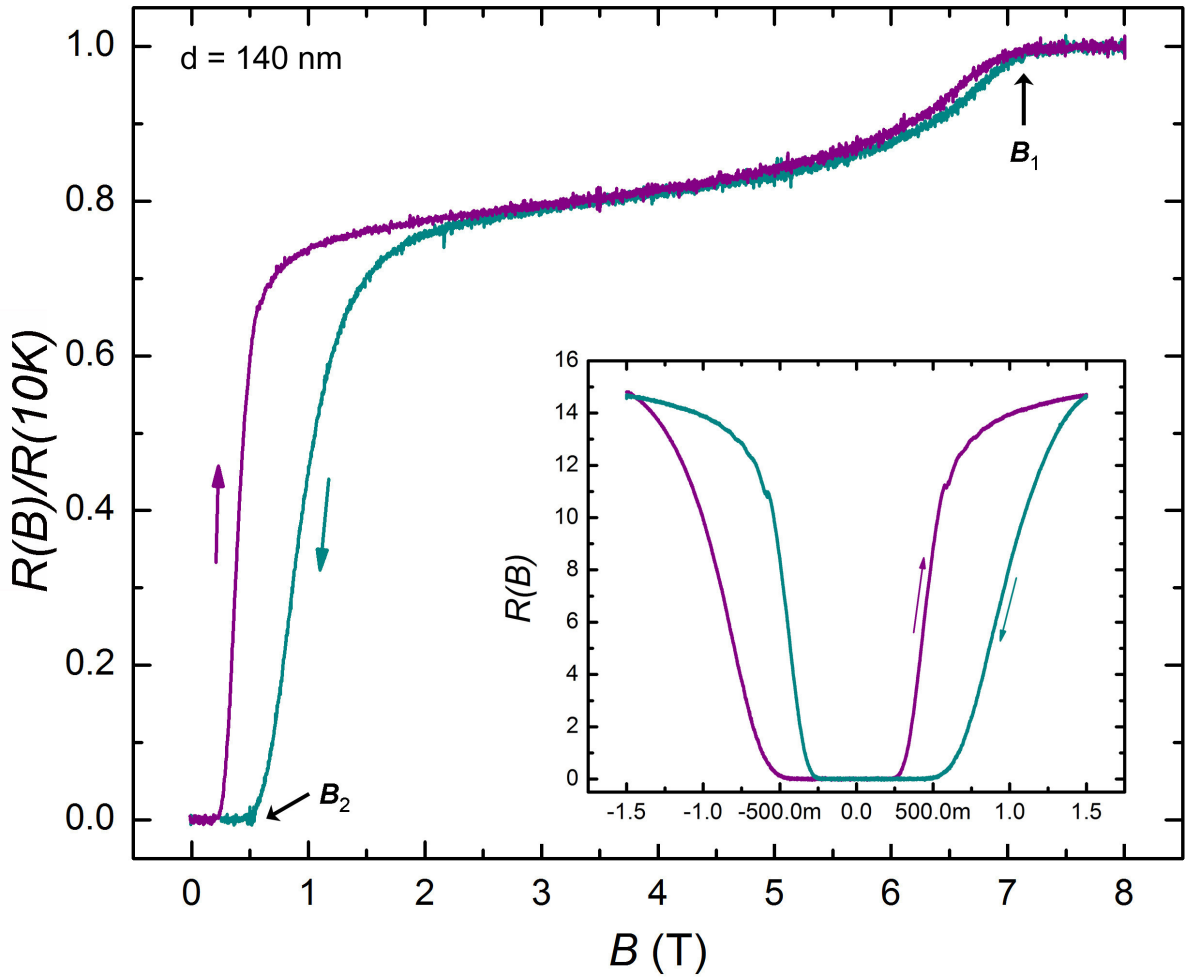

Figure 6.7: **Two-Step Transition and Magnetoresistance Hysteresis in a Swept Magnetic Field**. The resistance is plotted against a swept, perpendicular magnetic field for an array with $d = 140$ nm (sample **1**) at 260 mK. The arrows indicate the sweep direction. The magnetic field is swept at 10 mT/min for fields 0 to 1 T, then at 100 mT/min up until 8 T. An excitation current of 500 nA was used. The **inset** shows a zoomed-in view of the clockwise hysteresis loop, symmetric about $B = 0$.

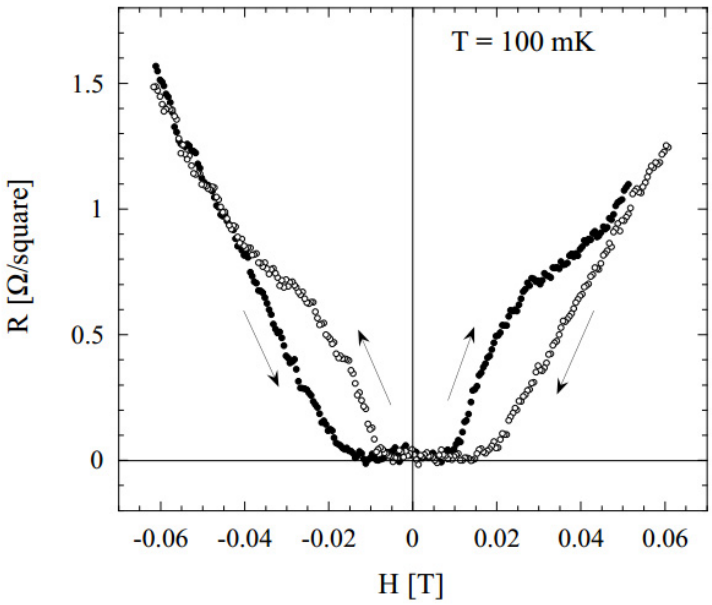

Figure 6.8: **Magnetoresistance Hysteresis in MoGe Films**. Magnetoresistance sweep at $T = 80$ mK of 40 Å film of $Mo_{43}Ge_{57}$ sandwiched between insulating layers of amorphous Ge on SiN substrates. The critical field observed here is significantly less than the field at which the film becomes insulating. The authors attribute this clockwise hysteresis to either a low field first order phase transition to a superconducting state or a vortex-glass (a low density of vortices are frozen). Image extracted from Mason *et al.*[105]

An understanding of hysteresis in SNS arrays could help elucidate the origin of magnetoresistance hysteresis in high temperature superconductors. Whether it is caused by pinning of Abrikosov vortices in the superconducting grains or by inter-granular weak-links[107,108] remains under debate. Our data, however, implies that it is related to the latter. Further, some high-T_c cuprate-based superconductors also experience a two-step resistive transition in an applied magnetic field[109], similarly attributed to Josephson-coupled grains becoming superconducting before the grains phase-lock and superconductivity persists across the film.

Figure 6.9 shows the results of magnetoresistance measurements up to 8 T in arrays with spacings $d = 490$ – 690 nm. B_2 shows a clear suppression with an increase in d, while B_1 appears to saturate. This saturation is unexpected; the island transition temperatures T_1 are distinctly different in all arrays. Assuming that B_1 is indeed related to the critical field of the individual islands, we would subsequently expect different values of B_1.

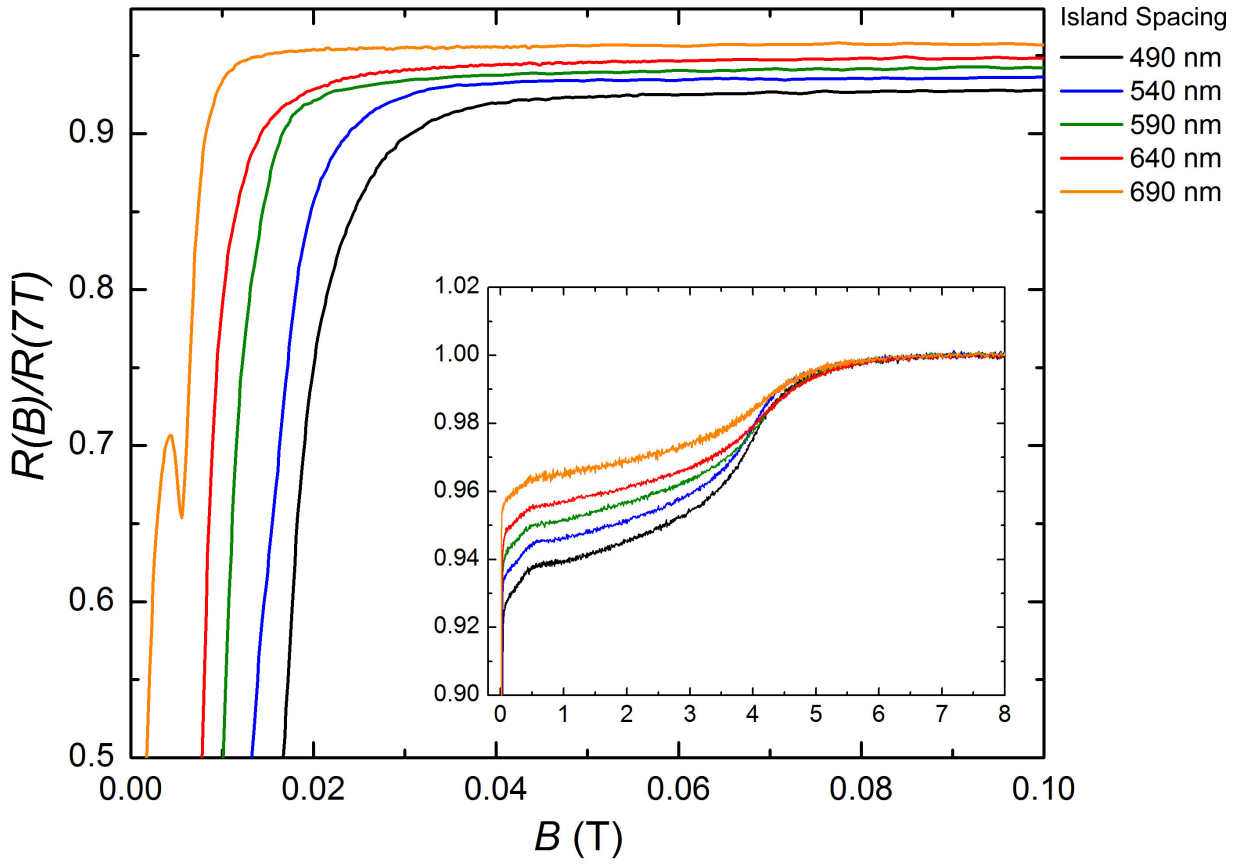

Figure 6.9: **Comparison of High-Field Transitions in Arrays with $d = 490 - 690$ nm**. The **main panel** shows a systematic suppression in the critical field with an increase in d. The field was swept at 1 mT/min for $f < 1.5$, then at 10 mT/min up to 1 T, and 100 mT/min up to 8 T. The **inset** shows the full sweep from 0 to 8 T. The value of the high-field step is approximately independent of d. (Sample **4**)

6.2.1 Crossing Point in Magnetoresistance Isotherms

Figure 6.10 shows magnetoresistance at multiple temperatures for an array with 440-nm spaced islands. The curves all cross at the same point. Traditionally, the appearance of a temperature-independent crossing point of magnetoresistance isotherms in the SIT picture indicates adherence to scaling theories [27,105]. The scaling exponent can determine whether such systems experiences a quantum critical point or percolation. Testing scaling theories may provide enlightening results on the high field behavior. Further studies and a more detailed analysis is warranted.

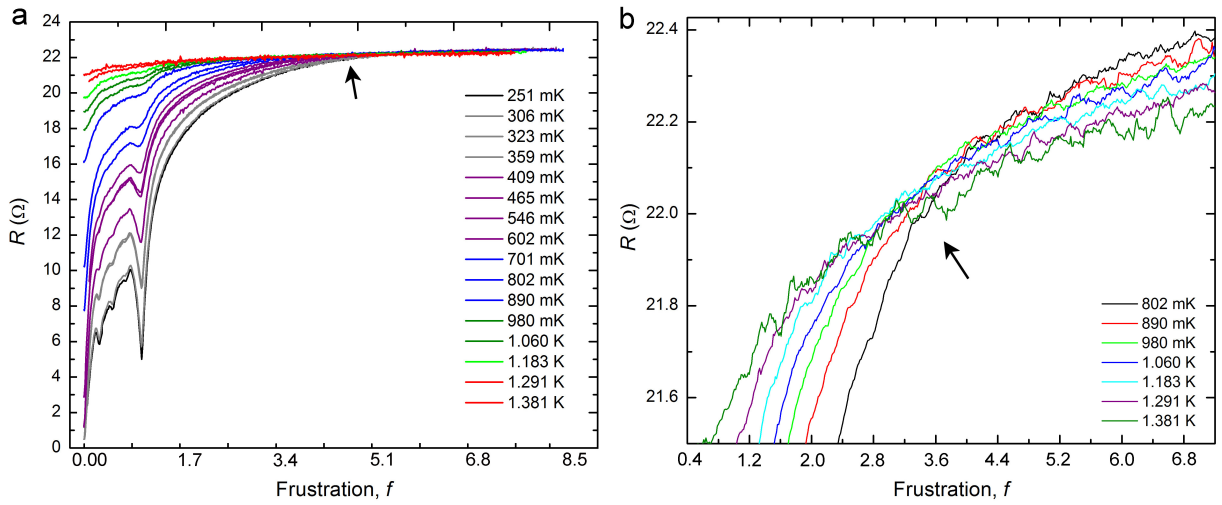

Figure 6.10: **Crossing Point in the Magnetoresistance Isotherms**. Resistance is plotted versus frustration in arrays with $d = 440$ nm and $z \approx 50$ nm (**a**) at different temperatures $T = 251$ mK – 1.381 K, and (**b**) at temperatures $T = 802$ mK – 1.381 K. In (**b**) the curves have been re-colored for clarity and the range of the displayed data has been reduced. The curves all cross around $f \approx 3.6$. The arrow marks the crossing point in both (**a**) and (**b**).

6.3 Smoothly Varying Resistance versus Temperature in a Magnetic Field

Temperature sweeps in a magnetic field could reveal the effects of thermal energy on field-induced vortices. Figure 6.11a shows the resistance versus temperature in multiple magnetic fields for the arrays with 125-nm tall islands and 490 nm spacing. An excitation current of 500 nA was used; lower excitation currents produced unreproducible features due to the amount of noise coupled in during these long temperature sweeps [4].

[4] We later figured out how to reduce the noise and better times of the day to take long, sensitive measurements, allowing us to use lower excitation currents in future measurements.

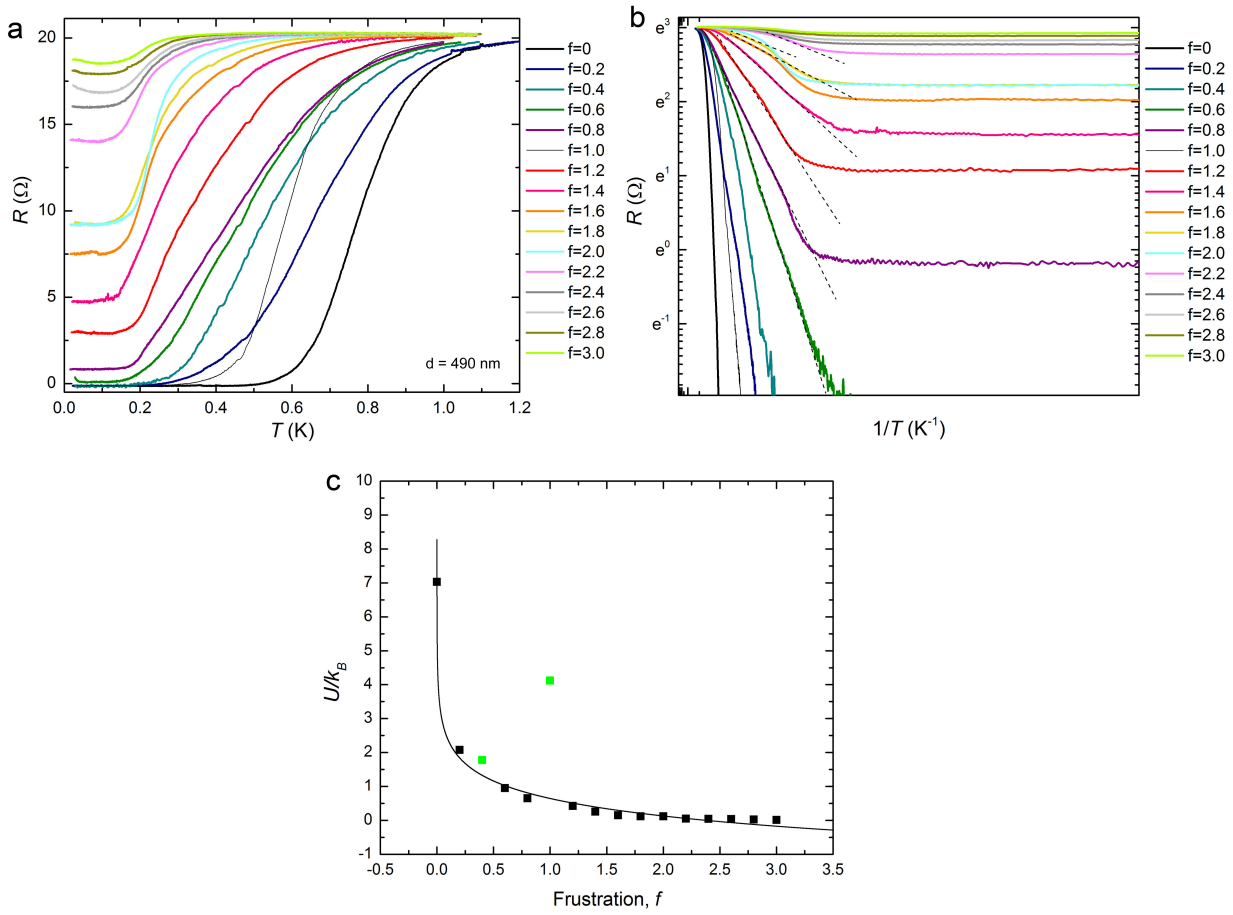

Figure 6.11: **Thermally Activated Motion of Field-Induced Vortices in Array with $d = 490$ nm.** (**a,b**) Resistance versus Temperature Sweep in Different Magnetic Fields. Most curves show a temperature-independent finite resistance at low temperatures due to flux flow of weakly pinned, field-induced vortices. The upturns with a decrease in T for $f = 2.6$, 2.8, and 3.0 are not understood. (**b**) The dashed lines show linear fits to $\ln R$ vs. $1/T$ within the thermally activated flux flow regime. The extracted slopes yield the activation energy U plotted versus the frustration in (**c**). (The measurements were taken on sample **4**.)

The most striking feature of the data is the flattening of resistance at finite values at low temperatures and broadening of the transitions with an increase in field. Broadened transitions in a field are typically caused by the thermally activated motion of initially pinned vortices, possibly signifying a collective creep regime[27]. We have analyzed the data to show that this is reasonable. Flattened low-temperature resistive tails are indicative of a metallic regime. We believe this regime is caused by resistance from flux flow of weakly pinned vortices.

In fields $f > 1$, there is more than one vortex per plaquette and vortex-vortex interactions begin to play a significant role. Appreciable vortex-vortex interactions increase the likelihood of collective vortex behavior. To date, high field behavior is not well understood. Whether multiple vortices are positioned

within a plaquette or extra vortices are positioned on the edge of plaquettes is not completely clear. Perhaps these results are best understood by considering two populations of field-induced vortices. Single vortices pinned in center of each plaquette would be considered stable, requiring high energy to depin. The second population consists of vortices unable to sit in the minimum energy state of the egg crate potential. Such vortices are easily depinned by either a finite excitation current or finite thermal energy. It is likely this fixed population of field-induced free vortices are mobile up until a critical temperature. At this critical value, both populations become thermally-activated and the resistance rises as the system transitions to a normal state.

Thermally-activated vortex motion induces an exponential increase in the resistance $R \propto R_N e^{-U(B)/(k_B T)}$. Figure 6.11b depicts how the activation energies $U(B)$ were extracted through linear fits to plots of $\ln R$ vs. $\frac{1}{T}$. In the collective creep regime, the field-dependence of the activation energy follows the relation

$$U(H) = U_0 \ln(\frac{H_0}{H}), \tag{6.4}$$

where H_0 is on the order of the critical field[110]. Extracted activation energies are plotted against their respective fields f in Figure 6.11c. The solid line is a fit to Eq. 6.4, with $U_0 = 0.744 k_B$ and $H_0 \sim f_0 = 2.381$. Both $f = \frac{2}{5}$ and $f = 1$ were excluded, as a significant population of vortices are strongly pinned at these fields. The data seems to fit the expected collective creep dependence fairly well, though a more rigorous analysis is warranted.

A flattening of resistance at low temperatures is also seen at low fields $f < 1$ for non-rational values of frustration. This observation is consistent with the above picture — a population of vortices determined by the nearest rational value of frustration (less than the actual value) remains pinned, while the additional vortices undergo flux flow. At rational values of f, T_2 is field-dependent. The fractional shift in T_2 with field would equal the fractional shift in ground-state energy as the field is varied. The barrier to vortex motion is high at $f = 0$ and $f = 1$. These curves appear similar in shape, with a shifted T_2. The $f = \frac{1}{2}$ (not shown) and $f = 1$ states may exhibit BKT-like transitions.

A better understanding of these results would come from directly observing vortex dynamics in our devices. Scanning probe microscopy techniques have been used to create videos of vortex dynamics in unpatterned superconducting thin films and films with arrays of holes or magnetic dots that act as pinning sites. Some of these techniques (e.g. magneto-optical Kerr effect microscopy, scanning SQUID microscopy) lack the appropriate spatial resolution needed to identify individual vortices in our arrays. Vortices in our arrays with the farthest spaced islands may approach the appropriate sizes or separations within the resolution of the aforementioned techniques. However, T_2 is extremely low in these arrays, requiring a

microscope to be mounted in a dilution cryostat. Unfortunately, such systems do not yet exist.

Scanning tunnelling microscopy (STM) holds the most promise for probing vortex dynamics in our devices, as it can locally measure the density of states. Additionally, low-noise, low-temperature STMs do exist. To date, the aspect ratio of our islands makes it difficult to scan our arrays without crashing the tip into the side of the islands during a scan. This problem is not insurmountable; presently a research group is adjusting their system and we hope to scan our arrays in the near future.

6.4 Cusps in Resistance versus Temperature in a Magnetic Field

Section 6.3 presented an analysis of thermally activated field-induced vortices for sample **4**. At low temperatures, the resistance is temperature-independent and either zero or finite. At a critical value the temperature smoothly increased up to the normal state value. The transition to the normal state was broader for higher fields. Though these trends were reproducible for most samples, a couple samples exhibited striking behavior. Results from these samples are presented in this section.

Figures 6.12 and 6.13 show sets of resistance versus temperature sweeps for an array with 440-nm and 540-nm spaced islands, each plot showing the results for a different field. (Because for $f < 1$ the transitions to the normal state did not systematically broaden with an increase in field, the curves could not be clearly displayed on a single plot). These measurements were taken on sample **3**. Sweeping the temperature up results in a series of sudden increase in resistance that flatten out before suddenly increasing again. Each cusp fits well to a general Arrhenius form $R \propto R_0 e^{E_0/(k_B T)}$, though whether the coefficients are meaningful has not been determined. Furthermore, the trend in the positions and numbers of the cusps for each f has yet to be determined. To our knowledge, this behavior has never been observed in superconducting devices.

Cusps were also observed in a device with 640-nm spaced islands on the same sample, and devices with island spacings of 290 nm and 340 nm on a different sample. Finite field thermal activation in the aforementioned sample could not be thoroughly investigated because T_2 was too high to observe more than one cusps in the accessible temperature range of the ^{3}He fridge.

A possible explanation for these cusps is collective, sudden depinning of different populations of field induced vortices. Some populations are more strongly bound to the vortex lattice than the other. Perhaps as the thermal energy becomes high enough for a particular population of pinned vortices to surmount U_B, we see a cusps.

To explore the reason some samples exhibit cusps-like behavior and some smooth behavior, we scrutinized the differences in the measurement scheme and in the intrinsic properties of the samples. The islands in the

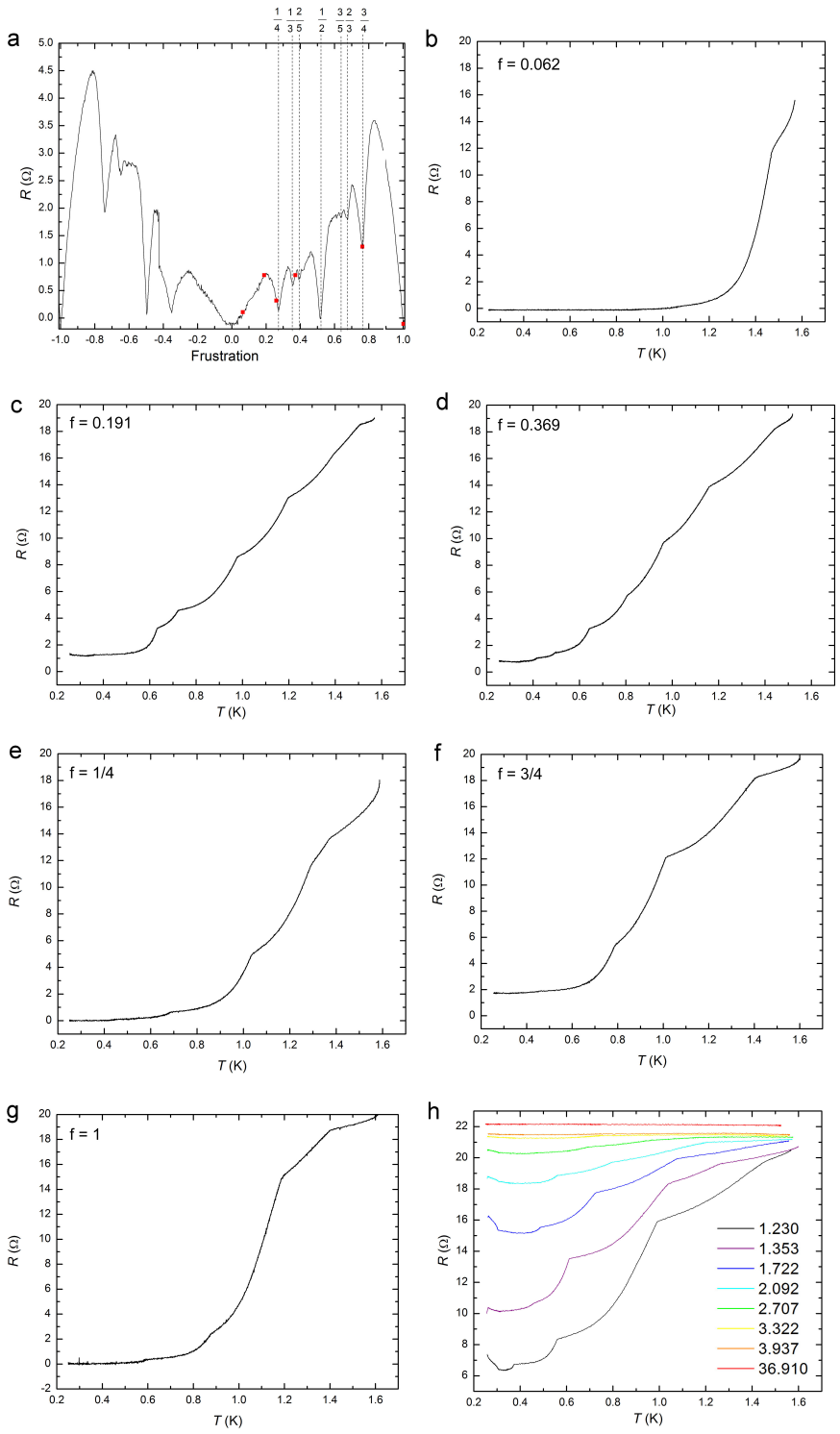

Figure 6.12: **Cusps in Resistance versus Temperature in a Magnetic Field in Arrays with d = 440 nm**. Magnetoresistance oscillations at $T = 495$ mK are plotted in (**a**) for perspective sake. The red dots correspond to the values of frustration at which the temperature sweeps are measured in (**b,c,d,e,f,g**). Resistance versus temperature curves for non-rational values of frustration (**b**) $f = 0.062$, (**c**) $f = 0.191$, and (**d**) $f = 0.369$ and rational values of frustration (**e**) $f = \frac{1}{4}$, (**f**) $f = \frac{3}{4}$, and (**g**) $f = 1$. (**h**) Temperature-dependent resistance curves for multiple values of $f > 1$. (This data was taken on Sample **3**).

samples that did not display cusps were about twice as tall as those that displayed cusps. Additionally, the sample that displayed cusps had significantly fewer islands than those that did not show cusp-like behavior. We have yet to retest a sample with the same island heights as sample **3**. Measurements on sample **3** were all taken in the ^{3}He cryostat, while all samples that displayed no cusps were mounted in the dilution cryostat. We investigated the possibility that sample **3** was accidentally field-cooled and the cusps were related to resulting trapped flux in the sample. This was not entirely unreasonable; trapped flux in the magnet during the initial fridge cool-down and setting an improper offset field during re-condensation could result in cooling the sample at fields of ~ 0.1 mT – 6.6 mT. However, cooling in such small fields appeared to have no measurable affect on zero-field R vs. T measurements nor IV characteristics. Attempts at cooling in high fields (6 – 8 T) before taking temperature sweeps in a small field failed to reproduce the cusps.

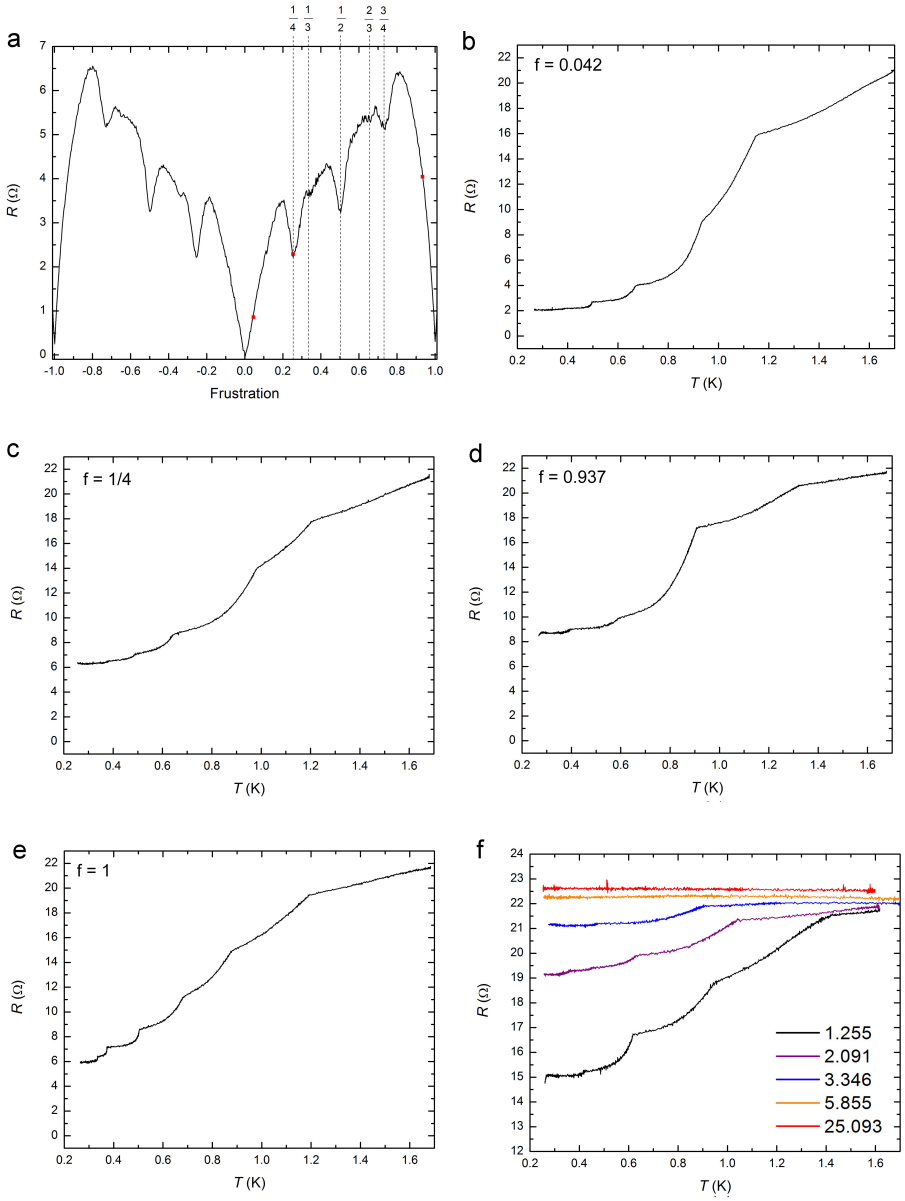

Figure 6.13: **Cusps in Resistance versus Temperature in a Magnetic Field in Arrays with d = 540 nm**. (**a**) Magnetoresistance oscillations at $T = 263$ mK are plotted for perspective sake. Resistance versus temperature curves for non-rational values of frustration (**b**) $f = 0.042$ and (**d**) $f = 0.937$, and rational values of frustration (**c**) $f = \frac{1}{4}$ and (**e**) $f = 1$. (**f**) Temperature-dependent resistance curves for multiple values of $f > 1$. (This data was taken on Sample **3**).

6.5 Effects of an Applied Current on Field-Induced Vortices

In Section 5.4, we discussed the effect of a current on bound vortex pairs in non-zero field. Thermally-induced vortices will suddenly depin from the lattice when the current-induced Lorentz force is high enough for vortices to overcome the egg crate potential lattice. This results in a U-shaped differential resistance ($R_d \equiv \frac{dV}{dI}$) plot, with a flat region below I_c, sharp peak rising above R_N at I_c, then drop down R_N and Ohmic behavior. In this section, we will discuss the effects of a current on field-induced vortices. The magnetic field not only tunes the number of vortices, but also the pinning strength of these vortices to the lattice due to magnetic frustration. Some of these vortices will be better coupled than others. Because of this, all vortices do not suddenly depin at a single critical current, and the current-biased differential resistance in non-zero field has a far richer structure than in the zero-field case (shown on page 63).

Figure 6.14 shows the differential resistance under a current bias for four different frustrations. All measurements were taken at 257 mK using a Keithley 6221 AC/DC current source and 2182a nanovoltmeter. The current was swept from negative to positive using a DC sweep. The different regimes of vortex flow will be discussed below.

I. Vortex Depinning Current

First of all, for even the lowest of fields, the curves exhibit a small cusp for very small, finite currents. The current at which $\frac{dV}{dI}$ is no longer zero is called the depinning current, i_d. Vortex depinning occurs when the applied current is high enough for a vortex to overcome U_B, the position-dependent energy barrier for vortex motion. It is the minimum current required to depin a single vortex, so will depend on the most weakly bound vortices. So, in the most strongly bound configurations, there may be little-to-no noticeable low-current cusps.

There are no such low-current features in the zero-field differential resistance curves in Section 5.4, such as Figure 5.6 on page 63. For small fields $f \ll \frac{1}{2}$ and low temperatures $T \ll T_2$, vortex-vortex interactions are insignificant when compared to that between individual vortices and the egg crate lattice. Also, the vortex pinning energy is smaller than the energy scale of the BKT transition[111]. So, individual field-induced vortices can easily depin at temperatures $T \ll T_2$. This is clearly evident in Figure 6.14, as the blue curve exhibits a distinct depinning current despite the field being extremely low, $f = 0.005$. In a square array, the depinning current is expected to be $0.1I_c$. This has been experimentally verified in square arrays of Al-AlO_x junctions, and found to be higher than in triangular arrays of the same material[112]. This is not surprising given that the energy barrier E_B is much higher in square arrays than in triangular ones.

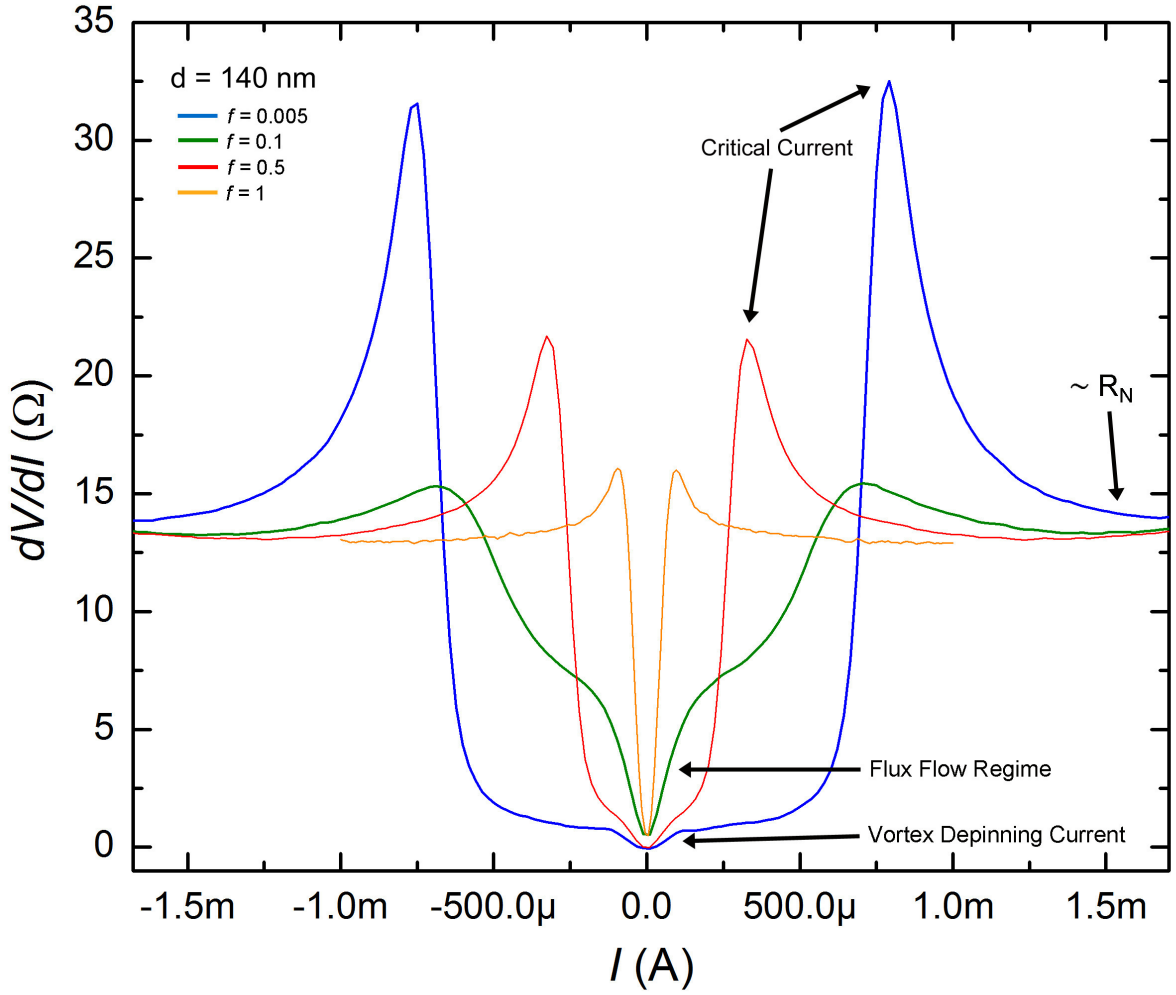

Figure 6.14: **Current-biased Differential Resistance in a Magnetic Field** . The data was taken on an array with island spacing $d = 140$ nm and height $d = 87$ nm. Each curve was taken in a different magnetic field, specified by the frustration f in the legend. The vortex depinning, flux flow regime, and critical currents are labelled. The $R_d \equiv \frac{dV}{dI} \approx R_N$, where R_N is the normal resistance, for high currents.

II. Flux Flow Regime

Above the depinning current, damping will play a significant role in determining vortex motion. In overdamped arrays such as ours, vortices move as massless particles. Moving vortices will cause a voltage drop across the width of the sample ($\hat{y}$ direction) causing time-dependent phase differences. This voltage drop satisfies the Josephson relation Eq. 1.6, with a voltage proportional to the number of vortices (field- and thermally generated), and induces dissipative currents in the Au. This creates a viscous force on a vortex $F_{dv} = -\eta(T,B)v_v$, where the vortex velocity is v_v and drag[113] is $\eta \propto \frac{3}{2}(\frac{\Phi_0}{a})^2\frac{1}{2R_N}$. The actual drag will depend on the position of the vortex. In this region, the array will experience Ohmic behavior and the differential resistance is the effective damping resistance in the array[112]. The slope is expected to be field-independent, though the actual resistances will be proportional to the density of freely flowly vortices, which rises as we continue to reduce the barrier by increasing the current. In Figure 6.14, the flux flow regime is very distinct in the data taken at $f = 0.1$, where $\frac{dV}{dI}$ becomes linear immediately after weakly bound vortices depin.

III. Critical Current

As the current is further increased, the Lorentz force eventually surpasses the pinning force. This is the point at which the energy barrier to vortex motion becomes zero and the vortex lattice completely depins from the egg crate potential. The peak in the differential resistance marks the critical current of the array, then the differential resistance falls to its normal state value. The slope of the differential resistance due to depinning of the vortex lattice varies substantially depending on the magnetic field. The exact behavior depends on the number of vortices, the pinning energy, and the specifics the vortex lattice rearrangements. We are currently attempting to simulate this behavior.

IV. Multiple Peaks in the Differential Resistance

In our arrays, we observe four large peaks in the differential resistance, that is, two peaks for $I > 0$. The low current peak marks the critical current of the array and we presume that the high current peak marks that in the individual islands. Nb has a fairly high critical current density, so we are unable to sweep to high enough currents to observe the second peak in most of our arrays due to Joule heating. We were, however, able to observe both peaks in our array with 90-nm spaced islands. The results are shown in Figure 6.15.

Figure 6.15a displays $R_d \equiv \frac{dV}{dI}$ for $B = 5$ mT, 15 mT, and 150 mT, and include the zero-field result for comparison. The differential resistances in the non-zero field cases exhibit a distinct depinning current, and the flux flow regime is clear in the data taken in $B = 100$ mT. Each curve exhibits two distinct peaks

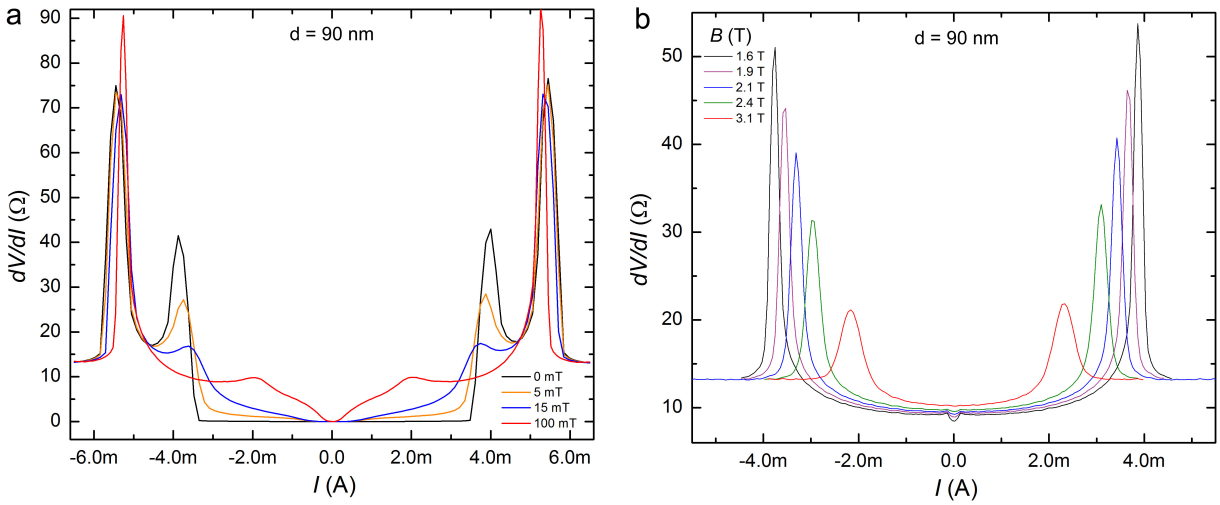

Figure 6.15: **Current-biased Differential Resistance in a Magnetic Field for an array with d = 90 nm**. Differential Resistance curves under a current-bias in different applied magnetic fields for an array with $d = 90$ nm, $z = 87$ nm at $T = 257$ mK (Sample **1**). (**a**) Two distinct peaks are evident in the differential resistance for $I > 0$. Each sweep is taken at low values of magnetic field ($f < 1$), $B = 0$, 5 mT, 15 mT, and 100 mT. The low current peak represents the critical current of the array (I_c), and the high current peak the critical current of the individual islands (I_{c1}). (**b**) Differential resistance at fields higher than the array critical field are shown. The arrays are no longer superconducting, but the remaining peaks are indicative of superconductivity in the individual Nb islands.

for $I > 0$. The adjacent plot, Figure 6.15b shows results for the same array, but at the significantly higher fields of B = 1.6 T, 1.9 T, 2.1 T, 2.4 T, and 3.1 T. These fields are high enough to suppress the array critical current peaks, yet the peak associated with the critical current of the individual islands remains. A dip in R_d that drops below R_N is evident between the negative and positive current peaks, so some type of superconducting correlation remain for $I < I_{c1}$.

6.5.1 Commensurate Fields

The peak in R_d is higher and narrower when the vortex lattices are strongly commensurate with the triangular lattice structure in our arrays. As we deduced from the magnetoresistance oscillations, the vortex superlattice is most strongly coupled to the egg crate potential for frustrations $f = \frac{1}{4}, \frac{1}{2}, \frac{3}{4}$, and 1. Of these commensurate fields, the vortex configuration is most stable at $f = \frac{1}{2}$ and 1.

In the array with 90-nm spaced islands, we can see from Figure 6.14 that the peak in R_d at $f = 0.1$ is lower than that at $f = \frac{1}{2}$, and wider than both $f = \frac{1}{2}$ and 1. This is also clear in the 140-nm spaced islands, results of which are in Figure 6.16a. In this array, R_d is highly sensitive to frustration; very low frustrations $f < 0.1$ quickly suppress the peak height and position. There is also a clear depinning current at extremely low currents, and the linear flux flow regime for $f = 0.051$, 0.102, 0.154. Furthermore, it is quite evident

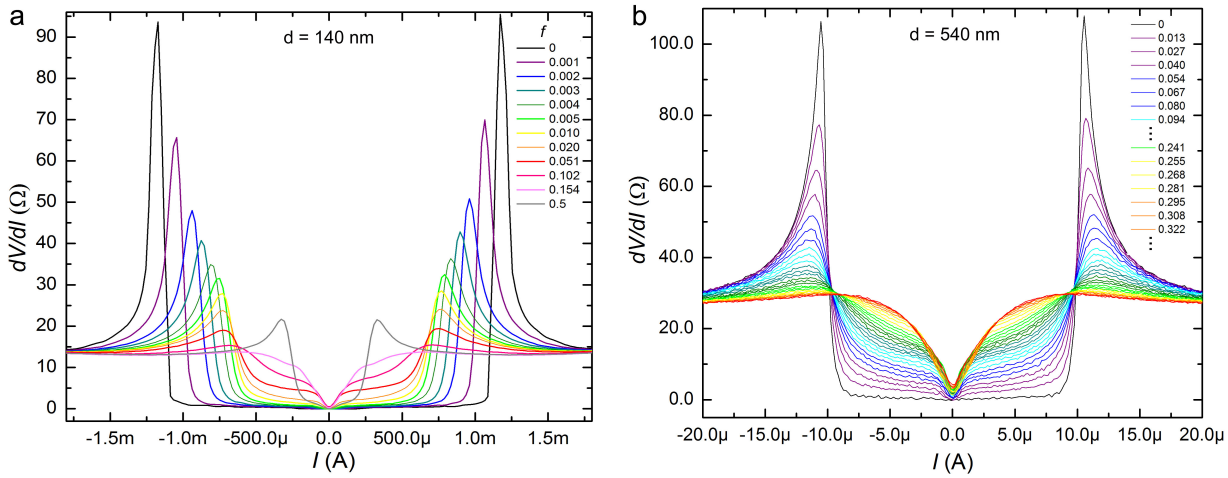

Figure 6.16: **Current-biased Differential Resistance in a Magnetic Field: Sensitivity of Critical Current**. Differential Resistance curves under a current-bias in different applied magnetic fields for an array with (**a**) $d = 140$ nm $z = 87$ nm at $T = 257$ mK (Sample **1**) and (**b**) $d = 540$ nm at $T = 17$ mK (Sample **4**). (**a**) Each curve was taken very low values of frustration $f = 0.001 - 0.005$, at intervals of 0.001, then at $f = 0.01$, 0.02, 0.051, 0.102, 0.154, and $\frac{1}{2}$. (**b**) Each curve was taken at a different field, from $f = 0$ to $f = 0.362$, at intervals of $\Delta f \approx 0.13$.

here that, as predicted, the slope of R_d in the flux flow regime is field-independent. At $f = \frac{1}{2}$, the peak height rises above that of the significantly lower frustrations $f = 0.102$ and 0.051.

We can more easily observe the evolution of the peak in R_d through 3D plots or 2D contour maps. Figure 6.17 contains two contour plots for an array with $d = 540$ nm. The current and frustration are shown on the x- and y- axes, respectively, the color scale represents the differential resistance, and all measurements are taken at $T = 17$ mK. The color scale in Figure 6.17b is meant to isolate the behavior of R_d for values near and above R_N, so no data for $R_d \leq 10\ \Omega$ is shown (white region). Dark blue regions denote the flux flow regime. In the green region, the array is in the normal state. The red and yellow regions are peaks where R_d rises above R_N. In this array, we see strong peaks near $f = 0$, which progressively drop as $f \to \frac{1}{4}$, flatten out, and then reappear at $f = \frac{1}{2}$ and $f = 1$.

From studying the differential resistance, we should also be able to see evidence of magnetic frustration. At $R_d(I \approx 0)$ versus frustration, we should be able to re-create features from the magnetoresistance plots under a swept field presented in Section 6.1. To this end, Figure 6.17a isolates the lower values of R_d, cutting off all $R_d > 6\ \Omega$ (shown as the white region). Dips in R_d at rational values of frustration are evident, where the blue regions are the deeper dips. The deepest dips occurs at $f = 0$ and $f = 1$, next deepest at $f = \frac{1}{2}$, and third deepest at $f = \frac{1}{4}$. This is completely consistent with our resistance oscillations under a swept field.

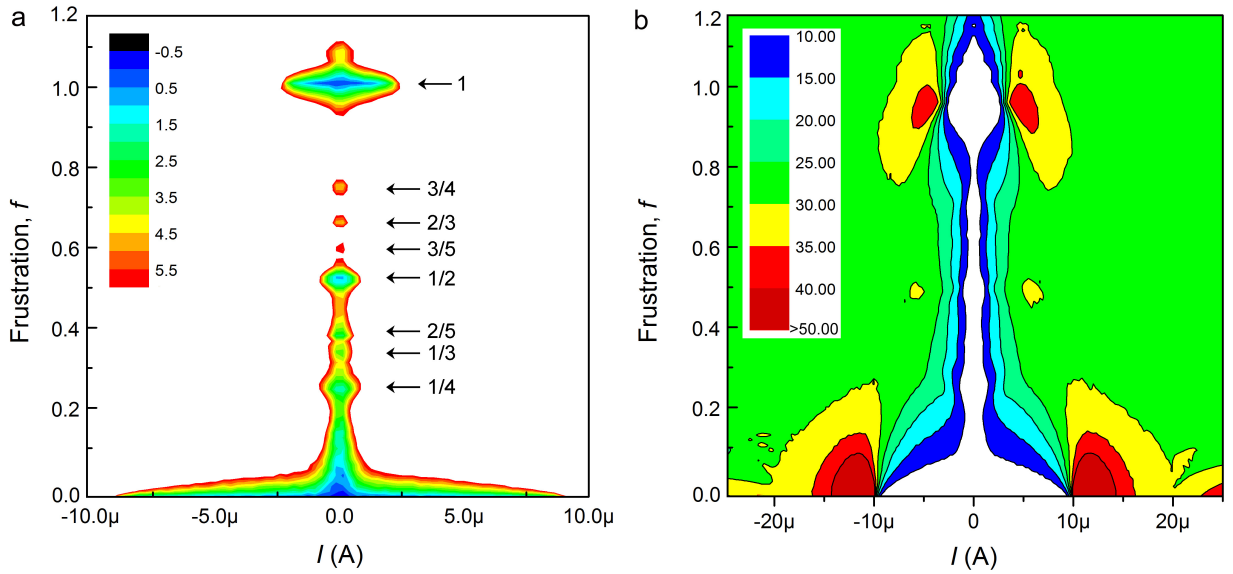

Figure 6.17: **Current-biased Differential Resistance in a Magnetic Field for an array with d = 540 nm: Evidence of Magnetic Frustration**. Differential Resistance curves under a current-bias in different applied magnetic fields for an array with $d = 540$ nm, $z = 125$ nm at $T = 17$ mK (Sample **4**). The color scale represents the differential resistance $R_d \equiv dV/dI$ (**a**) At certain rational values of frustration f, the differential resistance dips down as stable configurations of vortices become strongly pinned, consistent with magnetic frustration. This plot exclusively shows R_d values lower than 6 Ω, to isolate these regions. The critical values of f are labelled with black arrows. (**b**) This plot isolates the high values of R_d, cutting off all values lower than 10 Ω (white background). In the green regions, the array $R_d \approx R_N$. The red and yellow regions are peaks where R_d rises above R_N, clearly evident around $f \approx 0, \frac{1}{2}, 1$.

6.5.2 Incommensurate Fields

When the frustration is far from a commensurate value (by Δf), the barrier height for vortex motion is field dependent and vortex-vortex interactions might become important. The precise dynamics of vortices at incommensurate values is not rigorously understood. It is thought that the vortex lattice either forms a metastable vortex-glass state[114,115] or a quasi-ordered state[116]. In the latter case, the state would be an interpolation of nearest commensurate states, in which the main structure favors the lower commensurate configuration. This picture seems plausible for our arrays with $d = 490 - 640$ nm. Figure 6.18 shows our results for an array with $d = 540$ nm, taken at 50 mK. For the low field results, which are plotted in Figure 6.18a, the position of the peaks seem completely insensitive to field. Turning to the full results (Figure 6.18b), the dotted white line follows the peak position for $f = 0$ to $f = 0.5$; the peak position remains unchanged though the width of the peak clearly evolves. For $f \approx 0.5$ to $f \approx 0.9$, the peak is too low to accurately equate it with the critical current. At $f = 1$, the peak clearly reappears and is at a lower value than $I_c(f \leq 0.5)$. This would be consistent with two dominant pinned structures, with the extra field-induced vortices, determined by Δf, flowing as defects. However, nowhere in the literature have we

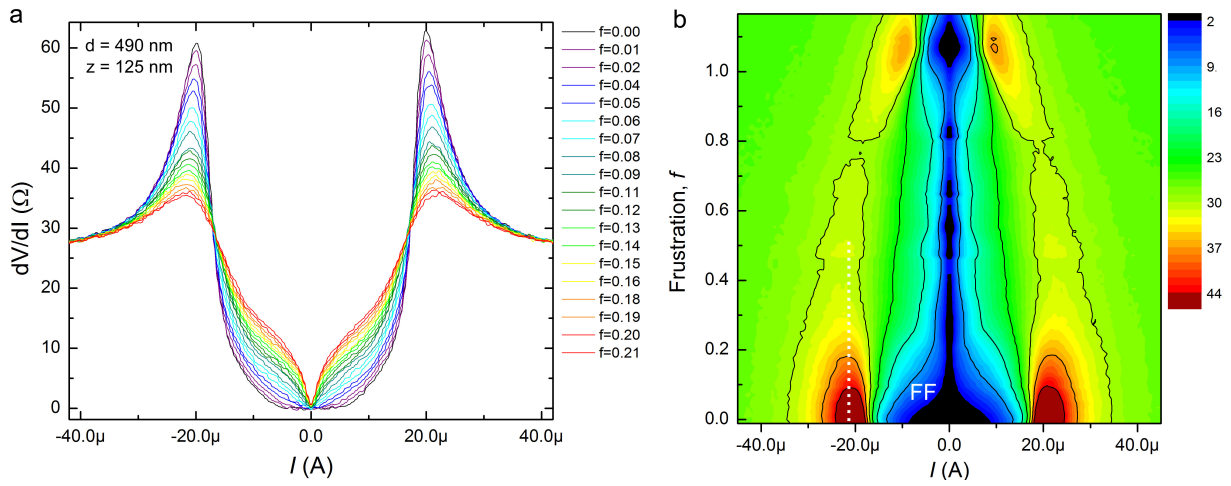

Figure 6.18: **Current-biased Differential Resistance in a Magnetic Field for an Array with $d =$ 490 nm**. Differential Resistance curves under a swept current in different applied magnetic fields for an array with $d = 490$ nm, $z =$ at $T = 50$ mK (Sample **4**). (**a**) Each curve shows the R_d at a different magnetic field, from $f = 0$ (black curve) to $f = 0.21$ (red curve) in intervals of $\Delta f \approx 0.01$. (**b**) The 2D contour plot shows R_d in fields from $f = 0$ to $f \approx 1.2$. The color scale represents the differential resistance. The white dotted line is the approximate position of the $I < 0$ peak for $f < \frac{1}{2}$. "FF" marks the flux flow regime, the blue region on the contour scale.

seen such insensitivity of I_c to field in Josephson junction arrays.

However, all of our arrays do not show such insensitivity in the critical current to the applied field. Figure 6.16 shows a comparison between R_d in (a) 140-nm spaced islands and (b) 540-nm spaced islands. In Figure 6.16b, we see a single peak position for fields ranging from $f = 0$ to $f = 0.362$. However, the array with 140-nm spaced islands shows a very clear, immediate suppression in the peak at very low fields of $f = 0.001$ to $f = 0.004$. The peak is then less sensitive for $f = 0.005 - 0.051$.

Shih and Stroud[104] used mean field theory to calculate the ground state energy E_g in a triangular array at a range frustrations. From Figure 6.3 on page 81, we can see that the ground state energy is symmetric around $f = \frac{1}{2}$. This symmetry should be reflected in the corresponding $I_c(T = 0, f)$. However, the insensitivity in the critical current to the field is inconsistent with this prediction.

Chapter 7

Conclusions

7.1 Summary of Results

We have studied superconducting transitions and vortex dynamics in triangular arrays of Nb islands on Au. Our research has focused on how these phenomena change with array geometry. The tunability of our devices -- including the ability to vary island geometry, spacing, material properties, and disorder – thus makes them excellent test-beds for exploring such transitions. To this end, we developed a nanofabrication procedure for arrays with island spacings ranging from 90 nm to 1.24 μm, and island heights 32 – 145 nm. This is the first systematic study of the dependence of superconducting transitions on island spacing and height in SNS arrays.

Arrays with islands spacings 90 – 690 nm undergo a two-step transition to a zero-resistance superconducting state upon cooling. The high-temperature drop in resistance marks the superconducting transition in the individual islands; the low-temperature drop to zero-resistance is a vortex-antivortex binding transition typical of 2D superconducting devices. Both transitions are suppressed with an increase in island spacing, and neither conforms to conventional theories for SNS arrays. The spacing dependence of the high-temperature drop was unexpected. We attribute this dependence to intra- and inter-island Josephson coupling. The trend in the lower temperature drop with an increase in island spacing appears to conform to models of a single, diffusive Josephson junction. Examination of our novel results led us to develop a phenomenological model capturing the spacing dependence of the transitions, and lack of saturation of the critical transition temperatures with an increase in spacing.

Dilute arrays show evidence of a 2D $T = 0$ metallic state, forbidden by Anderson localization. This spacing-dependent transition to an unconventional metallic state qualitatively resembles the predictions of

Spivak, but the specific dependence differs. Quantum tunnelling of vortices may characterize this state; this might be the first observation of vortex quantum tunnelling in SNS arrays.

To further understand these transitions, we have characterized vortex dynamics in these systems. All arrays exhibit magnetic frustration, which has been observed in numerous previous studies of regular arrays of Josephson junctions. A particular subset of fields show evidence of Bardeen-Stephen-like flux flow of vortices; magnetoresistance hysteresis may point to glassy behavior at particular fields. This hysteresis, as well as a two-stage transition in the magnetoresistance from $f = 1$ to the critical field of the individual islands resembles behavior commonly seen in high-temperature superconducting cuprates. Further examination of our finite-field data and extensions of our studies could shed light on vortex motion in high-temperature superconductors.

We have created an intrinsically phase separated system with "regional" phase correlations, i.e., correlations at length-scales larger than that of an island but not global in extent. The ability to stabilize regional correlations, in the absence of long-range ordering, is characteristic of a variety of inhomogeneous correlated systems, including high-temperature superconductors[117], coupled magnetic chains[118], and strained superconducting films[17]. The tunability of our system could thus help elucidate open questions in these materials.

7.2 Future Work

This research has created as many questions as it has answered. One of the best means of understanding the origin of the metallic state and better understanding vortex dynamics in these arrays would be through scanning tunnelling microscopy (STM). We are specifically interested in comparing tunnelling measurements on our arrays at temperatures between T_1 and T_2 to data for and predictions regarding the pseudogap in high-temperature superconductors. Collaborations with outside groups specializing in low-temperature STM have been established. The aspect ratio of our samples present a challenge; the groups are attempted to adjust their apparatuses appropriately.

Current-voltage characteristics in a field show a very low depinning current of weakly bound field-induced vortices. As the current is increased, the arrays experience a flux flow regime below the critical current before the vortices suddenly depin and the arrays transition to a normal state. In some arrays, the critical current is highly sensitive to fields; in others, it appears relatively insensitive. We will continue to model vortex dynamics in these arrays to better understand this behavior.

We have also started fabricating disordered arrays [(1)]. By systematically adding site disorder to the

[1]Malcolm Durkin is currently working on this project.

arrays, we can test percolation theories. We can also test the sensitivity of the BKT transition to disorder. Additionally, we would like compare our results to similar 1D systems by fabricating and studying 1D rows of islands.

In the superconductor-to-insulator transition picture, the sheet resistance of the film was a critical parameter in the transition in some devices. Given this, it is worthwhile for us to study how superconducting transitions in arrays may be affected by the resistance of the underlying normal metal. We will try non-magnetic, high resistance normal metals, such as bismuth or copper-nickel alloys.

We would like to further test predictions of 2D systems that may exhibit $T = 0$ metallic state, such as arrays of superconducting islands on graphene. To this end, we are currently fabricating and measuring arrays of superconducting Sn islands on graphene, specifically looking for a dissipation-tuned superconductor-insulator or superconductor-metal transition [(1)]. Such devices are in-situ tunable, as the carrier density of the graphene can easily be tuned by a back-gate.

Appendix A

Establishing a Clean S-N Interface

A dirty interface could hinder the diffusion of Cooper pairs from the superconductor to the normal metal. It could also cause a high capacitance, therefore charging energy, in the islands. An ideal interface is best established by depositing the normal metal, then subsequently depositing the superconductor without breaking vacuum. To this end, we began with Nb-Cr bilayers grown via molecular beam epitaxy by Dr. Tim McArdle in Professor James Eckstein′s research group. Though Cr is not ideal, as it shows antiferromagnetic ordering at room temperature and becomes paramagnetic above 38 °C, Nb and Cr have similar lattice constants and the bilayers have a clean and stable interface. We tried patterning arrays of islands of a masking material then using reactive ion etching to selectively etch the unmasked Nb, transferring the array pattern to Nb. We needed a mask material that would not easily sputter under reactive ion etching, nor easily diffuse into our superconductor. For mask materials, we tried both oxidized Al through positive electron-beam lithography and electron beam evaporation, and HSQ (spin-on glass) through negative electron-beam lithography. Additionally, we tried a range of reactive ion recipes involving SF_6 or CF_4 combined with O_2 gas.

Reactive ion etching is both a chemical and physical etching process. It is not as isotropic as ion milling and the directionality can be controlled by finding the optimal gas pressure and power. SF_6 does not generate a polymer to protect the sidewalls of the Nb islands formed during the process. This makes SF_6 suboptimal for etching thick layers of small Nb features, as it can undercut the islands over time. When using CF_4, a fluorocarbon film adheres to the sidewalls of the Nb islands, protecting these pillars from lateral etching. This film also progressively masks the device from further etching, therefore, using CF_4 typically requires high power to completely etch through the Nb layer. Higher power increases the physical versus chemical aspect of reactive ion etching, making it easy to quickly etch completely through the thin,

underlying Cr layer. Adding O_2 typically suppresses passivation of the sidewalls. Attempting a full range of power, gas pressures, and O_2 content, we were unable to come up with a reproducible RIE procedure that did not completely undercut the Nb islands, etch away the metal mask too quickly, or form a polymer mask across the sample before the unmasked Nb was completely etched away.

After abandoning RIE, we tried a similar fabrication procedure using ion milling on various superconductor-normal metal combinations (Nb-Cr, Nb-Cu, Al-Cu, Al-Au). It was impossible to insure that the underlying metal would not either quickly (within seconds) etch away once the superconductor was completely etched, or that a thin layer of superconductor would remain between the islands. Given that superconductivity could persist in very thin layers of superconducting material, incomplete etching of the superconducting layer could complicate analysis of our results. This could not be excluded in any fabrication procedure that starts with a bilayer and uses reactive ion etching or ion milling. Given that the alternative fabrication procedures involve breaking vacuum in between normal metal and superconductor deposition, the next best method of establishing a clean interface is to be able to mill a thin layer of the surface of the metal immediately prior to superconductor deposition.

Appendix B

Fabrication Procedure for Nb-Au Arrays

In Sections 2.2 and 2.1, we summarized the procedures used to fabricate the samples reported in this thesis. We developed this fabrication procedure from scratch, and list the detailed recipe here.

1. Cut substrates into 5 mm × 5 mm squares using diamond scribe or dicing saw

   We used undoped (100) silicon wafers (Si resistivity > 80 Ω-cm) with a 500 nm surface oxide layer

2. Clean substrates

   (a) Sonicate in acetone for 40 min.

   (b) Sonicate in isopropyl alcohol (IPA) for 30 min.

   (c) Rinse with ethanol to remove solvent residue.

   (d) Dry with N_2 gun.

3. Photolithography

   (a) Dehydration bake at 115 °C for 5 min.

   (b) Spin on AZ 5214E photoresist at 5000 rpm for 40 s.

   (c) Softbake at 95 °C for 60 s.

   (d) Expose in UV mask aligner with sample underneath a four-point pattern mask for ∼10 – 15 s.

   (e) Develop in 1:3 AZ 351:DI Water for ∼25 s.

   (f) Stop development by soaking in DI Water for 1 min.

4. Au Deposition using electron beam evaporation

   We deposited 99.999% *purity Au from ESPI in an ultra-high vacuum system at a base pressure of* 3×10^{-10} – 2×10^{-9} *torr*

   (a) Expose to UV/Ozone lamp (removes resist residue) for 3 min.

   (b) Evaporate 4 Å – 1 nm Ti sticking layer at 1 Å/s.

   (c) Evaporate 10 nm Au at 1 Å/s.

   (d) Lift-off in acetone.

5. Electron Beam Lithography

   We used a 3 layer scheme with lower molecular weight underlayers to create a slight undercut for easy lift-off

   (a) Spin on 495K A2 PMMA at 6000 rpm for 40 s.

   (b) Bake at 180 °C for 2 min.

   (c) Spin on 495K A2 PMMA at 6000 rpm for 40 s.

   (d) Bake at 180 °C for 30 min.

   (e) Spin on 950K A2 PMMA at 6000 rpm for 40 s.

   (f) Bake at 180 °C for 30 min.

   (g) Write array of islands using RAITH 150 e_Line.

      i. EHT = 30 kV

      ii. Aperature = 7.5 μm

      iii. Writefield = 200 μm

   (h) Develop in 1:3 MIBK:IPA for 90 s

   (i) Stop development by soaking in IPA for 1 min.

6. Nb Deposition using electron beam evaporation

   We deposited 99.95% *purity Nb from Alfa Aesar in an ultra-high vacuum system at a base pressure of* $3 - 9 \times 10^{-10}$ *torr*

   (a) Expose to UV/Ozone lamp for 3 min.

   (b) Ion mill sample for 25 s.

   (c) Electron-beam evaporate 20 – 150 nm Nb at 1 Å/s.

(d) Lift-off in acetone.

7. Wirebond

   (a) Mount sample to chip carrier using silver paint.

   (b) Connect Al wirebonds to contact pads using a wedge bonder.

B.1 Resistivity and Number of Islands in Each Array

The table below a follow-up to Table 2.1 on page 30. The resistivity (column 4) was used to calculate the diffusion constant D. Table 2.1 includes the number of island per array, rounded to the hundredth for clarity. This table includes the specific number of islands, which can be useful in many calculations (e.g. the number of plaquettes and vortices).

Sample	Island Spacing [nm]	No. of Islands [$\times 10^3$]	Resistivity [10^{-6} Ω·cm]
1	90, 140, 190, 240, 290, 340	33.858, 25.8, 20.482, 16.56, 13.734, 11.4	6.25
2	90, 140, 190, 240, 290, 340	33.858, 25.8, 20.482, 16.56, 13.734, 11.4	6.25
3	440, 540, 640	8.379, 6.450, 5.054	6.18
4	490, 540, 590, 640, 690	153.846, 135, 119.364, 106.56, 95.732	6.10
5	740, 840, 940, 1040, 1140, 1240	86.5, 71.278, 59.904, 51.072, 43.911, 38.295	8.7
6	740, 840, 940, 1040, 1140	86.5, 71.278, 59.904, 51.072, 43.911	8.1

Table B.1: **Additional Information on Samples Presented in this Thesis**.

Appendix C

Additional Magnetic Frustration Data

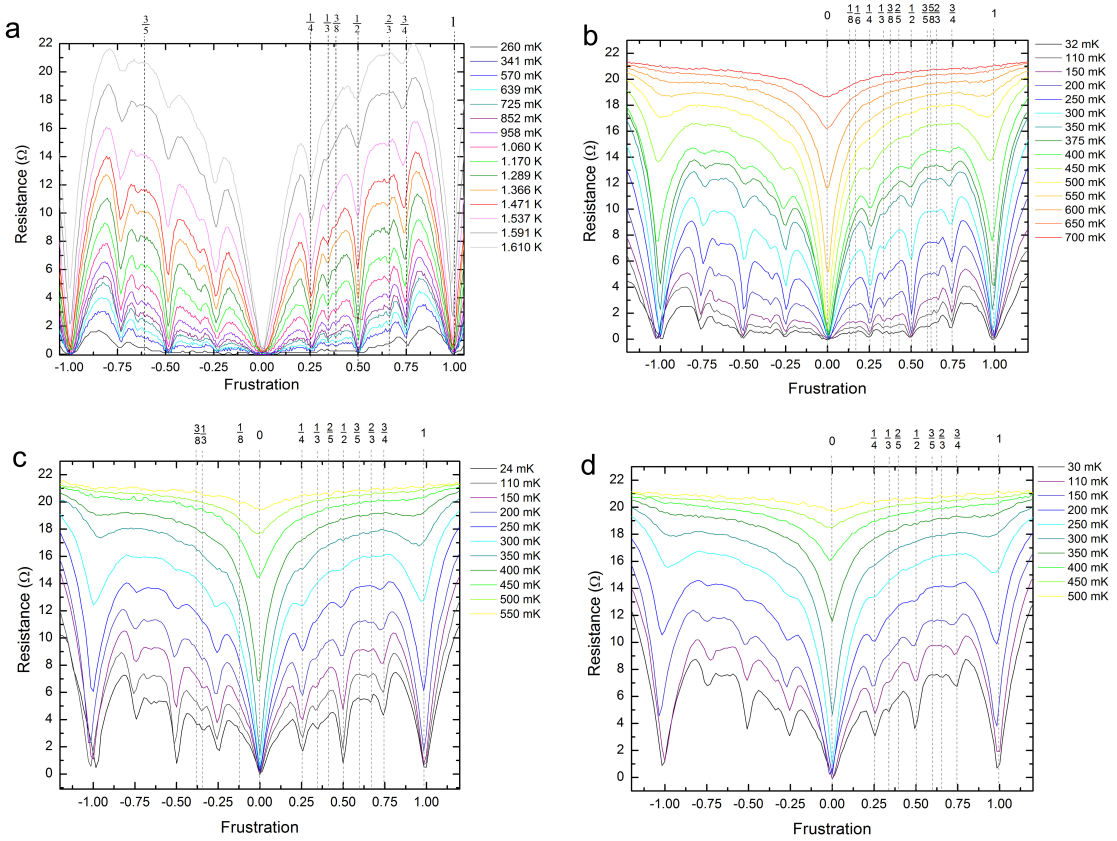

Figure C.1: **Magnetic Frustration Isotherms in Nb Arrays**. Magnetic frustration is a manifestation of competing magnetic ground states. The plots show the evolution of magnetoresistance oscillations in arrays with island spacings $d =$ (**a**) 290 nm, (**b**) 540 nm, (**c**) 590 nm, and (**c**) 640 nm. Dips can be seen at rational values of frustration $f = \frac{BA}{\Phi_0}$, where the area of the plaquette is A and B is the applied magnetic field. Note that the island height in each array is $z =$ (**a**) 87 nm and (**b**, **c**, **d**) 125 nm.

Appendix D

Arrays of Al Islands on Au Layer

Prior to fabricating arrays of Nb islands on Au, we studied arrays of Al islands on Au. Here, we report measurements on arrays of Al islands on a thin layer of Au, observing a tunable, geometry-dependent T_c, and evidence of a BKT transition and Andreev reflection. Samples were fabricated using a similar procedure to that outlined in Section 2.1. There were two major differences. The sample was cooled during evaporation using a continuous flow of LN_2, which is known to result in an increased mean free path in Al. Secondly, the lift-off procedure involved mounting the sample upside-down in a beaker of warm acetone (40 – 50°C). A magnetic stir-bar spun below the sample to assist in gently removing the resist.

The use of Al instead of Nb presented numerous hurdles. First of all, the T_c of Al is fairly low. From the DeGennes-Werthamer relation Eq. 1.5, we know that the T_c of a SN bilayer is suppressed in accordance with the relative of the thicknesses of each layers. Ideally, we would want to begin with a higher z_S-to-z_N ratio than in the research presented here on Nb-Au arrays. Also, both LAT and our phenomenological model predict a marked further suppression in T_2 with an increase in island spacing. A continuous Al film already has a low $T_c \approx 1.1$ K; it was easy to suppress T_2 below the accessible temperature range of our measurement apparatuses.

The second major hurdle was that fabricating Al-Au structures is more difficult than Nb-Au structures. The sticking coefficient of Al is significantly higher than that of Nb; the lift-off process with Nb is far easier than that using Al [1]. We were unable to consistently fabricate arrays of closely-spaced Al islands ($d < 90$ nm). Though fabricating closely-spaced individual junctions of Al is not difficult, lift-off is more difficult in arrays. Two processes used to clean the S-N interface (UV Ozone and ion milling) also slightly encumber lift-off. The devices required long hours (1 to 8 hours) of sonication in warm acetone to complete lift-off in

[1] Given that Nb tends not to stick well to many materials, and the source in the evaporator radiates substantial heat during evaporation, many researchers find it more difficult to use than Al.

the center of the arrays. Less than half of the samples were severely damaged during this process; it was not the show-stopper. However, the lift-off process did severely limit the heights of the islands we could fabricate, requiring us to use an extremely thin normal metal. Extremely thin layers of many metals tend to form discontinuous films with either immeasurable resistances or insulating behavior. We chose Au because we could reproducibly evaporate 3-nm thick layers of Au on a 0.5 Å thick Ti sticking layer.

Lastly, observations of a rapid increase in the device resistance at room temperature evinced interlayer diffusion. Consequently, the samples were immediately cooled to 77 K after lift-off of the Al layer.

D.1 Superconducting Transitions in Al-Au arrays

We fabricated and studied triangular arrays of 20-nm thick Al superconducting islands with 140-nm and 340-nm center-to-center spacings on a 3-nm thick layer of Au. All islands are 260-nm in diameter. Figure D.1 shows the temperature-dependent resistances measured in the ^{3}He cryostat using a 50 nA excitation current. The 140-nm spaced islands exhibit a single transition to a zero-resistance superconducting state, and the 340-nm spaced islands show a two-step transition. We were unable to investigate whether the 340-nm spaced islands become fully superconducting due to the limited accessible temperature of the ^{3}He cryostat. Presuming that both arrays experience BKT transitions, the transition to the superconducting state T_2 is suppressed for the farther spaced islands.

Fits to the resistance versus temperature curves were consistent with the BKT prediction $R \propto R_n e^{-b/\sqrt{T-T_2}}$. IV isotherms (Figure D.2) show evidence of the Nelson-Kosterlitz jump, however, limited data and very long low current Ohmic tails from trapped flux in the magnet limited the accuracy of the extracted T_2. From this analysis, $T_2 = 300$ mK in the 140-nm spaced array and the projected T_2 for the 340-nm spaced array is 246 mK.

We transitioned from Al to Nb for many reasons. The transition temperatures in Al arrays of fixed geometry were not reproducible; this may be due to rapid diffusion between the Al and Au. Upon increasing the island spacing even slightly beyond 340 nm, the resistances were temperature independent down to 15 mK. It was unclear if this was due to metallic behavior or if $T_2 <$15 mK.

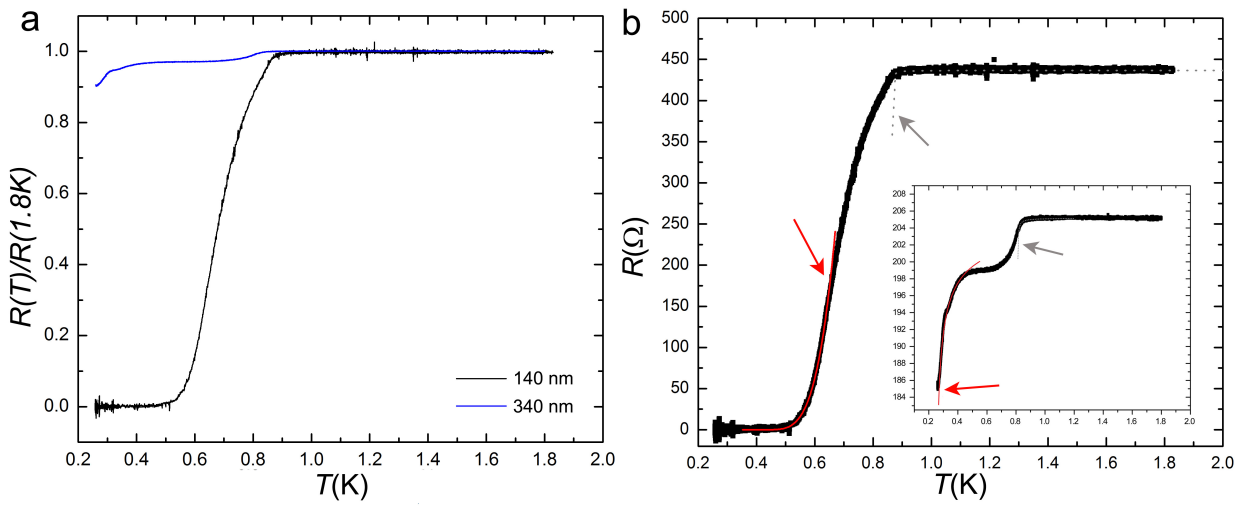

Figure D.1: **Superconductivity in Arrays of Al Islands on Au**. Temperature dependent resistive transitions in arrays with island spacings (**a**) 140 nm and (**b**) 340 nm. The island diameter is 260 nm for all arrays. The islands are 20 nm thick on a 3 nm thick Au layer. (**a**) A comparision of the transitions in 2 different arrays. (**b**) The **main panel** shows the transition in the 140-nm spaced islands. The red curve is a fit of the low temperature region to the BKT prediction and the dotted gray curve the Aslamazov-Larkin prediction, applicable to the T_1 of the individual islands. The **inset** shows the transitions in and fits for the 340-nm spaced islands.

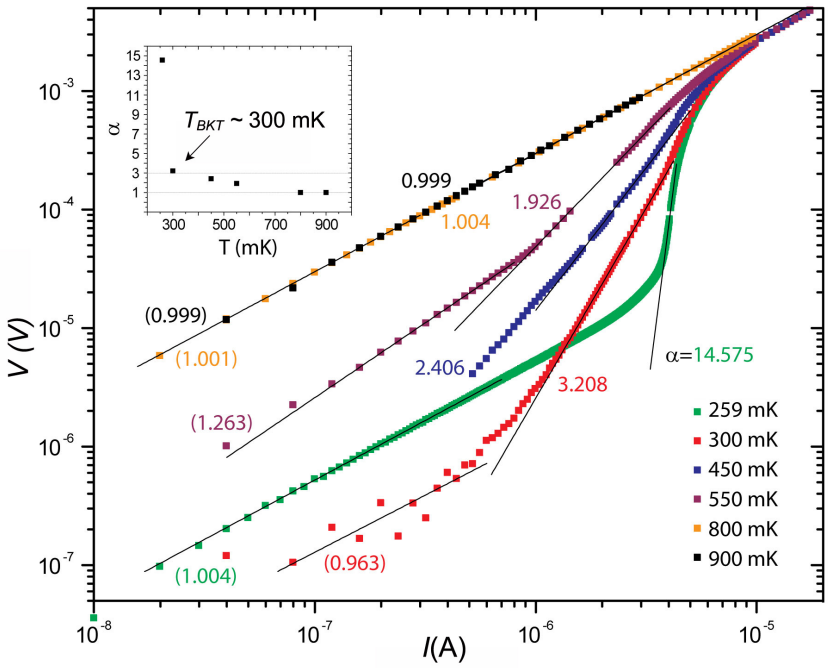

Figure D.2: **Possible BKT Transition in Arrays of Al Islands on Au**. **Main Panel**, Log I-Log V plot of current-voltage characteristics taken at six different temperatures for the array with $d = 140$ nm. The slope of the curves is marked; the slope of the low current Ohmic tails is parenthetically labelled. The **inset** is a plot of the temperature dependence of α, showing an extracted T_2 of 300 mK.

D.2 Critical Current and Andreev Reflection in Al-Au Arrays

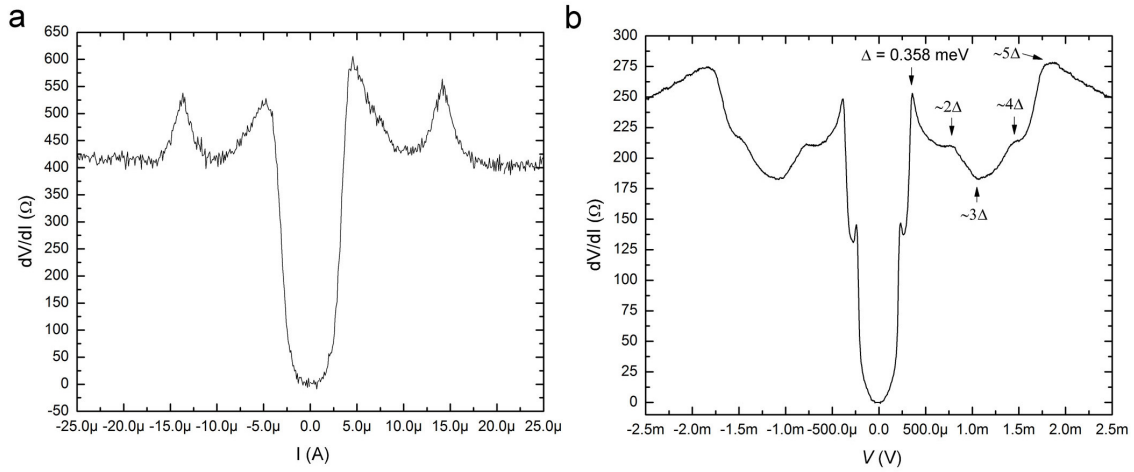

Figure D.3: **Critical Current and Evidence of Andreev Reflection in Arrays of Al Islands**. *IV* Characteristics in 140-nm spaced islands at 259 mK. (**a**) Differential resistance in response to a (**a**) swept current and (**b**) voltage bias. From (**a**), the critical current is extracted from the low current peak at 4.5 μA. The high current peak at 14.1 μA may signify the I_c of the individual Al islands. (**b**) Dips and peaks at multiple integral values of the gap $\Delta = 0.358$ meV are likely evidence of Muliple Andreev reflection (MAR).

Both the current- and voltage-biased differential resistance responses were measured in both Al arrays; the results for the 140-nm spaced islands are shown in Figure D.3. Differential resistance measurements were taken by adding a 10 nV AC signal from a SRS 830 lock-in amplifier to a swept DC signal from a Keithley 2400 sourcemeter using a battery operated sum box. The resulting change in voltage was recorded using a lock-in amplifier. Current-biased sweeps were taken in a four-point configuration, while voltage-biases sweeps required a two-point measurement. Despite only observing a one-step transition to the superconducting state in the 140-nm spaced islands, $\frac{dV}{dI}$ vs I shows two peaks above $I = 0$. From Figure D.3a, we note the array critical current $I_c = 4.5$ μA.

Unlike in the Nb arrays, we were able to cleanly observe Multiple Andreev Reflection in the Al arrays. In the Andreev Reflection picture, an electron with energy ε above the Fermi energy, where $\varepsilon < \Delta$ is retroreflected as a hole at the normal-superconductor interface. An Cooper pair is formed in the second superconductor. The retroreflected hole gains energy eV from the voltage bias as it crosses the normal metal. In the case of multiple Andreev reflection, the hole continues to gain energy eV with each successive reflection n, and it finally absorbed when $neV \geq 2\Delta$. This leads to a series of peaks and dips in the voltage-biased differential resistance. Figure D.3b shows the $\frac{dV}{dI}$ vs. V for the arrays with $d = 140$ nm. Dips and peaks are evident at integral multiples of the gap.

We were unable to apply a high enough voltage bias the Nb island arrays to observe MAR. Due to the

high resistance filters on the transport leads in all measurement systems, the required voltage bias to observe multiple peaks would cause Joule heating [2]. If we integrate our current-biased differential resistance data to extract $\frac{dV}{dI}$ vs. V, we do see evidence of structure. However, that is beyond the scope of this thesis.

[2]Arrays that superconduct within the accessible temperature range of the pumped He-4 cryostat have high gaps. Those measured in the dilution cryostat have lower gaps, but the cooling power of the system is also significantly lower.

References

[1] S. V. Kravchenko and M. P. Sarachik. Metal-insulator transition in two-dimensional electron systems. *Rep. Prog. Phys.*, 67(1):1–44, 2004.

[2] N. Mason. Dissipation effects on the superconductor-insulator transition in 2D superconductors. *Phys. Rev. Lett.*, 395(26):253–5344, June 1999.

[3] A. M. Goldman and N. Markovic. Superconductor-insulator transitions in the two-dimensional limit. *Phys. Today*, 51(11):39, 1998.

[4] P. Phillips, Y. Wan, I. Martin, and S. Knysh. Superconductivity in a two-dimensional electron gas. *Nature*, 395:253–257, 1997.

[5] M. Feigel'man, A. Larkin, and M. Skvortsov. Quantum superconductor-metal transition in a proximity array. *Phys. Rev. Lett.*, 86(9):1869–1872, February 2001.

[6] B. Spivak, A. Zyuzin, and M. Hruska. Quantum superconductor-metal transition. *Phys. Rev.*, 64:13, April 2000.

[7] R.S. Shulman and V.C. Cox. How to write a Ph.D. dissertation. *Annals of Improbable Research*, 3(5):8, 1997.

[8] J. Bardeen, L. N. Cooper, and J. R. Schrieffer. Theory of superconductivity. *Phys. Rev.*, 108:1175–1204, December 1957.

[9] B.P. Martins. *Frontiers in superconductivity research.* Nova Science Publishers, 2003.

[10] A. Rimberg. Dissipation-driven superconductor-insulator transition in a two-dimensional Josephson-junction array. *Phys. Rev. Lett.*, 48(13):3316–2635, March 1997.

[11] H. Fu, A. Seidel, J. Clarke, and D.H. Lee. Stabilizing superconductivity in nanowires by coupling to dissipative environments. *Phys. Rev. Lett.*, 96(15):2–5, April 2006.

[12] C.J. Lobb, D. Abraham, and M. Tinkham. Theoretical interpretation of resistive transition data from arrays of superconducting weak links. *Phys. Rev. B*, 27(1):150–157, January 1983.

[13] K. M. Lang, V. Madhavan, and J. E. Hoffman. Imaging the granular structure of high-T_c superconductivity in underdoped $Bi_2Sr_2CaCu_2O_8 + \delta$. *Nature*, 415, 2002.

[14] E. Shimshoni. Transport through quantum melts. *Phys. Rev. Lett.*, 140(15):A1197–3355, 1998.

[15] A. Kapitulnik, N. Mason, S.A. Kivelson, and S. Chakravarty. Effects of dissipation on quantum phase transitions. *Phys. Rev. B*, 63(12):125322, March 2001.

[16] B. Spivak, P. Oreto, and S. Kivelson. Theory of quantum metal to superconductor transitions in highly conducting systems. *Phys. Rev. B*, 77(21):1–18, June 2008.

[17] A. Glatz, I. Aranson, T. Baturina, N. Chtchelkatchev, and V. Vinokur. Self-organized superconducting textures in thin films. *Phys. Rev. B*, 84(2):1–9, July 2011.

[18] The Economist. Moore's law at 40: Happy birthday, The tale of a frivolous rule of thumb, 2005.

[19] D.J. Resnick and J.C. Garland. Kosterlitz-Thouless transition in proximity-coupled superconducting arrays. *Phys. Rev. Lett.*, 47(21), November 1981.

[20] M. Tinkham. *Introduction to superconductivity.* Dover books on physics and chemistry. Dover Publications, 2004.

[21] J.M. Kosterlitz and D.J. Thouless. Ordering, metastability and phase transitions in two-dimensional systems. *J. Phys. C. Solid State*, 1181(6):1181 – 1203, 1973.

[22] L.A. Turkevich. Resistivity of superconducting films. *J. Phys. C. Solid State*, 12(1):L385, 1979.

[23] V. M. Svistunov, A. I. D, and V. Yu Tarenkov. Resistive vortices and two-dimensional transition in aluminum films. *J. Low. Temp. Phys.*, 57:619–627, 1984.

[24] H.M. Jaeger, D.B. Haviland, and B.G. Orr. Onset of superconductivity in ultrathin granular metal films. *Phys. Rev. B*, 40(1), July 1989.

[25] H.S.J. Van der Zant and H.A. Rijken. Phase transition of frustrated two-dimensional Josephson junction arrays. *J. Low Temp. Phys.*, 82, 1991.

[26] C. Chen, P. Delsing, D. Haviland, Y. Harada, and T. Claeson. Flux flow and vortex tunneling in two-dimensional arrays of small Josephson junctions. *Phys. Rev. B*, 54(13):9449–9457, October 1996.

[27] M.P.A. Fisher. Quantum phase transitions in disordered two-dimensional superconductors. *Phys. Rev. Lett.*, 65(7):923–927, August 1990.

[28] D.B. Haviland, Y. Liu, and A.M. Goldman. Onset of superconductivity in the two-dimensional limit. *Phys. Rev. Lett.*, 62(18):2180–2183, May 1989.

[29] Y. Liu, K.A. McGreer, B. Nease, and D.B. Haviland. Scaling of the insulator-to-superconductor transition in ultrathin amorphous Bi films. *Phys. Rev. Lett.*, 67(15):2068–2071, 1991.

[30] Y. Takahide, R. Yagi, A. Kanda, Y. Ootuka, and S. Kobayashi. Superconductor-insulator transition in a two-dimensional array of resistively shunted small Josephson junctions. *Phys. Rev. Lett.*, 85(9):1974–7, August 2000.

[31] Y. Takahide, H. Miyazaki, and Y. Ootuka. Superconductor-insulator crossover in Josephson junction arrays due to reduction from two to one dimension. *Phys. Rev. B*, 73(22):1–7, 2006.

[32] A. Yazdani and A. Kapitulnik. Superconducting-insulating transition in two-dimensional a-MoGe thin films. *Phys. Rev. Lett.*, 74(15):3037–3040, April 1995.

[33] M.A. Paalanen and A.F. Hebard. Low-temperature insulating phases of uniformly disordered two-dimensional superconductors. *Phys. Rev. Lett.*, 69, September 1992.

[34] T. Baturina, A. Mironov, V. Vinokur, M. Baklanov, and C. Strunk. Localized superconductivity in the quantum-critical region of the disorder-driven superconductor-insulator transition in TiN thin films. *Phys. Rev. Lett.*, 99(25):1–4, December 2007.

[35] J.M. Valles Jr, R.C. Dynes, and J.P. Garno. Electron tunneling determination of the order-parameter amplitude at the superconductor-insulator transition in 2D. *Phys. Rev. Lett.*, 69(24):3567–3570, December 1992.

[36] A. E. White, R.C. Dynes, and J.P. Garno. Destruction of superconductivity in quench-condensed two-dimensional films. *Phys. Rev. B*, 33(5):3549 – 3552, 1986.

[37] P. Phillips and D. Dalidovich. The elusive Bose metal. *Science*, 302(5643):243–7, October 2003.

[38] A.O. Caldeira and A.J. Leggett. Influence of dissipation on quantum tunneling in macroscopic systems. *Phys. Rev. Lett.*, 46(4):211–214, January 1981.

[39] N. Mason and A. Kapitulnik. Superconductor-insulator transition in a capacitively coupled dissipative environment. *Phys. Rev. B*, 65(22):1–4, May 2002.

[40] G. Deutscher, O. Entin-Wohlman, and Z. Ovadyahu. Transition temperature of proximity-effect thin sandwiches. *Phys. Rev. B*, 14(3):1002–1006, August 1976.

[41] J.J. Hauser, H.C. Theuerer, and N.R. Werthamer. Superconductivity in Cu and Pt by means of superimposed films with lead. *Phys. Rev.*, 136(3A):637–641, 1964.

[42] Z. Long, M.D. Stewart Jr, and J.M. Valles Jr. Super-weakly coupled superconductivity in ultrathin superconductornormal-metal bilayers. *Phys. Rev. B*, 73(14):140507, 2006.

[43] T. Kouh and J. Valles. Deviations from mean-field behavior in disordered nanoscale superconductornormal-metalsuperconductor arrays. *Phys. Rev. B*, 67(14):1–4, 2003.

[44] S. Bose and P. Ayyub. Superconducting proximity effect in PbAg nanocomposites. *Phys. Rev. B*, 76(14):1–5, 2007.

[45] O. Bourgeois, A. Frydman, and R. Dynes. Proximity effect in ultrathin Pb/Ag multilayers within the Cooper limit. *Phys. Rev. B*, 68(9):2–5, September 2003.

[46] C.J. Kircher. Superconducting proximity effect of Nb. *Phys. Rev.*, 168(2):437–441, 1968.

[47] R. Banerjee, P. Vasa, G.B. Thompson, H.L. Fraser, and P. Ayyub. Proximity effect in Nb/Zr multilayers with variable Nb/Zr ratio. *Solid State Commun.*, 127(5):349–353, 2003.

[48] A. K. Gupta. Anomalous density of states in hybrid normal metal-superconductor bilayers. *Pramana*, 87(1):027002–259, 2006.

[49] N.R. Werthamer. Theory of the superconducting transition temperature and energy gap function of superposed metal films. *Phys. Rev.*, 132(1960):2440–2445, 1963.

[50] L.G. Aslamasov and A.I. Larkin. The influence of fluctuation pairing of electrons on the conductivity of normal metal. *Phys. Lett. A*, 26(6):238 – 239, 1968.

[51] R.S. Newrock, C.J. Lobb, U. Geigenmller, and M. Octavio. The two-dimensional physics of Josephson junction arrays. volume 54 of *Solid State Physics*, pages 263 – 512. Academic Press, 1999.

[52] S. Chakravarty, G.L. Ingold, and S. Kivelson. Quantum statistical mechanics of an array of resistively shunted Josephson junctions. *Phys. Rev. B*, 37(7), 1988.

[53] G. Refael, E. Demler, Y. Oreg, and D. Fisher. Dissipation and quantum phase transitions of a pair of Josephson junctions. *Phys. Rev. B*, 68(21):1–34, 2003.

[54] R Yagi, S. Kobayashi, and Y. Ootuka. Phase diagram for superconductor-insulator transition in single small Josephson junctions with shunt resistor. *J. Phys. Soc. Jpn.*, 66(12):3722–3724, 1997.

[55] K. Wagenblast. Superconductor-insulator transition in a tunable dissipative environment. *Phys. Rev. Lett.*, 48(14):3316–2733, October 1997.

[56] H.S.J. van der Zant, W.J. Elion, L.J. Geerligs, and J.E. Mooij. Quantum phase transitions in two dimensions: Experiments in Josephson-junction arrays. *Phys. Rev. B*, 54(14):10081–10093, October 1996.

[57] D. Kimhi and F. Leyvraz. Resistive transition in two-dimensional arrays of proximity Josephson junctions: Magnetic field dependence. *Phys. Rev. B*, 1984.

[58] C. Macchiavello, G.M. Palma, and A. Zeilinger. *Quantum computation and quantum information theory: reprint volume with introductory notes for ISI TMR Network School, 12-23 July 1999, Villa Gualino, Torino, Italy.* World Scientific, 2000.

[59] K. D. Usadel. Generalized diffusion equation for superconducting alloys. *Phys. Rev. Lett.*, 25:507–509, August 1970.

[60] J. M. Martinis, G. C. Hilton, K. D. Irwin, and D. A. Wollman. Calculation of Tc in a normal-superconductor bilayer using the microscopic-based Usadel theory. *Nuclear Instruments and Methods in Physics Research*, 444:23–27, 2000.

[61] P. Dubos, H. Courtois, B. Pannetier, F. K. Wilhelm, A. D. Zaikin, and G. Schon. The Josephson critical current in a long mesoscopic S-N-S junction. *Phys. Rev. B*, 63(6):5, 2001.

[62] F.K. Wilhelm, A.D. Zaikin, and G. Schon. Supercurrent in a mesoscopic proximity wire. *J. Low Temp. Phys.*, 106(305), 1997.

[63] C. Delacour, L. Ortega, M. Faucher, T. Crozes, T. Fournier, B. Pannetier, and V. Bouchiat. Persistence of superconductivity in niobium ultrathin films grown on R-plane sapphire. *Phys. Rev. B*, 83(14):1–8, 2011.

[64] D.R. Lide. *CRC Handbook of Chemistry and Physics: A Ready-Reference Book of Chemical and Physical Data.* CRC Handbook of Chemistry and Physics, 85th Ed. CRC Press, 2004.

[65] E.M. Gershenzon, M.E. Gershenzon, and G.N. Goltsman. Electron–phonon interaction in ultrathin niobium films. *Zh. Eksp. Teor. Fiz.*, 70(March), 1990.

[66] Yuji Asada. Superconductivity of niobium films. *J. Phys. Soc. Jpn.*, 25(2):347–354, 1969.

[67] I.M. Kooy, C.and Nieuwenhuizen. Structural effects in thin films observed by electron microscopy of thin film cross-section, 1965.

[68] S. Eley, S. Gopalakrishnan, P.M. Goldbart, and N. Mason. Approaching zero-temperature metallic states in mesoscopic superconductor-normal-superconductor arrays. *Nature Phys.*, 8(1):59–62, December 2011.

[69] C.V. Parker, P. Aynajian, E. H. da Silva Neto, A. Pushp, S. Ono, J. Wen, Z. Xu, G. Gu, and A. Yazdani. Fluctuating stripes at the onset of the pseudogap in the high-T_c superconductor $Bi_2Sr_2CaCu_2O_{8+x}$. *Nature*, 468(7324):677–80, 2010.

[70] V. V. Moshchalkov, J. Vanacken, and L. Trappeniers. Phase diagram of high-T_c cuprates: stripes, pseudogap, and effective dimensionality. *Phys. Rev. B*, 64:214504, November 2001.

[71] A. Kampf and J. R. Schrieffer. Pseudogaps and the spin-bag approach to high-t_c superconductivity. *Phys. Rev. B*, 41:6399–6408, April 1990.

[72] A. P. Kampf and J. R. Schrieffer. Spectral function and photoemission spectra in antiferromagnetically correlated metals. *Phys. Rev. B*, 42:7967–7974, November 1990.

[73] R. Preuss, W. Hanke, C. Gröber, and H. G. Evertz. Pseudogaps and their interplay with magnetic excitations in the doped 2D hubbard model. *Phys. Rev. Lett.*, 79:1122–1125, August 1997.

[74] J. R. Schrieffer, X.-G. Wen, and S.-C. Zhang. Spin-bag mechanism of high-temperature superconductivity. *Phys. Rev. Lett.*, 60:944–947, March 1988.

[75] N. M. Plakida. Theory of antiferromagnetic pairing in cuprate superconductors. *Low Temperature Physics*, 32(4):363, 2006.

[76] V. M. Loktev, R. M. Quick, and S. G. Sharapov. Phase fluctuations and pseudogap phenomena. *Physics Reports*, 349(1):1 – 123, 2001.

[77] Y. Youichi and Y. Kosaku. Theory of pseudogap phenomena in high-T_c cuprates based on the strong coupling superconductivity. *J. Phys. Soc. Jpn.*, 68(9):2999–3015, 1999.

[78] D. Rohe and W. Metzner. Pair-fluctuation-induced pseudogap in the normal phase of the two-dimensional attractive Hubbard model at weak coupling. *Phys. Rev. B*, 63:224509, May 2001.

[79] H.-J. Kwon and A. T. Dorsey. Effect of phase fluctuations on the single-particle properties of underdoped cuprates. *Phys. Rev. B*, 59:6438–6448, March 1999.

[80] A. Ghosal, M. Randeria, and N. Trivedi. Inhomogeneous pairing in highly disordered *s*-wave superconductors. *Phys. Rev. B*, 65:014501, November 2001.

[81] Igor F. Herbut. Quantum fluctuations, pseudogap, and the T = 0 superfluid density in strongly correlated *d*-wave superconductors. *Phys. Rev. B*, 70:184507, November 2004.

[82] L. B. Ioffe and A. J. Millis. Superconductivity and the c axis spectral weight of high-Tc superconductors. *Science*, 285(5431):1241–1244, 1999.

[83] M. Jiri, J. Boldizsr, and K. Levin. Numerical studies of the s-wave pseudogap state and related Tc: the pairing approximation theory. *Physica C*, 321(12):113 – 133, 1999.

[84] V.P. Gusynin, V.M. Loktev, R.M. Quick, and S.G. Sharapov. Quantum phase fluctuations responsible for pseudogap. *Physica C*, 370(4):239 – 245, 2002.

[85] B. Sacépé, C. Chapelier, T. I. Baturina, V. M. Vinokur, M. R. Baklanov, and M. Sanquer. Pseudogap in a thin film of a conventional superconductor. *Nature Communications*, 1(9):140, 2010.

[86] V. Ambegaokar and A. Baratoff. Tunneling between superconductors. *Phys. Rev. Lett.*, 10:486–489, June 1963.

[87] D.R. Tilley, D.R. Tilley, J. Tilley, J. Tilley, and J. Tilley. *Superfluidity and superconductivity*. Graduate student series in physics. Institute of Physics Publishing, 1994.

[88] C. Kaiser. *High quality Nb/Al-AlOx/Nb Josephson junctions: Technological development and macroscopic quantum experiments*. KIT Scientific Publishing.

[89] H. Ehrenreich and F. Spaepen. *Solid state physics: advances in research and applications*. Solid State Physics. Academic Press, 1999.

[90] D.R. Nelson and J.M. Kosterlitz. Universal jump in the superfluid density of two-dimensional superfluids. *Phys. Rev. Lett.*, 39(19):1201–1205, November 1977.

[91] R. Voss and Richard A. Webb. Phase coherence in weakly coupled array of 20000 Nb Josephson junctions. *Phys. Rev. B*, 25(5):3446 – 3449, 1982.

[92] B.J. Wees, H.S.J. Van der Zant, and J.E. Mooij. Phase transitions of Josephson-tunnel-junction arrays at zero and full frustration. *Phys. Rev. B*, 35(13):7291–7295, May 1987.

[93] W. C. Stewart. Current-voltage characteristics of Josephson junctions. *Applied Physics Lett.*, 277(12):10–14, 1968.

[94] D. E. McCumber. Effect of ac impedance on dc voltage-current characteristics of superconductor weak-link junctions. *J. Appl. Phys.*, 39(7):3113, 1968.

[95] C. M. Falco. Effects of thermal noise on current-voltage characteristics of Josephson junctions. *Phys. Rev. B*, 10(5):1865 – 1873, September 1974.

[96] V. Ambegaokar and B.I. Halperin. Voltage due to thermal noise in the DC Josephson effect. *Phys. Rev. Lett.*, 22(25):23–25, 1969.

[97] W. Coffey, Y.P. Kalmykov, and J.T. Waldron. *The Langevin equation: with applications to stochastic problems in physics, chemistry, and electrical engineering.* World Scientific Series in Contemporary Chemical Physics. World Scientific, 2004.

[98] L. Angers, F. Chiodi, G. Montambaux, M. Ferrier, S. Gueron, and H. Bouchiat. Proximity dc squids in the long-junction limit. *Phys. Rev. B*, 77(165408):1–12, 2008.

[99] H. Courtois, Ph. Gandit, and B. Pannetier. Proximity-induced superconductivity in a narrow metallic wire. *Phys. Rev. B*, 52:1162–1166, July 1995.

[100] R. A. Webb and F. Voss. Macroscopic quantum tunneling in 1-um nb Josephson junctions. *Phys. Rev. Lett.*, 47(4), July 1981.

[101] I. Baek, Y. Yun, and M. Choi. Critical behaviors of triangular Josephson junction arrays in a magnetic field. *J. Phys. Chem. Solids*, 67(1-3):172–174, January 2006.

[102] M. Vélez, J.I. Martín, J.E. Villegas, A. Hoffmann, E.M. González, J.L. Vicent, and I. K. Schuller. Superconducting vortex pinning with artificial magnetic nanostructures. *Journal of Magnetism and Magnetic Materials*, 320(21):2547–2562, 2008.

[103] W.Y. Shih and D. Stroud. Molecular-field approximation for a Josephson-coupled superconducting array in a magnetic field. *Phys. Rev. B*, 28(11):6575–6577, 1983.

[104] W.Y. Shih and D. Stroud. Two-dimensional superconducting arrays in a magnetic field: Effects of lattice structures. *Phys. Rev. B*, 32(1):158 – 165, July 1985.

[105] N. Mason and A. Kapitulnik. True superconductivity in a two-dimensional superconducting-insulating system. *Phys. Rev. B*, 64(6):060504, 2001.

[106] C. Ebner and D. Stroud. Diamagnetic susceptibility of superconducting clusters: Spin-glass behavior. *Phys. Rev. B*, 31(1):165, January 1985.

[107] D. A. Balaev, D. M. Gokhfeld, A. A. Dubrovski, S. I. Popkov, K. a. Shaikhutdinov, and M. I. Petrov. Magnetoresistance hysteresis in granular HTSCs as a manifestation of the magnetic flux trapped by superconducting grains in YBCO + CuO composites. *JETP*, 105(6):1174–1183, December 2007.

[108] L. Ji, M.S. Rzchowski, and N. Anand. Magnetic-field-dependent surface resistance and two-level critical-state model for granular superconductors. *Phys. Rev. B*, 47(1):470–483, January 1993.

[109] A. Mohanta and D. Behera. Magnetic field dependence of the pinning effect in -doped ceramic superconductor. *Solid State Commun.*, 150(2930):1325 – 1328, 2010.

[110] M.V. Feigelman, V.B. Geshkenbein, and A.I. Larkin. Pinning and creep in layered superconductors. *Physica C*, 167:177–187, 1990.

[111] M.S. Rzchowski, S.P. Benz, and M. Tinkham. Vortex pinning in Josephson-junction arrays. *Phys. Rev. B*, pages 2041 –2049, 1990.

[112] H.S.J. Van der Zant, F.C. Fritschy, T.P. Orlando, and J.E. Mooij. Vortex dynamics in two-dimensional underdamped, classical Josephson-junction arrays. *Phys. Rev. B*, 47(1):295–304, January 1993.

[113] S. Kirkpatrick. Percolation and conduction. *Reviews of Modern Physics*, 45(4):574–588, 1973.

[114] T.C. Halsey. Array in an irrational magnetic field : A superconducting glass? *Phys. Rev. Lett.*, 55(9):1018–1021, August 1985.

[115] M.Y. Choi and D. Stroud. Glassy phase in an array of Josephson junctions. *Phys. Rev. B*, 35(13):7109–7112, May 1987.

[116] I.-C. Baek, Y.-J. Yun, and M.-Y. Choi. Vortex state of a 2D Josephson junction array at irrational frustration. *Physica C*, 388-389:785–786, May 2003.

[117] S. A. Kivelson, I. P. Bindloss, E. Fradkin, and V. Oganesyan. How to detect fluctuating stripes in the high-temperature. *Rev. Mod. Phys.*, 75(October):1201–1241, 2003.

[118] C. Yasuda, S. Todo, K. Hukushima, F. Alet, M. Keller, M. Troyer, and H. Takayama. Néel temperature of quasi-low-dimensional Heisenberg antiferromagnets. *Phys. Rev. Lett.*, 94(21):5–8, 2005.